Lightning Protection and Radio Frequency Interference Mitigation for the Karoo Array Telescope

by

P. Gideon Wiid

Dissertation presented in fulfilment of the requirements for the degree of Doctor of Philosophy in Engineering at the Faculty of Engineering, Stellenbosch University

Promotors: Prof. Howard C. Reader & Dr. Riana H. Geschke
Department of Electrical and Electronic Engineering

March 2010

Declaration

By submitting this dissertation electronically, I declare that the entirety of the work contained therein is my own, original work, that I am the owner of the copyright thereof (unless to the extent explicitly otherwise stated) and that I have not previously in its entirety or in part submitted it for obtaining any qualification.

March 2010

Summary

South Africa and Australia are now the two remaining countries bidding for the Square Kilometre Array (SKA), the biggest and most sensitive project ever undertaken in radio astronomy. The South African SKA is demonstrating its technology capabilities through the Karoo Array Telescope (KAT or MeerKAT).

The development of KAT is taking place in stages to optimise design and minimise risks at each stage. An array of seven 12 m antennas will be complete by the end of 2009, called KAT-7. The following phase will see the construction of MeerKAT, which will lead to eighty arrayed dishes.

Lightning and RFI studies for KAT-7 are the focus of this dissertation. Due to the extent and complexity of the South African demonstrator project, these studies have largely been conducted on a single structure. Parameters for the dish antenna and pedestal design changed throughout their development. To be effective, the doctoral research had to track these changes appropriately.

A Method of Moments frequency domain computational electromagnetic code, FEKO, is used throughout the study. The consequences of direct and indirect lightning strikes are examined for the KAT-7 structure. Important FEKO model verification is achieved through measurement of physical scale models in an anechoic chamber. The microwave simulation code, CST, gives direct comparison of FEKO results by using a finite volume time domain method of calculation.

Using frequency domain analysis on these models, the lightning down conductor design over the dish antenna bearings is optimised with cost-effectiveness as one driving parameter. RFI coupling levels for different designs are compared to each other to identify areas requiring RFI mitigation. Analysis of resonances enables evaluation of the mitigation at frequencies sensitive to radio astronomy.

A Sommerfeld integral ground plane is used together with the computational model to investigate the use of the concrete foundation steel reinforcing as part of the lightning earthing electrode system. Different interconnections of the steel reinforcing elements are critically evaluated.

The KAT-7 design incorporated clear lightning protection and RFI mitigation policies derived from recommendations contained within this dissertation.

Opsomming

Suid-Afrika en Australië is nou die oorblywende twee lande wat bie vir die Vierkante Kilometer Reeks (SKA), die grootste en mees sensitiewe projek nog ooit in radio astronomie onderneem. Die Suid Afrikaanse SKA demonstreer sy tegnologiese bekwaamheid met die Karoo Reeks Teleskoop (KAT of MeerKAT).

Die ontwikkeling van KAT vind plaas in fases om die ontwerp te optimaliseer en risikos te minimaliseer met elke fase. ’n Reeks van sewe 12 m antennas, genaamd KAT-7, sal teen die einde van 2009 klaar wees. Die volgende fase behels die konstruksie van MeerKAT, wat sal lei tot ’n tagtig-skottel reeks.

Die fokus van hierdie proefskrif hanteer weerlig en radiofrekwensie steurings (RFS) vir KAT-7. As gevolg van die omvang en kompleksiteit van die Suid-Afrikaanse demonstreerder projek, is die studies hoofsaaklik op een struktuur gedoen. Parameters vir die antenna-skottel en -voetstuk ontwerp het met hul ontwikkeling deurgaans verander. Om effektief te wees, moes die doktorale navorsing hierdie veranderinge toepaslik volg.

’n Metode-van-Momente frekwensiedomein rekenaar elektromagnetiese kode, FEKO, is deurgaans met die studie gebruik. Die gevolge van direkte en indirekte weerligslae vir die KAT-7 struktuur is ondersoek. Belangrike FEKO model bevestiging is bereik met metings van skaalmodelle in ’n anegoïse kamer. Die mikrogolf-simulasie kode, CST, gee ’n direkte vergelyking met die FEKO resultate deur ’n eindige-volume-tyd-domein metode van berekening te gebruik.

Met behulp van frekwensiedomein analise van hierdie modelle, is die weerligafleier-ontwerp oor die antenna-skottel laers ge-optimaliseer, met koste-effektiwiteit as een van die drywingsparameters. RFS koppelingsvlakke vir onderskeie ontwerpe is teen mekaar opgeweeg om areas te identifiseer wat RFS tempering benodig. Analise van resonansies stel die evaluering van die tempering in staat teen frekwensies wat sensitief is vir radio astronomie.

’n Sommerfeld integrale grondvlak word saam met die rekenaarmodel gebruik om die insluiting van die beton se staalversterking as deel van die aardingselektrodestelsel te ondersoek. Verskillende bindmetodes van die onderlinge staalversterkingselemente word krities geëvalueer.

Die KAT-7 ontwerp inkorporeer duidelike weerligbeveiligings- en RFS temperingstrategieë, komende van aanbevelings in hierdie proefskrif omskryf.

Acknowledgements

First and foremost, I want to thank my Lord God for the strength and guidance throughout the three years of research for this PhD degree. Thank you to my wife Ilse, for her support through busy and difficult times, with tons of love and patience, and lots of coffee and snacks. Thanks to my mother-in-law, father and step-mom for their enduring support, and to my friends and family for all the words of encouragement.

I would like to thank the following people for their contribution to the work done in this dissertation: Rodney Urban, Howard Reader, Riana Geschke, Willem Esterhuyse and Wessel Crouwkamp, for their role in the design and building of the scale models. Riana, Rodney, Howard, Paul van der Merwe, Philip Kibet and Martin Siebers, for assisting the measurements in the anechoic chamber. Paul, Howard, Wernich de Villiers and Richard Lord for helping with the measurements at HartRAO. Johan Cronje and Mel van Rooyen at EMSS, for their support with the use of FEKO. Danie Ludick, Evan Lezar, Kevin Cole and David Davidson for their help in accessing the high performance computing centres. Willem, Richard, Carel van der Merwe, Japie Ludick and Kim de Boer for excellent collaboration and support from the SA SKA. David, Johan Joubert and Lex van Deursen for constructive comments on the final dissertation.

The author would like to thank the South African SKA offices and the Tertiary Education Support Programme for funding the research project, EMSS South Africa for making FEKO available to Stellenbosch University for research, the Stellenbosch University High Performance Computer (Rhasatsha) support team as well as the Centre for High Performance Computing (Iqudu) and their support team, and CST for the license used in this research.

A final thank you to the greatest leadership one could ask for in two supervisors, Riana and Howard. Thanks for continual support in many areas, professional guidance, friendly assistance, informed advice and good humour throughout.

– Ek is tot alles in staat deur Hom wat my krag gee –

– Fil 4:13 –

Dedication

This dissertation is dedicated to the love of my life –
my wife, Ilse

Abbreviations

ADM	Advanced Demonstrator Model
CEM	Computational Electromagnetics
CHPC	Centre for High Performance Computing
CM	Common mode
CW	Continuous Wave
dB	Decibel
EM	Electromagnetic
EMC	Electromagnetic Compatibility
EMI	Electromagnetic Interference
EMP	Electromagnetic Pulse
ESA	European Space Agency
FEM	Finite Element Method
F.l.t.r.	From left to right
Fig	Figure
FDTD	Finite Distance Time Domain
FVTD	Finite Volume Time Domain
GHz	GigaHertz
HartRAO	Hartebeespoort Radio Astronomy Observatory
IEC	International Electrotechnical Commission
ITU	International Telecommunications Union
KAT	Karoo Array Telescope
LDC	Lightning Down Conductor
LOFAR	Low Frequency Array
LPDA	Log Periodic Dipole Antenna
LPS	Lightning Protection System
MeerKAT	Karoo Array Telescope (Final stage)
MHz	MegaHertz
MLFMM	Multilevel Fast Multipole Method
MoM	Method of Moments
PEC	Perfect Electric Conductor

RF	Radio Frequency
RFI	Radio Frequency Interference
RFS	Radio Frekwensie Steurings
RSA	Republic of South Africa
SA	South African
SG	Signal Generator
S-parameter	Scattering parameter
SKA	Square Kilometre Array
SMA	Sub-miniature version A
SOLT	Short-Open-Load-Through
VNA	Vector Network Analyser
XDM	Experimental Demonstrator Model

Contents

List of Figures

Chapter 1

Introduction

The ambitious goals of the international Square Kilometre Array (SKA) project, brings to mind the mission statement of the popular Star Trek series created by Gene Roddenberry: "To boldly go where no man has gone before".

This biggest and most sensitive project ever undertaken in radio astronomy, endeavours to probe to the edges of the universe. It will help to answer fundamental questions in astronomy, physics and cosmology, including the nature of dark energy and dark matter, as well as to explore the origins of the first galaxies, stars and planets [1]. An artist's impression of the international SKA is shown in Fig. 1.1.

1.1 Background

The Republic of South Africa (RSA) and Australia are now the two remaining countries bidding to host the SKA. A consortium of the major international science funding agencies,

Figure 1.1: *Artist's impression of the SKA, "the international radio telescope of the* 21^{st} *century" [2].*

in consultation with the SKA Science and Engineering Committee (SSEC), will announce the selected site for the SKA in 2012.

The South African (SA) SKA is demonstrating its technology capabilities through the Karoo Array Telescope (KAT or MeerKAT), currently under construction in the Karoo area of the Northern Cape province. The development of KAT is taking place in stages to optimise design and minimise risks at each stage. An interferometer array of seven 12 m antennas will be complete by the end of 2009, called KAT-7. The following phase will see the construction and commissioning of MeerKAT, which will lead to eighty arrayed dishes at the same site [1].

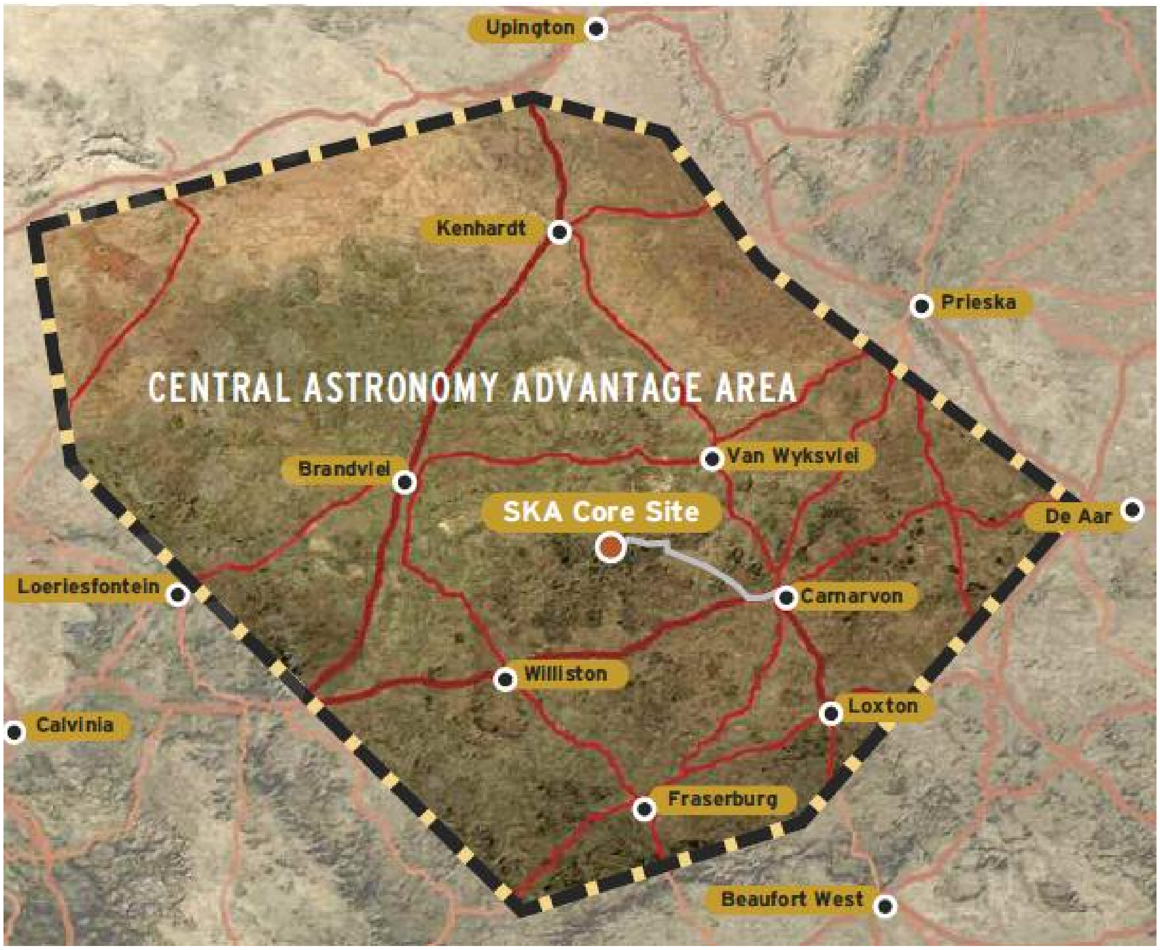

Figure 1.2: *Government proclaimed radio quiet zone in the Karoo, called the "Central astronomy advantage area" [1].*

1.2 Challenge: Radio Astronomy, Lightning Protection and Radio Frequency Interference Mitigation

To better convey the sensitivity needed for radio astronomy, the non-SI unit used by radio astronomers, jansky, is explained. Named after Karl Guthe Jansky, who was the first person to observe radio waves emanating from the milky way, the jansky is a measure of the spectral power flux density, or the "strength" of radio sources, and is defined as:

$$1\ Jy = 1 * 10^{-26}\ [W/m^2/Hz] \tag{1.1}$$

As an example, one of the strongest radio sources at 1420 MHz (except for the sun) is Virgo A, at 201.81 Jy. If a 26 m radio astronomy antenna were to point at this star for 30 years, 12 hours each day, the total collected energy (approximately 25 nWh) would still be a million times less than the energy a 100 watt bulb would consume in 1 second [1, 3].

Strong sources like Virgo A are well researched, so radio astronomers are more interested in sources within the milli-jansky range, and the SKA will probe the micro-jansky range and smaller. Because of this sensitivity of the antennas, the surrounding environment should preferably be radio frequency interference (RFI) free. Even static build-up on a nylon chair or loose hardware on a power line will interfere with the radio signals [3].

Considering these facts, it becomes clear that RFI can influence the measurements done by a radio telescope. This interference can enter the data stream at any frequency. Even if the interference is not at precisely the same frequency, the electronic receiver circuits can be driven into saturation, causing data corruption.

The SKA site in the Karoo chosen by South Africa is already relatively RFI free. To safeguard this advantage, the SA Government has proclaimed the site as a radio quiet zone (Fig. 1.2). The surrounding mountains also provide natural shielding from outside interference for the site.

However, there are still several possible causes of RFI with the introduction of the SKA into this environment, such as self-generated noise, coupling between neighbouring antenna systems and conducted noise through the power cabling and earthing systems. Direct and indirect lightning strikes (shown in Fig. 1.3) form an equivalently important part of the investigation. Some of the RFI aspects may be mitigated with good electromagnetic compatibility (EMC) design principles and proper implementation. The dissertation addresses these challenges in conjunction with specific aspects relevant to the lightning protection.

RFI coupling and lightning damage mechanisms need to be determined and mitigated. If RFI needs to be addressed at the digital signal processing stage, the electronic hardware increases in expense. The research considers the identification of areas in the design which

Figure 1.3: *Several lightning strikes, each typically conducting up to 300 kA (photograph taken by the author).*

are in need of RFI mitigation. Spectral analysis of lightning shows that there are frequency components up to 50 MHz. Most of the damage to systems is done at the low frequencies (kHz). RFI is more strongly coupled in the MHz frequency range. When developing measures to protect against both direct and indirect lightning, system EMC integrity is simultaneously improved. An illustration of this point is given in section 6.4.4, where by diverting lightning currents, interior coupling from exterior interference is reduced by more than 10 dB. Although this is demonstrated at 50 MHz, current diversion has implications for a wide span of high frequency signals. Lightning protection and interference hardening by current diversion are discussed in [4].

Where RFI and lightning problem areas in the design can be identified before implementation, a significant cost-saving can be achieved, especially when a total of 80 dishes for MeerKAT are considered. This is ever more true for the full SKA project. The research described in this dissertation gives practical contributions toward this goal.

The electronic systems also need to be protected against lightning overvoltages, and lightning-induced currents and fields. General surge protection is dealt with by the project contractors. What the doctoral research adds to the protection, is to use solid EMC principles to minimise RFI levels toward the inside of the pedestal, where the sensitive electronics reside.

At the KAT-7 stage of the project, time deadlines are strictly adhered to, and design parameters are continuously evolving as the manufacturing and construction of the antenna structures are carried out. These factors influence the decision on how the research is conducted, as time-constraints decree the level and speed at which valuable feedback on design changes need to be given for implementation on KAT-7.

1.3 Methodology: Computational Electromagnetics

Many lightning studies have been conducted in both the time and frequency domain. Each domain has specific benefits, depending on what is investigated. Lightning impulses can be accurately modelled, simulated and injected into a physical measurement setup. Time-domain measurements can be done with an oscilloscope, and the signals Fourier transformed to consider frequencies of interest.

For the investigations in this dissertation, the frequency domain was chosen. Working in the frequency domain, high dynamic range measurements are possible (as seen in section 5.4.2, Fig. 5.15). Specific frequencies can be used to investigate coupling mechanisms, identify current paths and apply good EMC principles for lightning protection and RFI mitigation.

If analysis were done in the time-domain, a Fourier transform of the results allows a comprehensive frequency study of the system. In some cases this is advantageous. However, in a measurement environment, an oscilloscope is necessary to replicate these measurements. An oscilloscope has inherently low dynamic range. In EMC studies, instead of analysing all frequencies, a single frequency in a high dynamic range measurement system often yields principal issues. In particular, interface integrity is readily identified. For example, a cable penetrating a galvanic barrier which does not make 360 degree contact, will allow exterior currents through the barrier at all frequencies. This test is not frequency specific. It can be argued that in a complex system, such as a radio telescope, all possible frequencies should be tested. In practice, specific resonant frequencies will change from one system to another by the movement of a single cable. In our research, we have opted to focus on system principles with high sensitivity measurements to identify specific areas of concern.

Instead of considering the whole array of seven antennas as a complete system, only one dish design is investigated. FEKO [5], a Method of Moments (MoM) based frequency domain code, is used for numerical modelling of the design due to the code's computational speed with conductive wires and surfaces. Simplified geometrically scaled numerical models in FEKO (following scaling principles discussed in [6, 7]) are verified by rigorous scattering parameter (S-parameter) measurements of physical scale models in an anechoic chamber, using high-dynamic-range measurement equipment. The frequency range of investigation is determined by the relevant equipment capabilites (e.g. anechoic chamber from 500 kHz) and CEM code computational requirements at higher frequency (above 6 GHz, the simulations become computationally expensive). Additional verification is done with a finite volume time domain (FVTD) code, CST [8].

With the inclusion of a Sommerfeld integral ground plane in FEKO and dielectric material in CST, soil can be considered in a numerical model. Verification is done by adding a saltwater mix with the correct conductivity to the corresponding physical scale model and taking S-parameter measurements.

The verified numerical model following the KAT-7 design gives accurate predictions of lightning induced current paths and electromagnetic (EM) field levels for the complete structure. Direct lightning strikes are modelled with a direct current injection onto the numerical model, and an indirect strike is modelled using EM plane waves from different directions.

Coupling levels for different lightning down conductor (LDC) designs are compared to each other to decide on cost-effective solutions for KAT-7. Specific surface current and electric field results are not considered, but comparative levels are used together with solid EMC design principles to select the best options for lightning protection and RFI mitigation. Keeping within the frequency limits of the available equipment, CEM codes and actual lightning frequencies, the high-frequency component of lightning at 50 MHz was chosen as a representative frequency for investigations. This principle has been used in lightning investigations within South Africa's power utility, ESKOM.

AdaptFEKO is used to evaluate worst case coupling levels for these designs at resonant frequencies, and areas that require RFI mitigation are identified.

Following lightning protection standard [9] good practices on earthing, the steel reinforcing of the concrete foundation for the structure is bonded to the earthing electrode. The effectiveness of the interconnection of the steel reinforcing elements are evaluated in FEKO by including the Sommerfeld integral ground plane in the numerical model.

1.4 Claims and Original Contributions

The KAT-7 structure consists of three main elements as shown in Fig. 1.4, the dish, the pedestal and the foundation (including earthing). The original KAT-7 design incorporated clear lightning protection and RFI mitigation policies derived from recommendations contained within this dissertation. However, mechanical construction of complete structures must be regarded as the primary design criteria. During the construction process the structure was fabricated with environmental conditions in mind. Specifically this led to main surfaces and interfaces being protected by either gun-coating or paint, which directly compromised the galvanic integrity of the entire system.

This dissertation presents original design contributions for lightning protection and RFI mitigation for KAT-7. This has had a significant bearing on South Africa's intended demonstrator for the world's largest radio astronomy project, the SKA. The contributions

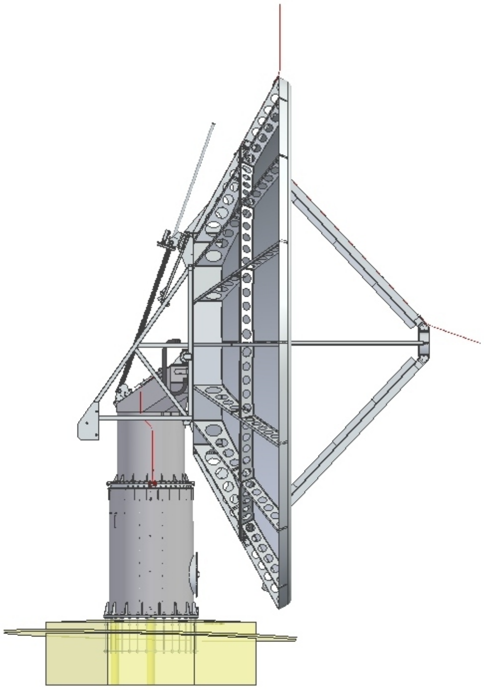

Figure 1.4: *The structure consists of three main elements: the parabolic dish, the pedestal on which the dish is mounted, and the steel reinforced concrete foundation.*

have been tested using the computational electromagnetic code, FEKO. The validity of this approach has been established through extensive checking of physical and computational scale models. The following principal claims are made concerning:

Method of lightning excitation in models

- At the 2008 URSI conference [10], the validity of a simulated lightning current injection measurement was brought into question. Our modelling has shown how this injection method does influence the measurement. However, when used according to recommendations in [11], the method is presently deemed to be valid. The author has demonstrated an improvement on the method by taking the excitation conductor connected to ground on four different sides. This is shown to give a more symmetrical injection current which does not influence the levels on one side only (see section 6.6.2). Additionally, a plane-wave excitation technique has been introduced for comparison.

The lightning down conductor design

- Using verified CEM scale model simulations of different strapping connections over the elevation bearings of the KAT-7 dish, the author has shown that straps connected below the elevation bearing axle provide better protection for the bearings at higher frequency. This involves a cost-saving for the project, with shorter straps being sufficient.

- When the LDC over the azimuth bearings was considered, coated surfaces and static-bearing roller elements are taken into account for modelling. The author has shown the influence that these coatings have on capacitive coupling levels and RFI toward the inside of the pedestal structure. Using copper shoes, corrective bonding and alternative termination of the lightning conductors, a considerable improvement was made for the distribution of surface currents around the azimuth bearing. Coupling levels toward the inside of the pedestal were reduced as well.

Identification of resonances

- A demonstration was given of how the FEKO program AdaptFEKO can be used to identify structure resonances for a defined frequency range. This will enable investigations into a pedestal, fully populated with equipment and cabinets, to highlight areas requiring RFI mitigation.

The lightning earthing electrode design

- Project cost and time are saved by evaluating the inclusion of the foundation reinforcing as part of the lightning earthing system. This eliminated the need for welded interconnection of all metallic elements of the reinforcing, which can take up to three days per structure. The findings were achieved with MoM code combined with a Sommerfeld integral ground plane and simulated soil below.

1.5 Dissertation Layout

Chapter 2 of this dissertation discusses published literature on lightning protection and modelling, scale models and measurement, as well as computational electromagnetic (CEM) codes used for investigating lightning and RFI in structures above and below ground. The design, construction and verification of the first scale model used in this research is detailed in chapter 3. A consequent design scale model is used to refine investigation methods to include soil conditions in the model (chapter 4). The 5^{th} chapter considers the detailed physical scale model of KAT-7 and the verification of the computational scale model for current injection and plane wave excitation.

Using the verified KAT-7 scale model in FEKO, detail and results on lightning excitations and investigations into the lightning down conductor design can be found in chapter 6. AdaptFEKO is used to consider resonant frequencies to identify areas requiring RFI mitigation. Specific studies toward optimal earthing connections of the KAT-7 foundation steel reinforcing, using FEKO together with a Sommerfeld integral ground plane, are shown here as well.

Finally, chapter 7 concludes the dissertation with an evaluation of the contributions of this research to KAT-7 and recommendations on future work for MeerKAT. This is followed by the bibliography.

– *Whether you believe you can do something or not, you are right* –

– *Henry Ford* –

Chapter 2

Literature Review

In this review chapter, important aspects of existing literature related to this dissertation are highlighted. Basic principles of the RFI mitigation plan, and where they fit into the lightning protection for this project, are explained. The current focus for modelling of lightning is mentioned, and the application of certain methods previously used are discussed. The use of numerical electromagnetic modelling to evaluate the current and electric field behaviour of a lightning protection system during a lightning strike is detailed. Scale model measurement verification of such numerical models, plays an important role in the level of confidence that can be placed in the computational results. With the unique requirements in radio astronomy radio frequency (RF) engineering, the implementation of our contribution toward the lightning protection and RFI mitigation on KAT-7 is given.

2.1 Introduction

Considering all the aspects involved in the design of lightning protection and RFI mitigation of a very complex system, it is clear that a systematic approach is essential. The main trait that sets this project apart from any other, is the level of RFI protection that is needed due to the sensitivity of the radio astronomy equipment (see section 1.2). The possibility exists to eliminate the effects of RFI in the received radio signals through digital signal processing, but with the sheer amount of antenna dishes for the project, that option is eliminated from a cost perspective. The computing power and storage capacity for this alternative for the full SKA is not even available at present. The most expedient method to ensure effective RFI mitigation, is to complement the design of the lightning protection system with solid EMC design principles in order to minimise RFI coupling toward the sensitive instrumentation inside each structure.

2.2 RFI Mitigation Plan

Practical guidelines on EMC management can be found in [12, 13, 14, 15]. Key items for a complex system is that EMC issues need to be clearly identified, defined and controlled. The identification of critical aspects for system susceptibility and electromagnetic interference (EMI) or RFI mitigation, control of assembly and installation, as well as defining the tests to be done, all form an important part of the control plan.

2.2.1 Identifying the Risk

With the proclamation of the core area in the Karoo as a radio quiet site, lightning was identified as one of the possible environmental sources of interference. Low frequency lightning induced currents and voltages from both direct and indirect strikes may lead to equipment failure and even loss of life. This is mainly governed by international standards on lightning protection. Higher frequency induced currents and voltages may interfere with the data-streams of the radio astronomy observations, and here RFI mitigation plays an important role.

The standards on protection against lightning [16, 17] give information regarding the basic parameters of lightning current, lightning coupling mechanisms, lightning threat parameters, protection levels and the determination of cost-effectiveness of the lightning protection system (LPS). The method of risk assessment for damage to structures, failure of equipment or loss of life, and the management thereof, are explained in [18]. Clear guidelines on specific requirements for the lightning air terminations, LDC and earth termination system are stipulated in [9]. The lightning protection of electrical and electronic equipment inside structures is dealt with in [19]. This chapter will not go into the detail of these factors, but will only highlight some of the issues relevant to RFI mitigation on the KAT-7 structures.

2.2.2 Characterising the RFI Source

At the early stages of the research, several international radio astronomy observatory sites were visited to discuss existing EMC, lightning protection, and earthing policies. This included Astron, Westerbork Sterrenwacht and Low Frequency Array (LOFAR) in the Netherlands, as well as Jodrell Bank Observatory and Manchester University in the United Kingdom [20]. These discussions helped to focus on the main issues that are of concern, including current paths, earthing and the relevant aspects of shielding.

To understand the risks involved with direct and indirect lightning strikes on the LPS of a structure, the above-mentioned International Electrotechnical Commission (IEC) standards were reviewed. In [16] the parameters of lightning current are explained. Light-

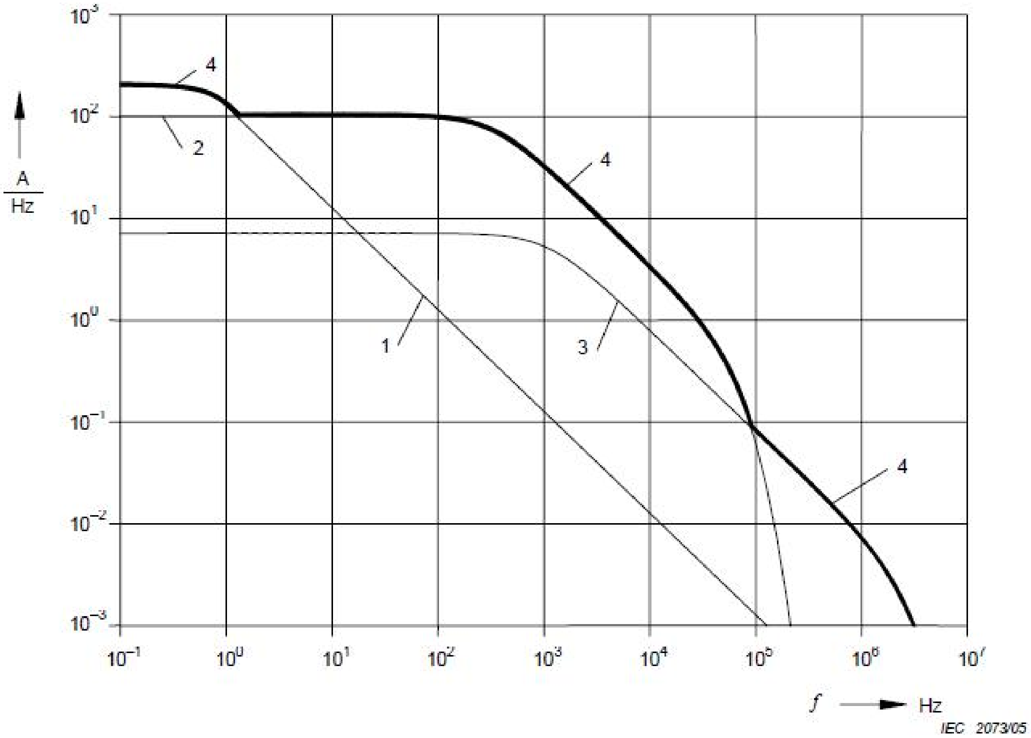

1	Long stroke	400 A	0,5 s
2	First short stroke	200 kA	10/350 µs
3	Subsequent short stroke	50 kA	0,25/100 µs
4	Enveloping curve		

Figure 2.1: *Amplitude density of lightning protection level 1 current against frequency [16].*

ning flashes to earth can be downward or upward flashes, initiated by either downward leader from cloud to earth, or upward leader from an earthed structure to cloud. The lightning current can consist of one or more long or short strokes. These strokes have different time-pulse characteristics. A stroke consists of a current curve rising to a peak value in a short time interval, and then decreasing over time to zero value. The front time is defined in the standard as the time interval from 10 % to 90 % of the peak current value, and the time to half value as the time from a virtual origin to half the peak value when the current is decreasing. The different strokes, combined to form a lightning strike, give rise to a frequency content as seen in Fig. 2.1. The figure shows the maximum current amplitude density as a function of frequency. From the envelope curve one can see that the higher frequency content up to 50 MHz is mainly due to short strokes subsequent to an initial short stroke. The subsequent short stroke has a front time of 0.25 μs, and a time to half-value of 100 μs.

To simulate the effects of lightning on a lightning protection system, test parameters similar to the peak current values shown in Fig. 2.1 are used to calculate the current levels to which the LPS will be subjected during direct strikes. Both direct and indirect lightning strikes can induce currents on other parts of the structure. Different coupling mechanisms are detailed in [17], of which resistive coupling and magnetic coupling have the greatest influence. A lightning discharge to an object creates a potential rise reaching several hundreds of kV at the point of impact with respect to remote earth, generating currents that are distributed amongst conductive paths which are bonded to the reference point of the system. For indirect lightning, magnetic fields are created by the lightning discharge channel, having approximately the same time variation as the current at distances of hundreds of metres. The magnetic field variations induce voltages and currents in conductive paths on a structure.

In [18] the risk assessment of lightning is discussed in detail. Parameters that influence the calculation, are the lightning flash density of a specific area, as well as the collection area of the structure. A map of the lightning flash density for South Africa is given in Fig. 2.2. The core area for KAT-7 and MeerKAT has a flash density of approximately two to three lightning strikes per square kilometre per year. To ensure that the lightning protection is cost-effective, a calculation has to be done to compare the cost of loss with no LPS, versus the cost of the LPS plus the cost of possible loss with the LPS installed.

With the amount of structures planned for MeerKAT and the SKA, the probability of a lightning strike exists. With the high levels of lightning current and risk of RFI to sensitive equipment inside the structure, we decided to incorporate an LPS in the design. However, cost-effectiveness remains the principal design constraint.

2.2.3 Computational Modelling

To simulate the effects of a lightning stroke, one of the International Telecommunication Union (ITU) recommendations for protection against interference [11], recommends the Method of Moments. This approach has been successfully used in literature [21, 22, 23]. Numerical models are preferred above measurement methods for situations where experimental reproduction of interference is difficult [23]. The radio astronomy sites where this project's telescopes will be installed, are all radio quiet zones. This eliminates the measurement methods as proposed by [24, 25], using an electromagnetic pulse (EMP) simulator as a lightning simulation.

When using computational modelling, verification of the code is done with measurements to validate the numerical calculations [22, 24, 26]. The use of scale models enables these measurements to be done in a controlled environment [22, 24, 25, 27, 28]. However, we did not have access to equipment such as EMP simulators [24, 25] to use for experimental validation of our computational code.

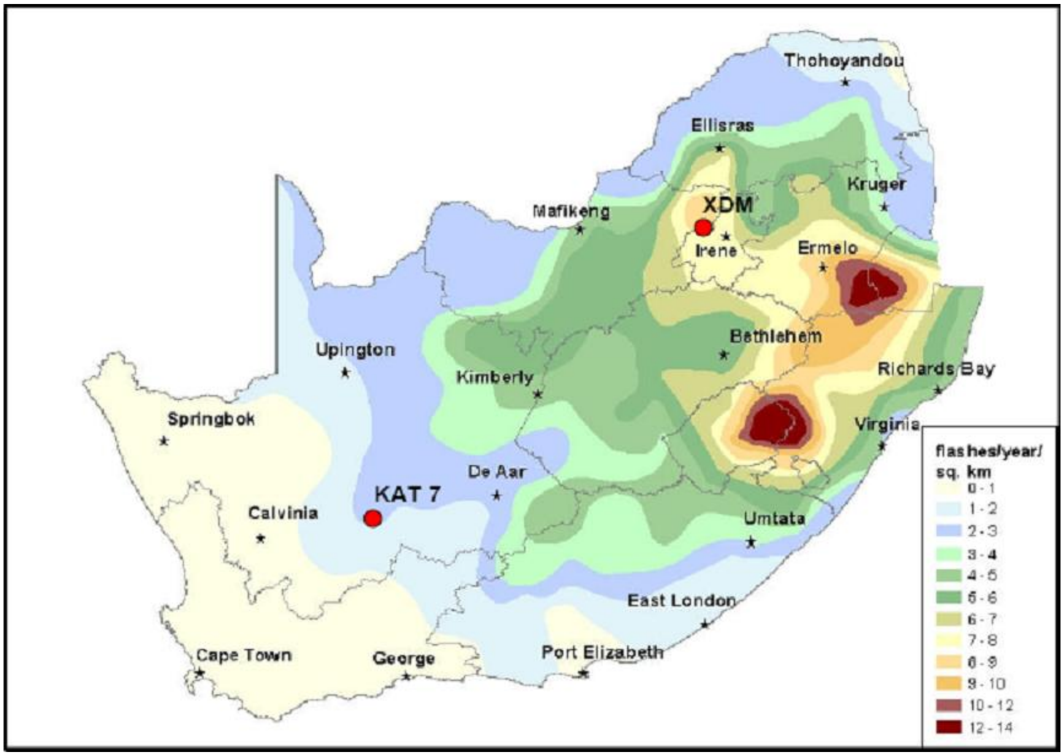

Figure 2.2: *Lightning flash density map for RSA, showing the location of XDM and KAT-7.*

Equipment available to us, was a Hewlett Packard two-port vector network analyser (VNA) and an anechoic chamber. S-parameters can be measured on devices inside the chamber using the VNA in the frequency range from 300 kHz to 18 GHz.

With the MoM used in the frequency domain, and the available equipment able to do accurate frequency domain measurements, the MoM based code FEKO was selected for our simulations. Doing analysis in the frequency domain enables investigations at frequencies which are of specific interest. To evaluate electromagnetic fields and currents on the KAT structure due to external RFI from lightning, the modelling was done at the highest probable lightning frequency of 50 MHz.

A finite difference time domain (FDTD) or finite volume time domain code can be used for lightning analysis as well [22, 29], and to evaluate specific frequencies require mathematical manipulation of the results using Fourier transforms [22]. This function is available in the FVTD based code, CST [8]. The code is used in our work to compare the MoM results at the verification stage of this project. Detail on the MoM can be found in [5, 30] and the FDTD and FVTD methods are explained in [8, 30].

2.2.4 Lightning Excitation and Scale Models

Extensive modelling has been done in the time domain of the lightning return stroke channel and current [6, 31, 32, 33]. One paper discussed this lightning excitation using a thin-wire antenna model [34]. The source used for the modelling is typically a voltage source tuned to provide a specific current impulse [21, 35, 36].

To verify the modelling, scale models are constructed with impulse generators as the main excitation [37, 38, 39]. The current injection simulating a direct strike is constructed on the scale model as a vertical wire onto a specific part of the scaled structure [22, 39]. Detail on how to incorporate the scaling factors to real values are given in [6]. However, an interesting observation from [40] states that care should be taken when relating scale model parameters to real parameters. Conductivity has to be scaled as well, and with a scaling factor of four for example, that involves a scaled conductivity of four times the real value [6, 7, 40]. Additionally, relative permittivity does not scale according to the scaling factor, thus making the use of dielectric in a scale model difficult to relate to real models with dielectric [40]. Scale model parameters can, however, be replicated in numerical models.

A recent progress overview of lightning modelling in [29], relates several interesting uses of computational modelling. One example is simplification of the model using perfect electric conducting (PEC) ground plane. To evaluate the effect of finitely conducting soil on electromagnetic fields at the air-soil interface, more precise modelling is done using the Sommerfeld integral [29, 41].

A final observation on the lightning excitation is made from [11]. A test setup to simulate lightning effects for modelling and measurement is given. The earthing of a structure is used as a return path connected to the earth of the lightning excitation. Here it is warned that the position of the excitation conductor can influence the measurement of induced voltages inside the structure. This is shown with an example done at a constant frequency with constant continuous wave (CW) current excitation.

Some practical issues regarding the LDC design for wind turbines is discussed in [42], explaining the influence of indirect lightning strikes as well. This shows the need to model indirect lightning strikes for models.

2.2.5 Lightning Protection System

In [43, 44], realistic models of European Space Agency (ESA) launch vehicles and their lightning down conductors are replicated in numerical models to study the lightning protection system. Specifically, [43] refers to the lightning qualification logic applied to the ARIANNE 5 launcher, complying with technical efficiency, cost and schedule constraints.

The modelling in [44] assumes perfect connections for all steel elements in their simulations. However, where there are discontinuities in the structure, and the lightning current path impedance changes, reflections of the lightning impulse may occur [21]. These reflections in the time domain can be related to resonances in the frequency domain, for which [45] explains how radio frequency resonances and nulls are influenced by reinforced concrete construction.

The suggestion is made in both [44, 46] that the entire LDC system be incorporated in modelling. For their simulations, finite-conductivity soil is included in the numerical calculation. With the inclusion of soil conditions, the modelling takes underground and above-ground fields which are influenced by the finite ground conductivity into account [32, 47]. This is done accurately using Sommerfeld's integral equations [41].

Further modelling has been done on lightning currents to ground for power line towers [48], modelling of grounding electrodes under lightning currents [49, 50], and the effect of lightning current injection on ground mesh and buried bare wires [51, 52]

Here the focus for the project is shifted to the bonding and interconnection of the earthing to the lightning protection system as discussed in the IEC standard [9]. The standard requires that all steel elements of a structure be connected to, and where possible, utilised as part of, the LDC. Where steel reinforcing is used in concrete foundations, the steel elements should be welded or securely bound [9, 53].

2.3 Conclusion

With the information from this survey, a good foundation was laid to investigate the lightning protection and RFI mitigation of KAT-7 by using numerical modelling. Verification of the modelling forms an important part of the research, which allows the computational code to be used with confidence for the relevant lightning and RFI studies.

– It takes less time to do things right, than to explain why you did it wrong –

– Henry Wadsworth Longfellow –

Chapter 3

Verification of FEKO Scale Model

The following chapter explains how a simplified $1/40^{th}$ scale model of an early design of KAT was constructed, replicated in a MoM code, FEKO, and verified with measurement. A FVTD code, CST, is used to evaluate both the FEKO and the measured results.

3.1 Introduction

The MoM-based CEM code, FEKO, is chosen due to the code's computational speed with dominantly metallic structures, open boundaries and minimal dielectric.

To be able to trust the computational modelling, verification of the code is essential. However, where experimental validation is not practically possible, scale models allow a more controlled environment to conduct measurements [24].

The operational band for an early design of KAT falls within the 700 MHz to 1750 MHz range [1]. The available anechoic chamber absorption is best between 2 GHz and 18 GHz for measurements. A scaling factor had to be chosen accordingly. Frequency is scaled proportionally [6, 7], and we chose a scaling factor of 40. For the scale model, measurements were only done between 2 GHz and 6 GHz, corresponding to 50 MHz to 150 MHz in real terms. The lower frequency is limited by the chamber absorption and the upper frequency limit was chosen to stay within the computational power available. The main purpose of this work was to do the CEM code verification. It is not important to cover the operational range precisely, as principal current paths can be identified at any reasonable portion of a high frequency band.

Placing an excitation port and a pick-up loop on the device under test, eliminates the need for invasive probes. An S-parameter measurement between the two ports gives an accurate definition of both ports' reflection characteristics with S_{11} and S_{22}, as well as the coupling between them using the transmission coefficient S_{21}. With careful calibration of a 2-port VNA, rigorous measurements can be made of these S-parameters. The setup is easily replicated in the computational code up to the calibration planes. This gives an

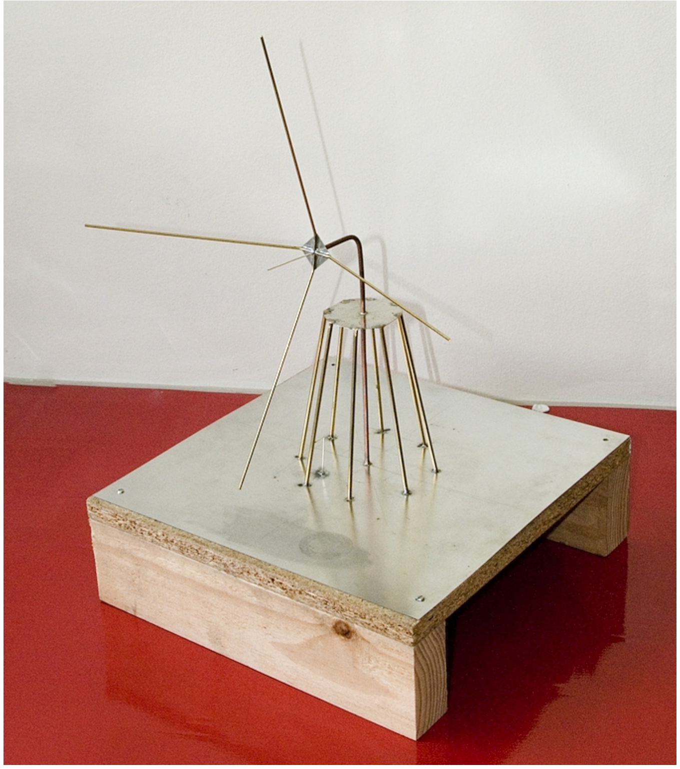

Figure 3.1: *Photograph of the first scale model following an early KAT design.*

accurate verification of the computational code in order to use the model for further RFI studies.

A FVTD-based code, CST, is used to evaluate both the FEKO and the measured results. Through comparison of both codes' results to each other and to the measurement, this forms a comprehensive authentication for the modelling used.

3.2 Early Design $1/40^{th}$ Scale Model

The electromagnetic environment inside a building can systematically be analysed using a simplified wire model of the steel reinforcing and lightning protection down conductors only [23, 28]. An early design of KAT was planned using steel-reinforced concrete for the structure, and a composite material for the parabolic dish, mounted on metallic struts. From [9], the steel elements of a structure can also be used as part of the lightning down conductor (LDC) system. Thus we simplified the design for the scale model to contain only the main metallic struts and surfaces of the pedestal structure and the dish. The complete model is mounted on a conducting ground plane and shown in Fig. 3.1.

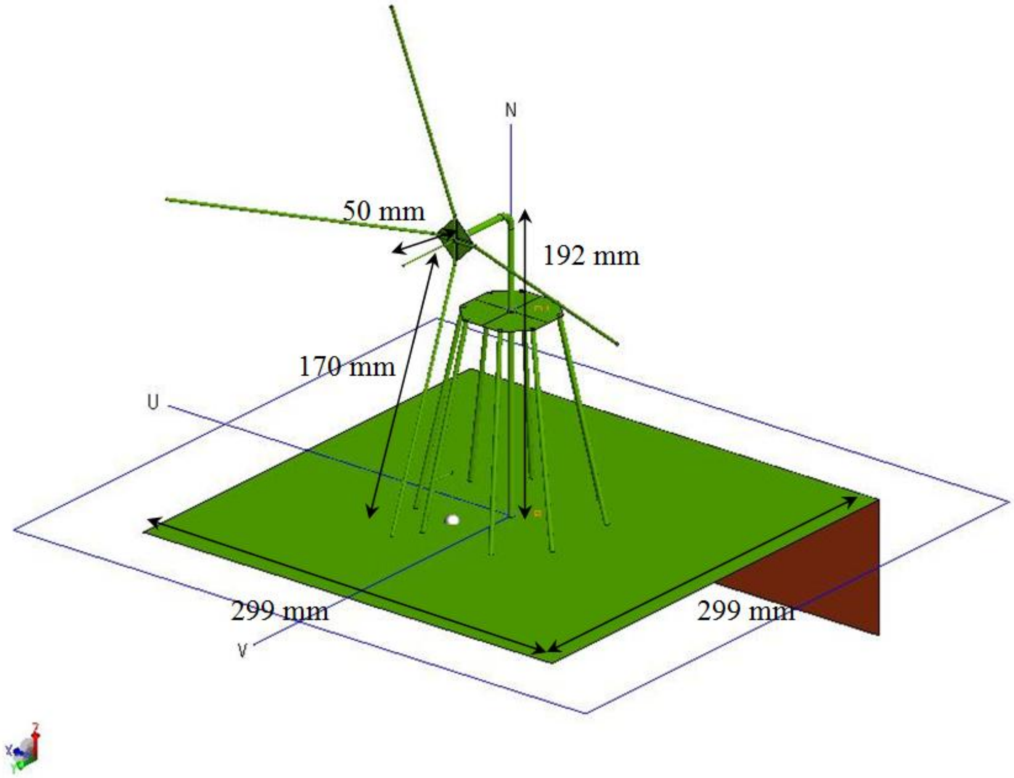

Figure 3.2: *FEKO model of the early KAT design, with basic dimensions.*

3.2.1 Physical Scale Model

The first 1:40 scale model is constructed using brass rods, semi-rigid cable and thin conductive metallic plates. One port in the bottom centre of the structure connects the dish to the core wire of the semi-rigid cable which goes through the centre of the structure. The core wire at the top was stripped from the dielectric and outer copper sheath, and forms a monopole onto which the dish, which is represented by four wires on a small plate, was soldered. Another port's core wire forms a pick-up loop at one of the struts going down to the earth, adjacent to one of the dish-wires. The area where this core wire is stripped of the dielectric, is flush with the ground plane plate. Sub-miniature version A (SMA) connectors attach the semi-rigid cable entry to the model from its underside, defining the calibration plane, and allowing minimally invasive S-parameter measurements of the model.

3.2.2 FEKO Scale Model

Careful measurement of the scale model wire thickness and lengths yielded the exact dimensions to be used in the FEKO model. The thin-wire approximation of the MoM code is not applicable to the relatively thick brass rods used on the model, especially in the 2 GHz to 6 GHz frequency range. Accordingly, the geometry was represented by solid

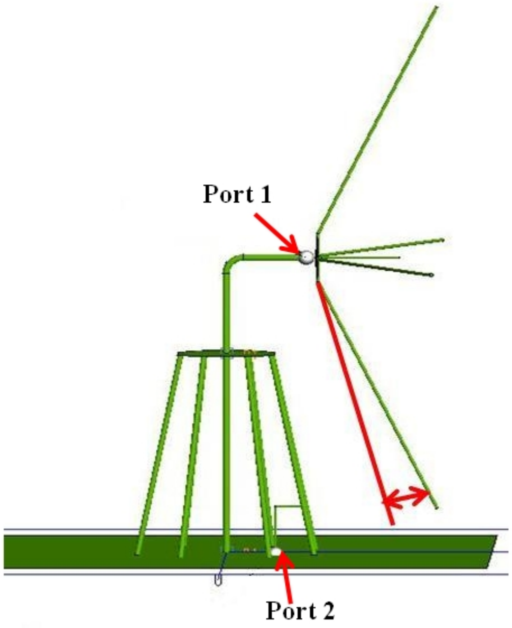

Figure 3.3: *FEKO model showing the excitation ports and the dish wire which was bent out of place in the direction indicated.*

cylinders of the exact dimensions.

The excitation port of the semi-rigid core wire onto the dish was simplified by placing the FEKO thin wire discrete voltage port at the interface where the core wire is stripped from the dielectric and outer sheath. This eliminated the need for modelling the dielectric, which is computationally expensive using the MoM code.

The pick-up loop's port was defined as a 0.5 mm length thin wire discrete voltage port between the ground plane and the loop itself. Both ports were defined with a 50 Ω impedance, representing the characteristic impedance of the VNA and the cables. They are indicated on Fig. 3.3. This enables FEKO to calculate S-parameters equivalent to the VNA measurement.

When we modelled the ground plane as an infinite perfect electrically conducting (PEC) plane, it was found that resonances associated with its dimensions were not present. Therefore the ground plane plate was also accurately defined in the FEKO model. It did, however, increase the computational time. Thus an accurate approximation of the MoM code, the multilevel fast multipole method (MLFMM) was utilised to speed up the solution.

After initial measurements of the physical model was made, it was found that the dish of the model is too heavy for the semi-rigid core wire, causing the dish to sag during handling. The lower dish-wire is consequently in closer proximity to the wire which connects to the pickup loop. When the semi-rigid core wire supporting the dish was bent

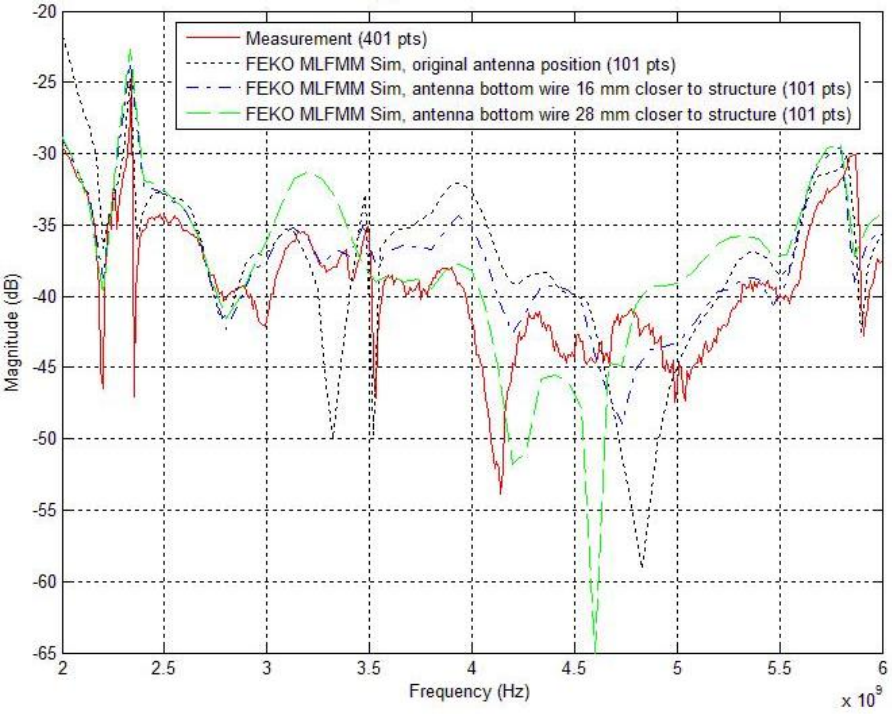

Figure 3.4: *Variations of FEKO results for S_{21} according to changes in dish geometry.*

higher or lower by approximately 10 degrees, a difference of signal level was seen and resonances changed significantly with the change in position of these wires. This change was successfully replicated in FEKO by adjusting the angle of the dish-wire by 10 degrees downwards and upwards respectively (see Fig. 3.3). The change in coupling between the two ports is shown by the S_{21} results in Fig. 3.4.

For MoM discretisation in the frequency range of 2 GHz to 6 GHz, the triangle edge size was chosen to be most efficient at 4 GHz, but within the parameter limits for 6 GHz. This resulted in 8,168 metallic triangles and 2 metallic segments in free space that had to be computed. The discretised triangle mesh is shown in Fig. 3.5. A simulation of 101 discrete frequency points took approximately seven and a half hours to run on a four-core processor with 15 GB of memory available.

3.2.3 Verification by Measurement

The S-parameters are measured using a two-port Hewlett Packard 8510 vector network analyser (VNA) connected to the model via two phase stable cables leading into an anechoic chamber. A diagram showing the measurement setup of the physical scale model in the anechoic chamber can be seen in figure 3.6.

The VNA was calibrated between 2 GHz and 6 GHz with 401 discrete points. A short-open-load-through (SOLT) procedure was used for calibration, where the connection point

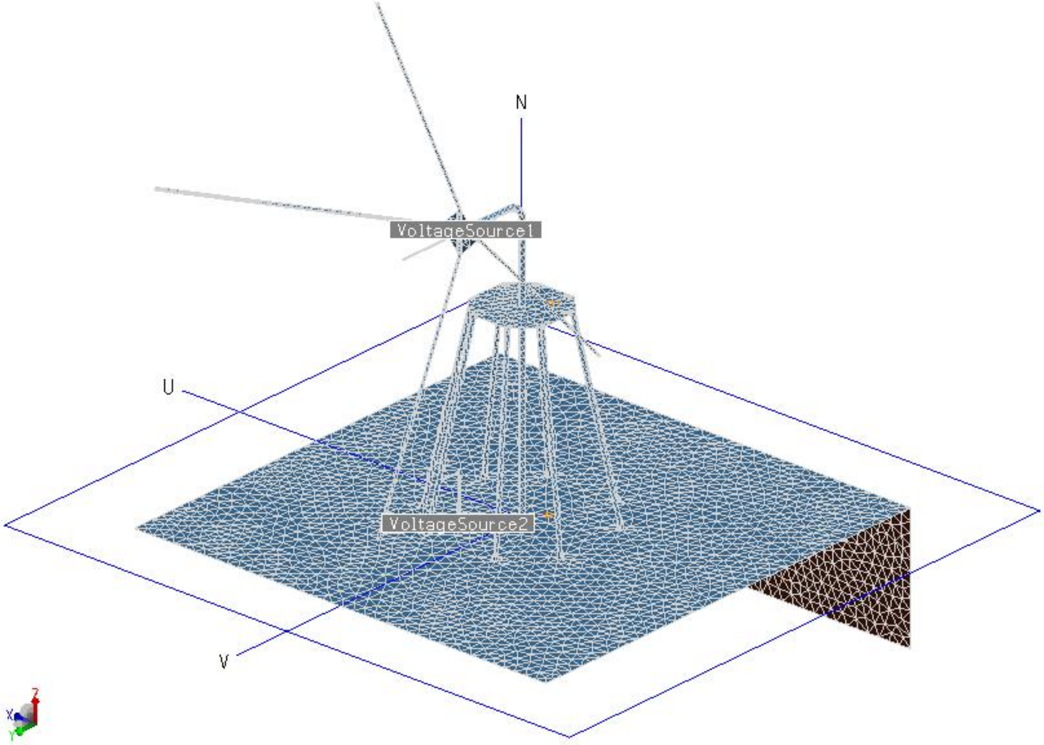

Figure 3.5: *Discretisation mesh of the FEKO model.*

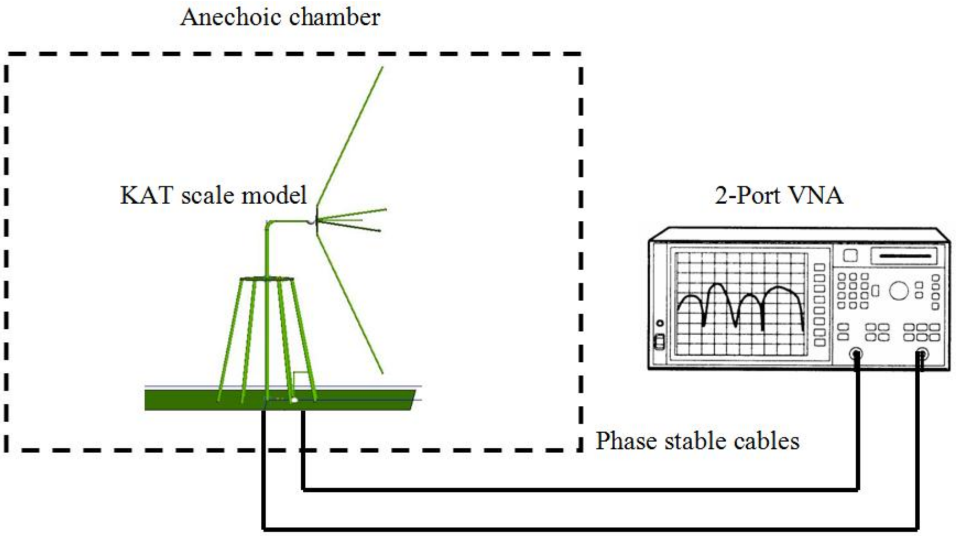

Figure 3.6: *Diagram of the measurement setup in the anechoic chamber.*

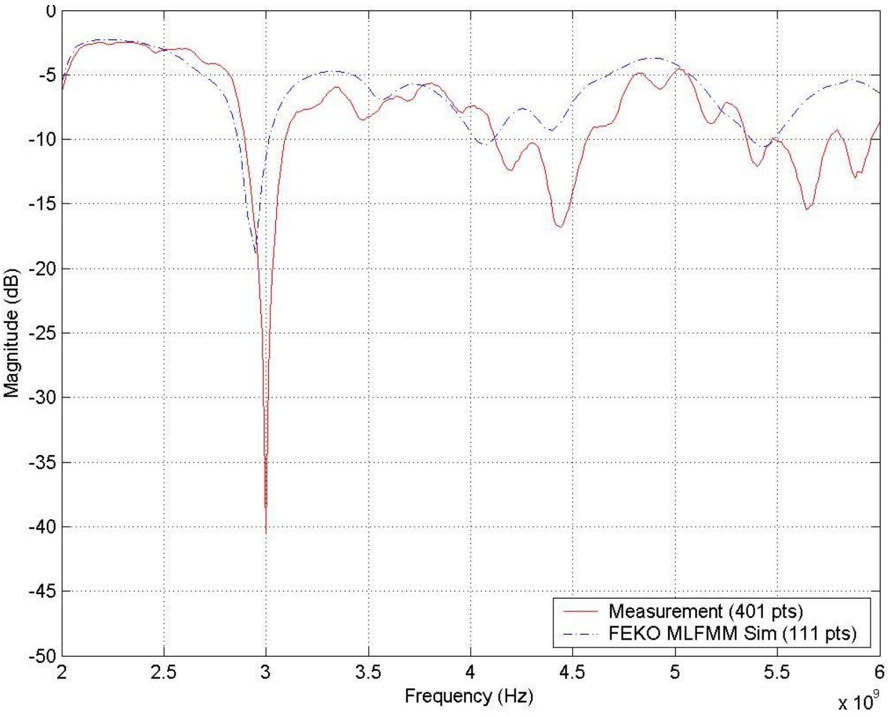

Figure 3.7: *Comparison between the measured and FEKO results for* S_{11}.

of the phase stable cable to the model sets the calibration plane. The measurement was carefully taken between the set frequencies and the results recorded to file for all the S-parameters. Measurements were taken under identical conditions on a second occasion, proving repeatability of the measurement.

The S-parameter results were saved to file and the data extracted. MATLAB plots were made to compare the measured results to the simulated results of FEKO. The comparison between the S-parameter magnitude results are given in Fig. 3.7 to Fig. 3.9.

The comparison of the measurement and FEKO results for S_{11} in Fig. 3.7, show that the plot for the FEKO simulation is in the same dB-range as for the measurement, but not following the shape precisely. The resonance is off-set by 61.5 MHz from 3 GHz, showing a difference of 1 mm in the length of the semi-rigid core-wire. The wire acts as a monopole at the tip of the dish and is the cause for the major resonance at that frequency.

Considering S_{21} as seen in Fig. 3.8, the lower end and higher end frequencies show that the measurement and FEKO simulation are in close agreement. Although variations are limited to around 5 dB in the 3.5 GHz to 5 GHz range, the strong radiation characteristics of the dish-wires while easily being bent, make a good comparison between the measured and simulated results difficult.

The result for S_{22} in Fig. 3.9 shows the best correlation between the measurement and the FEKO results. The differences between the values are less than 0.5 dB, except in the areas of resonance. The main resonance at 3.9 GHz is the resonant frequency for

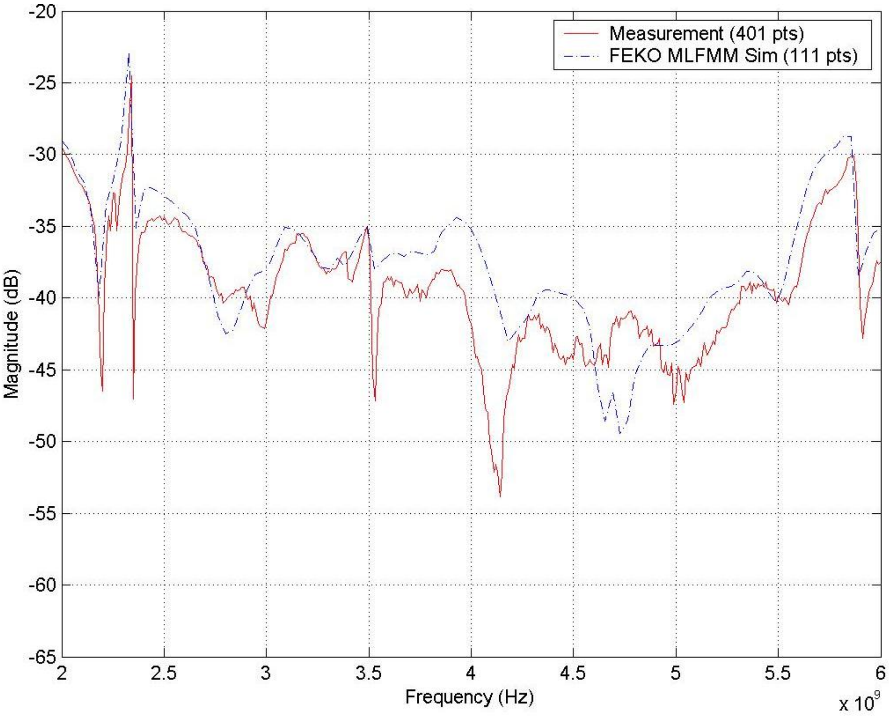

Figure 3.8: *Comparison between the measured and FEKO results for* S_{21}.

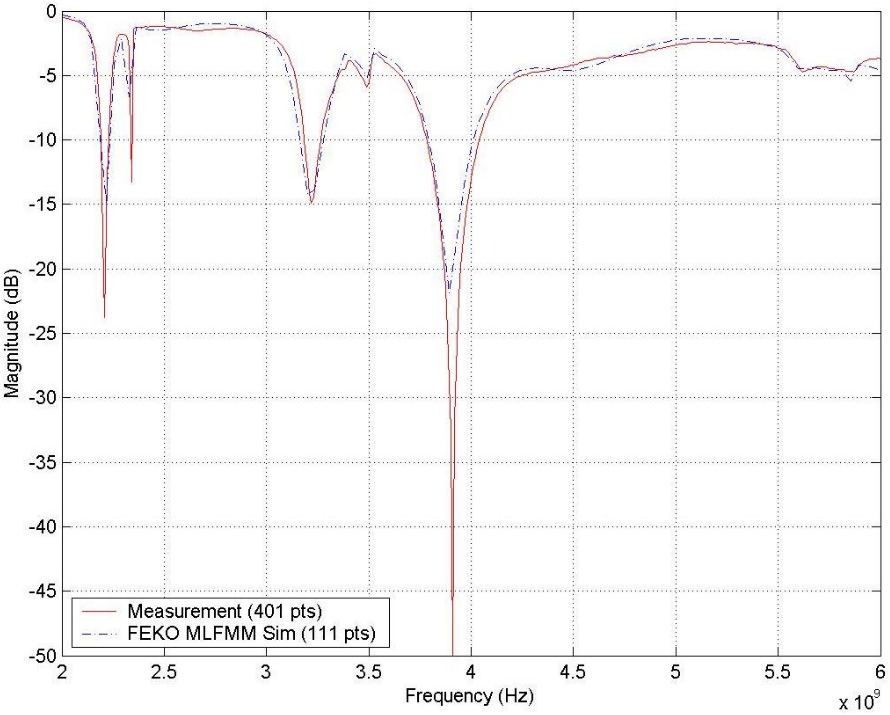

Figure 3.9: *Comparison between the measured and FEKO results for* S_{22}.

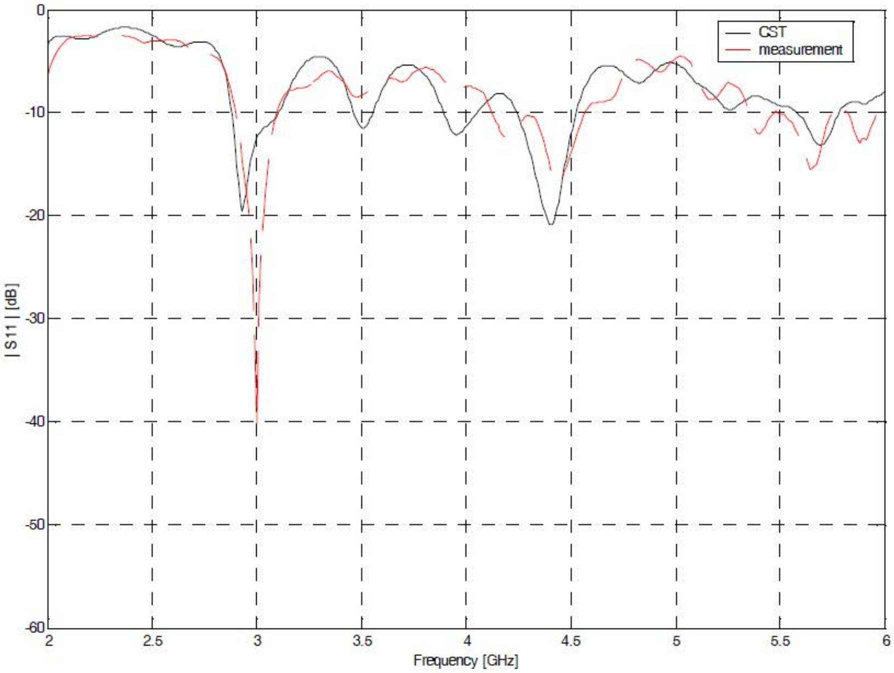

Figure 3.10: *Comparison between the measured and CST results for* S_{11} *[54].*

the small loop antenna of port 2.

An important observation made during the measurements, is that when chokes are placed on the measurement cables, the magnitude of the S-parameter resonances change slightly. This indicates that some stray currents are present on the outer sheaths of the measurement cables, originating from the ground plate of the model. To make an improvement on future models, EM barriers can be incorporated in the model design.

3.3 Evaluation with CST Code

Running parallel to this research project, another project by a postdoctoral fellow on a related topic, used CST for safety-related investigations on the KAT design [54]. The same physical scale model S-parameter measurement was used to validate the numerical model in CST. Open boundaries were used for free space and electric boundaries for the ground plane. The geometry was constructed in a similar manner to FEKO, and the two ports were also defined as discrete voltage ports with 50 Ω impedance. With these values set, the whole volume containing the model was discretised to form a mesh. The transient solver in CST was used to calculate a time-domain response which is then Fourier transformed to calculate the frequency domain S-parameters.

The magnitude comparison between the CST and measured results are shown in Fig. 3.10 to Fig. 3.12. The CST plots match the FEKO plots almost exactly. Minor variations in the shape of the plot are attributed to the Fourier transform of the CST

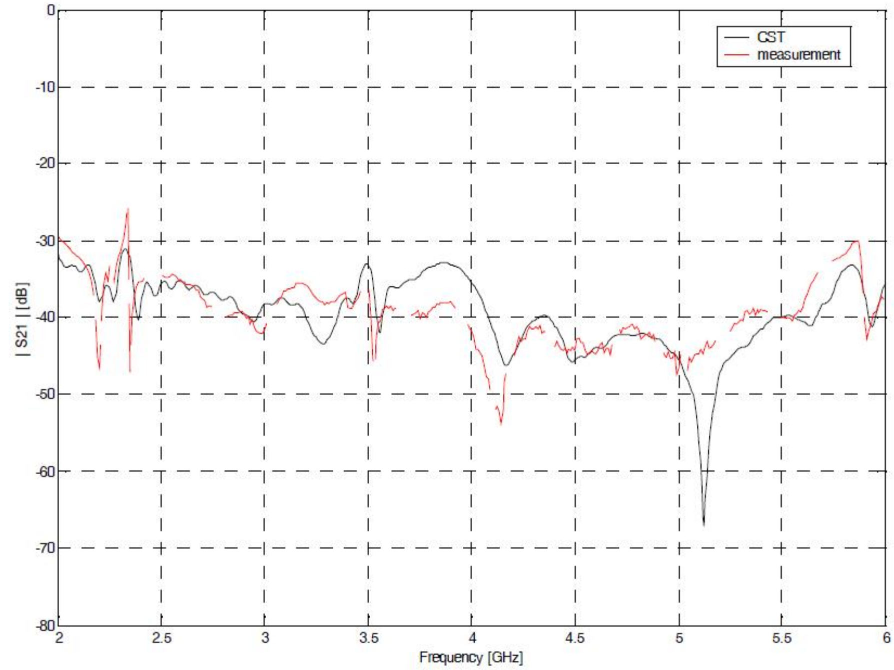

Figure 3.11: *Comparison between the measured and CST results for* S_{21} *[54].*

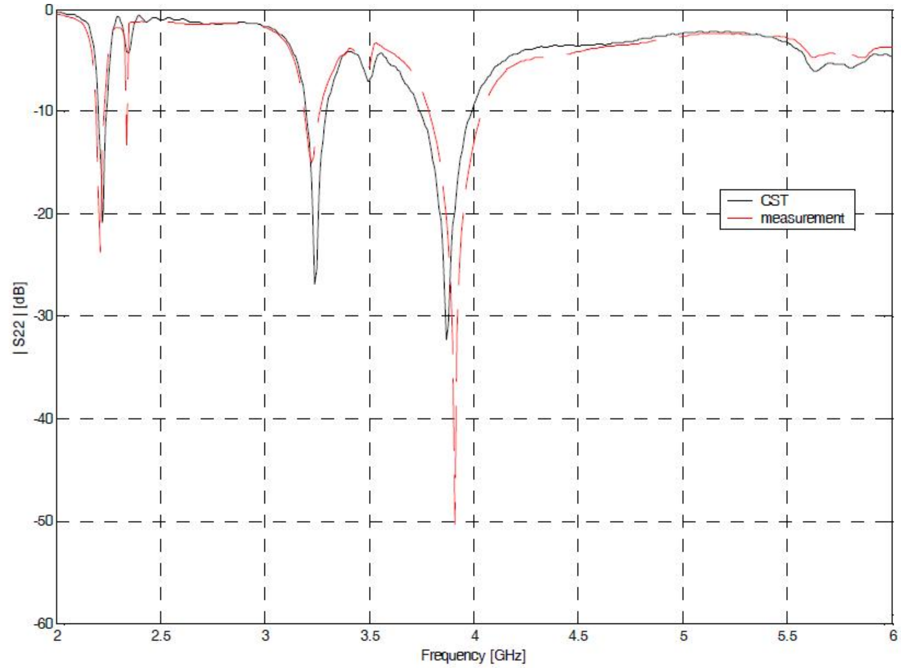

Figure 3.12: *Comparison between the measured and CST results for* S_{22} *[54].*

data compared to the FEKO result.

The variation in S_{11} magnitude rarely exceeds 3 dB. A similar offset from the resonant frequency of the dish monopole is seen as with FEKO, indicating the same 1 mm difference in length.

For the S_{21} results, the CST plot follows the measurement closely, except for one deep resonance at 5.1 GHz. As this feature is a consequence of coupling, the physical cause is not immediately clear. In the case of reflections for any given port, path length resonances are easier to determine. Apart from this resonance, the results agree to within 5 dB, similar to the FEKO results.

No more than 1 dB separates the CST and measured results in Fig. 3.12, testifying to the accuracy of the code. The minor offset of the resonant frequencies indicates a small dimensional error (less than 1 mm) on the computational model. This confirms the importance of accurate geometrical dimensions in the computational model.

3.4 Conclusions

The main objective for the work relayed in this chapter, which is the verification of the FEKO model, is successfully obtained. Rigorous S-parameter measurements in an anechoic chamber, in conjunction with the CST code results, show that the computational modelling in FEKO is convincingly validated and that the code can be trusted. However, the code is extremely dependent on the correct dimensional input and description of the geometry. With stray current found on the measurement cables, EM barriers will further add to the rigour of future model measurements.

– In theory, there is no difference between theory and practice. But, in practice, there is. –

– Jan L.A. van de Snepscheut –

Chapter 4

Real Earth in Scale Model

This chapter describes the following design of KAT, the experimental demonstrator model or XDM. In addition to incorporating the experience from the earlier modelling, equivalent soil conditions are introduced. The model, with and without the simulated soil, is verified by measurement and comparison to CST. Measurements are also done on the actual XDM as built at South Africa's main radio astronomy centre, the Hartebeeshoek Radio Astronomy Observatory (HartRAO). Fig. 4.1 shows the XDM that we tested for lightning and EMC.

4.1 Introduction

The design for XDM utilised steel reinforced concrete for the structure and foundation, and a lightweight composite material for the dish. The dish reflective layer was formed by an aluminium flash-spraying technique, resulting in an approximately 50 μm-thick coating. Scale modelling and verification was done during construction, while full-scale measurements were done after the structure was completed.

4.2 XDM Design $1/40^{th}$ Scale Model

Learning from previous modelling experience, the dish was not included in the XDM scale model design to eliminate earlier problems (see section 3.2.2). The focus for this model was shifted to the foundation, pedestal structure, and cable conduits. The simplified scale model includes the reinforcing within the concrete of the XDM pedestal structure, as well as in the foundation. According to international standards [9], this reinforcing can also be used as part of the lightning protection system.

Figure 4.1: *Photograph of the XDM as constructed at HartRAO.*

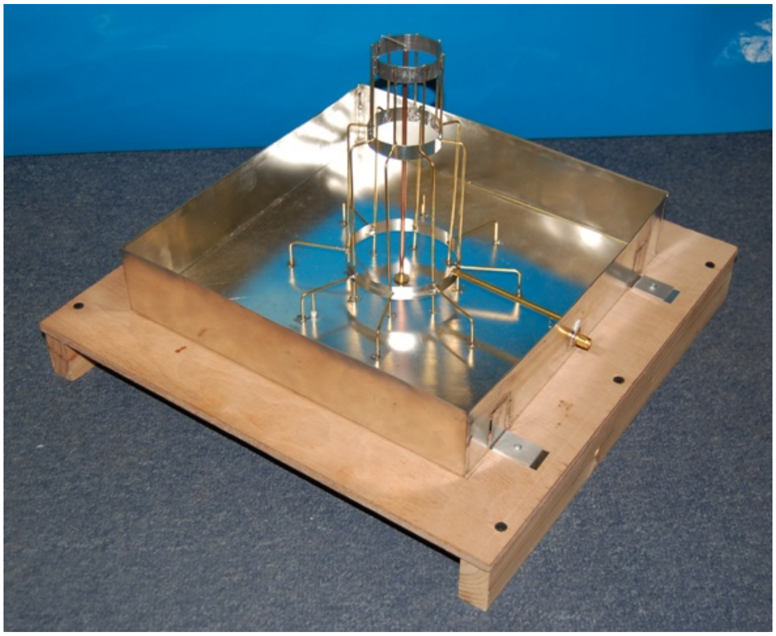

Figure 4.2: *Photograph of the XDM design scale model.*

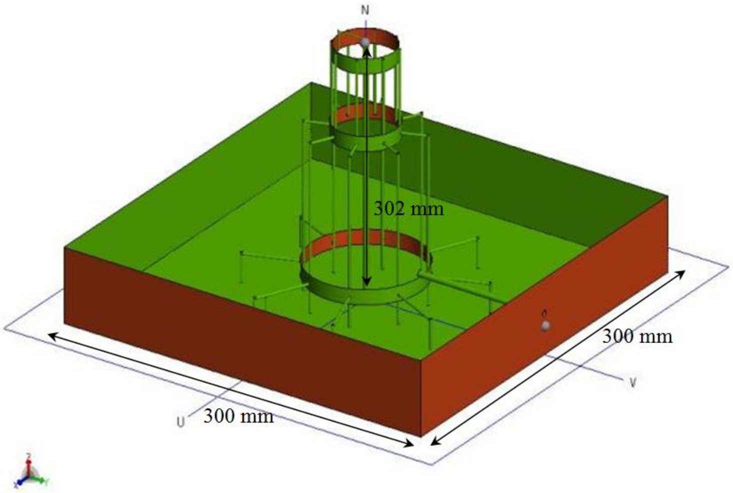

Figure 4.3: *XDM design FEKO scale model. The excitation port can be seen at the top, and the measurement ports are placed one on the right hand side, and one on the bottom ground plate. The basic dimensions are shown on the figure.*

4.2.1 Physical Scale Model

The simplified scale model following the XDM design can be seen in Fig. 4.2. The pedestal concrete steel reinforcing was represented by eight brass rods, and ring bonding bars by three thin metal plates, all interconnected. Eight radially connected horizontal brass rods mimic the steel reinforcing in the foundation. These rods then connect the pedestal structure to a ground plate. A brass pipe, which connects to the bottom ring bonding bar, depicts a cable conduit running from the pedestal.

Three ports are placed on the structure for S-parameter measurements similar to the previous model. The excitation port, which can simulate a direct lightning strike, is formed by a semi-rigid cable which enters via an SMA bulkhead connector through the ground plate at the bottom and extends to the top of the model. Here the core wire was stripped from the dielectric and sheath, and terminated onto the top ring.

The pick-up ports are formed by loops at two locations. One of the ports is placed on the end of the pipe representing the cable conduit, connecting to the side plate of the model. It uses an SMA bulkhead connector core wire to connect in an L-shape to the pipe. The SMA connector is soldered to the side plate to ensure a good connection to ground. Another port is placed at one of foundation reinforcement brass rods. Here the SMA connector is placed below the ground plate and the core wire forms a pick-up loop when connected to the foundation rod.

To prevent stray currents flowing from the ground plate onto the measurement cable sheaths, the side plate forms an EM barrier at the conduit port on the side of the model. This was achieved by bending 65 mm of the ground plate up by 90 degrees. The process

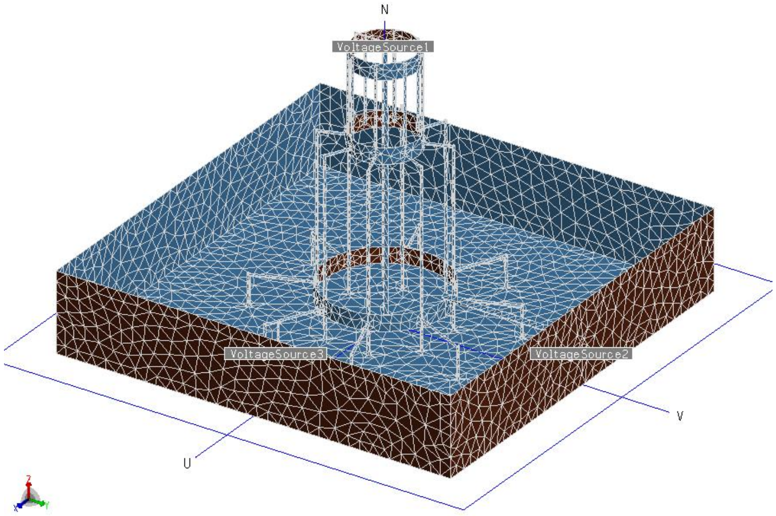

Figure 4.4: *Discretisation mesh of the XDM design FEKO model.*

was extended to all four sides of the plate to facilitate a watertight enclosure, which enables the inclusion of a salt solution to represent the Karoo soil properties.

4.2.2 Scale Model in FEKO

The dimensions of the scale model following the XDM design were accurately measured and the model reconstructed in FEKO. The excitation port was defined at the point where the core wire of the semi-rigid cable is stripped from the dielectric. This eliminates the need for the use of dielectric in the model. All three ports were again defined by 50 Ω discrete voltage ports. S-parameters are calculated in FEKO similar to the VNA measurement. The XDM design scale model in FEKO is shown in Fig. 4.3. The discretisation edge length for meshing was chosen the same as with the previous model, but a larger local mesh size was defined for the ground plate and sides. Subsequently a mesh was formed with 15,080 triangles and 3 segments in free space. The meshed structure can be seen in figure 4.4. The frequency range for investigation was chosen between 1 GHz and 6 GHz for the computation. The total time taken for FEKO to calculate the S-parameters at 51 discrete frequency points, on a four-core machine with 15 GB memory, was forty and a half hours.

4.2.3 Verification by Measurement

Similar to the procedure used in section 3.2.3, the S-parameters were measured using a two-port VNA connected to the model via two phase stable cables leading into an anechoic chamber. Different from the previous model, however, a third port was present in a two-port measurement. To prevent unwanted reflections from this port being left open, a

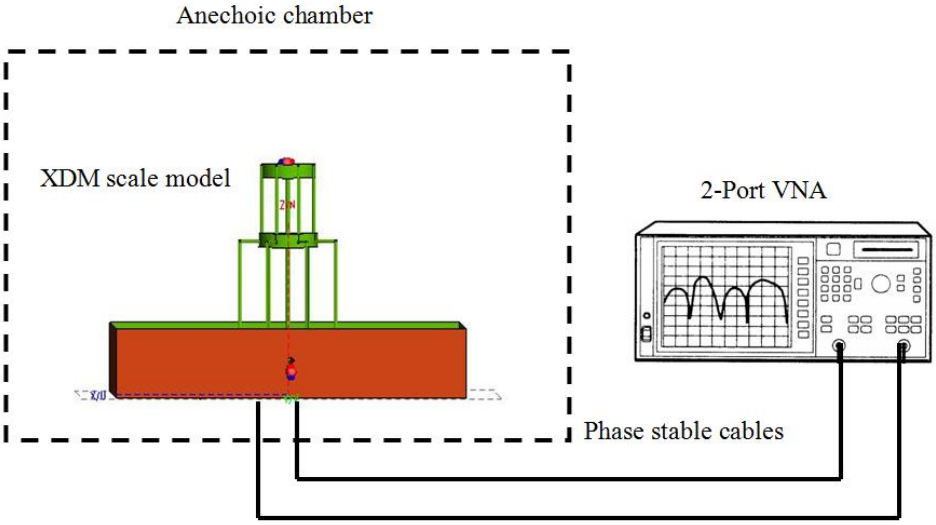

Figure 4.5: *Diagram of the measurement setup for the XDM scale model.*

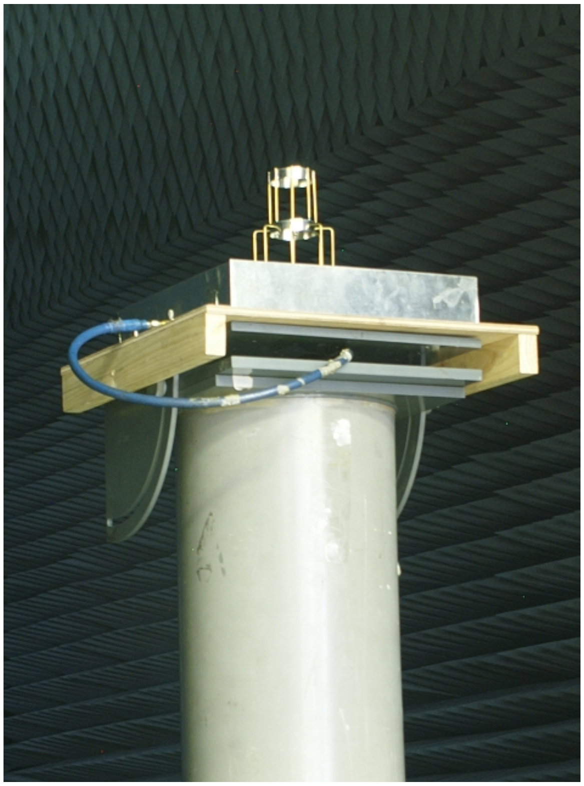

Figure 4.6: *Photograph of the XDM scale model as measured in the anechoic chamber.*

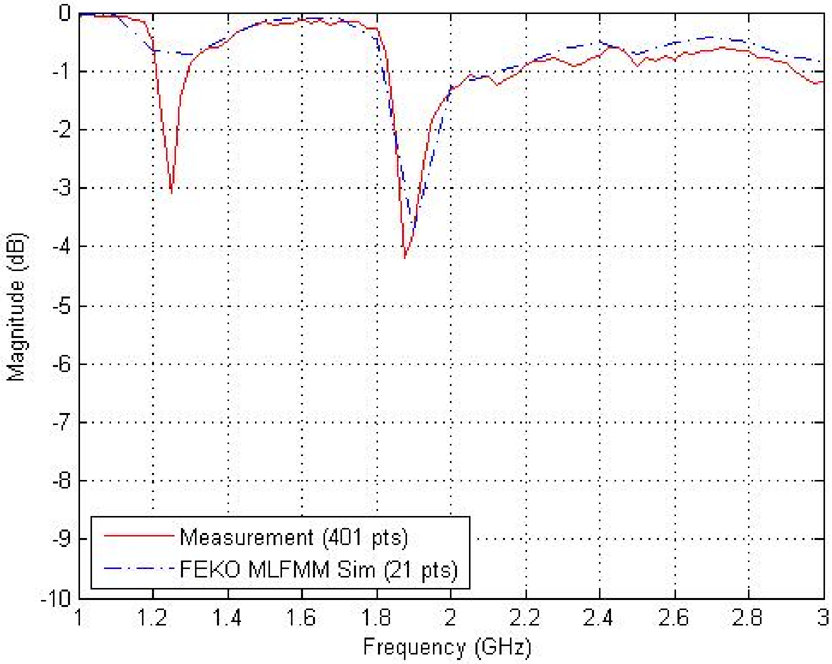

Figure 4.7: *S_{11} Magnitude comparison between FEKO and measured results for the excitation port of the XDM model without simulated soil.*

50 Ω load was connected to it when measurements were made. A diagram showing the measurement setup of the XDM scale model in the anechoic chamber can be seen in figure 4.5.

4.2.4 Evaluation with CST

The physical model geometry was replicated in CST. All three ports were represented by discrete voltage ports with 50 Ω impedance. Model boundaries were set to open for all sides except the ground plane, which was set to electric boundary. With the 4 mm diameter brass rods used for the model, the FVTD discretisation had to be small enough to ensure that all the elements in the model were represented in the mesh. Due to a lot of empty space in the total model volume, this led to a very large mesh being computationally expensive. However, a function in CST allows mesh adaptation for these situations, and after running the feature, the refined mesh was reduced to approximately 300,000 mesh cells. The frequency range was, however, limited to up to 3 GHz by the mesh size, to ensure accurate results. The transient solver was used for the calculations and the results Fourier transformed by CST to S-parameter results. The simulation was run on a dual-core machine and took just over six hours.

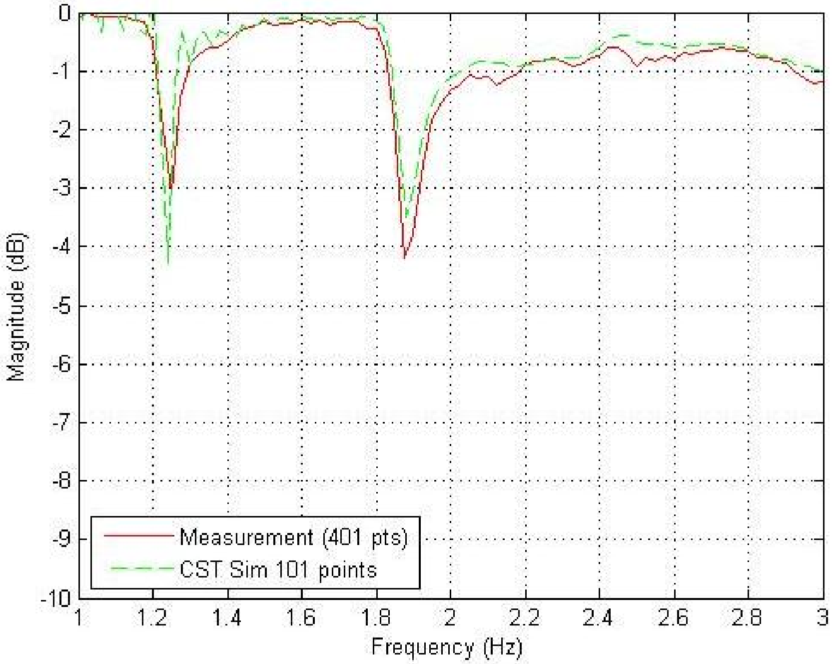

Figure 4.8: *S_{11} Magnitude comparison between CST and measured results for the excitation port of the XDM model without simulated soil.*

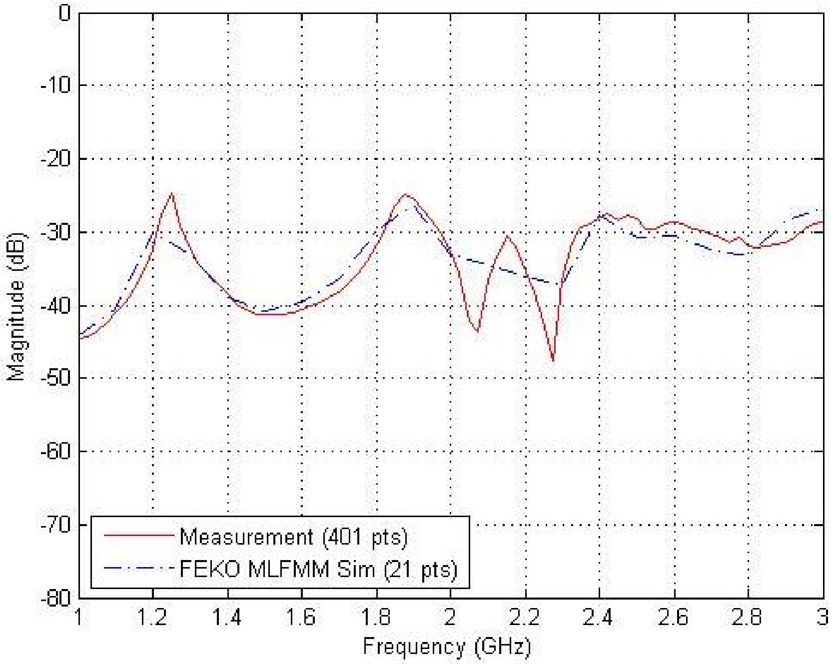

Figure 4.9: *S_{21} Magnitude comparison between FEKO and measured results for the bottom port of the XDM model without simulated soil.*

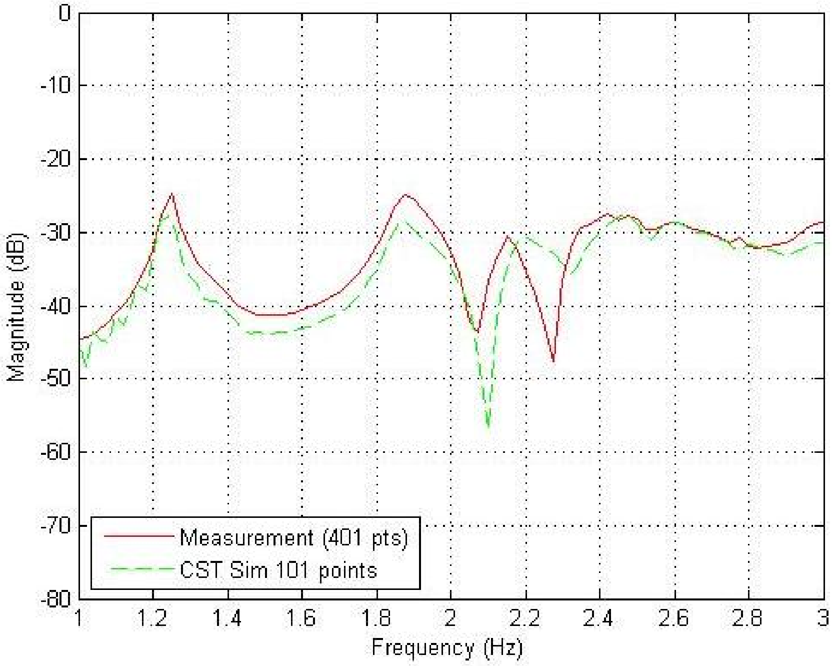

Figure 4.10: *S_{21} Magnitude comparison between CST and measured results for the bottom port of the XDM model without simulated soil.*

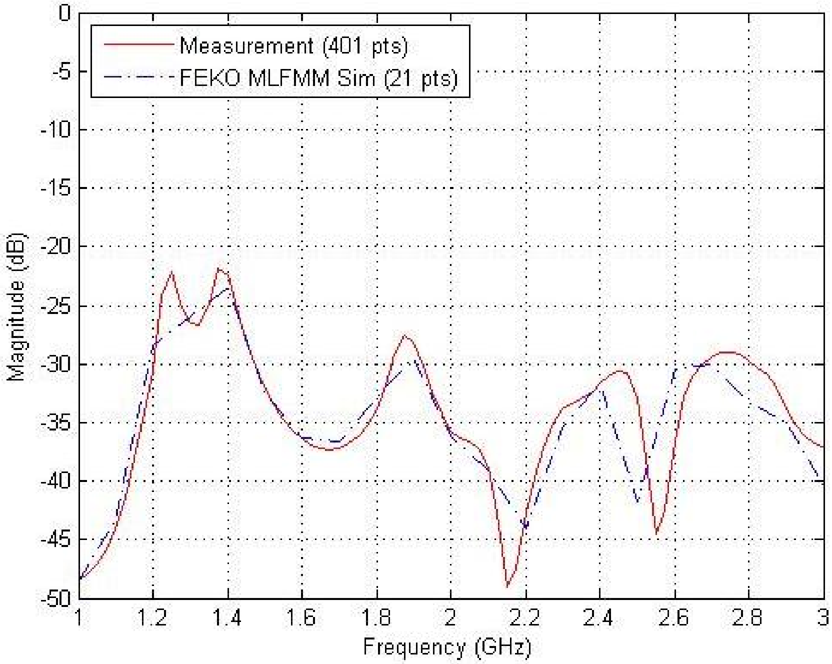

Figure 4.11: *S_{21} Magnitude comparison between FEKO and measured results for the side port of the XDM design model without simulated soil.*

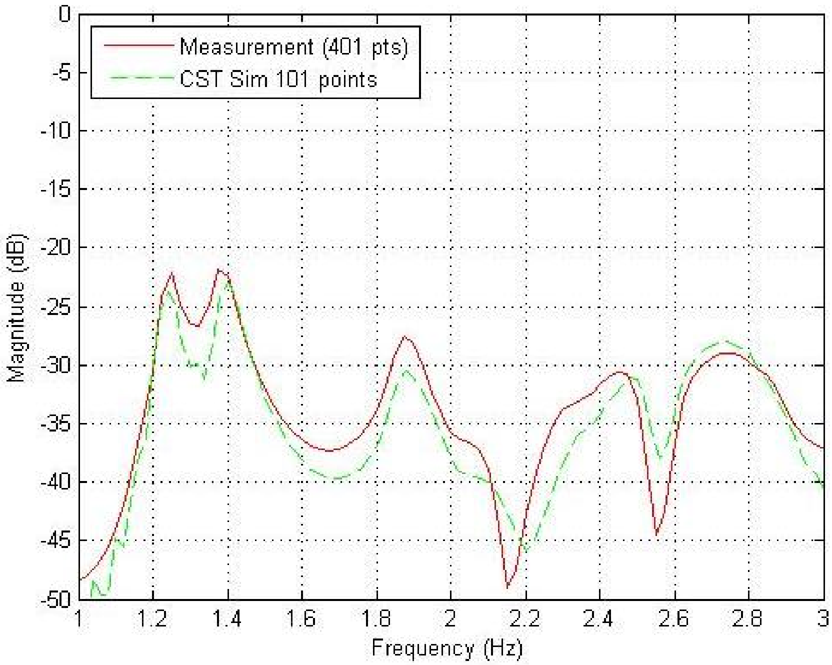

Figure 4.12: S_{21} *Magnitude comparison between CST and measured results for the side port of the XDM model without simulated soil.*

4.2.5 S-parameter Magnitude Results

Fig. 4.7 and Fig. 4.8 show the S_{11} magnitude comparison between FEKO and measured results, and the CST and measured results respectively, for the excitation port at the top of the XDM model. Excellent agreement to within 0.3 dB is shown for both CST and FEKO results compared to the measurement. The first sharp resonance is missed by FEKO due to the limited amount of frequency points calculated.

The S_{21} magnitude comparison between FEKO and measured results can be seen in Fig. 4.9 and the CST and measured results are shown in Fig. 4.10. Both figure's results are for the XDM bottom port simulations and measurement. The FEKO result variation from the measured result stays within 2 dB, except at the resonances. Here, some of the resonances are missed due to only 21 frequency points being calculated in the whole frequency range. For the CST results, the plot differs from the measurement by no more than 3 dB, but it follows the resonances closely, seeing that a total of 401 frequency points were Fourier transformed.

The same comparison for the side port FEKO and CST results are shown in Fig. 4.11 and Fig. 4.12. For both codes the measured and computed values stay within a 3 dB limit from each other.

Considering the correlation between the measurement and the two codes, the verification of the computational code can be deemed a success.

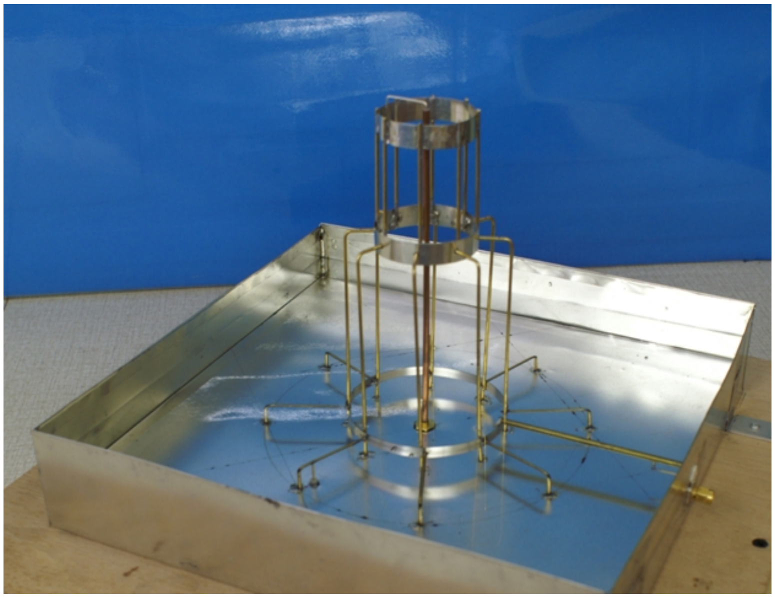

Figure 4.13: *XDM design scale model, filled with a salt solution to simulate Karoo soil.*

4.3 XDM Scale Model with Simulated Karoo Soil

The verified models are used to investigate the influence of the Karoo soil. The soil is simulated using a scaled conductivity salt water mix. With the Karoo soil resistivity of 200 Ω-meter and a scaling factor of 40, the conductivity of the salt solution needed to be $40 * 1/200 = 0.2\ S/m$. This was achieved by adding normal sodium chloride to distilled water at room temperature until the required conductivity was measured. The measurement was done using a calibrated conductivity probe.

4.3.1 Measurement of Model with Simulated Soil

The salt solution is added to the model and measurements are made in the anechoic chamber with the VNA, using the same measurement setup and procedure as in section 4.2.3.

4.3.2 Simulated Soil in FEKO

An initial attempt to model the enclosed salt solution in FEKO used a hybrid MoM / finite element method (FEM) solution (see Fig. 4.14). The salt solution has a 36 mm depth and size inside the enclosure of 300 mm x 300 mm. This volume has to be meshed with tetrahedra. To further complicate the modelling, the relative permittivity of the salt solution has to be taken into consideration for the mesh size. The assumed value of 80 for the relative permittivity of salt-water, implies a wavelength of $1/9^{th}$ times the wavelength in free space. For accurate solution to the FEM code at 1 GHz, the proposed side length of a dielectric tetrahedron mesh cell had to be between 3 mm and 6 mm. With 5 mm

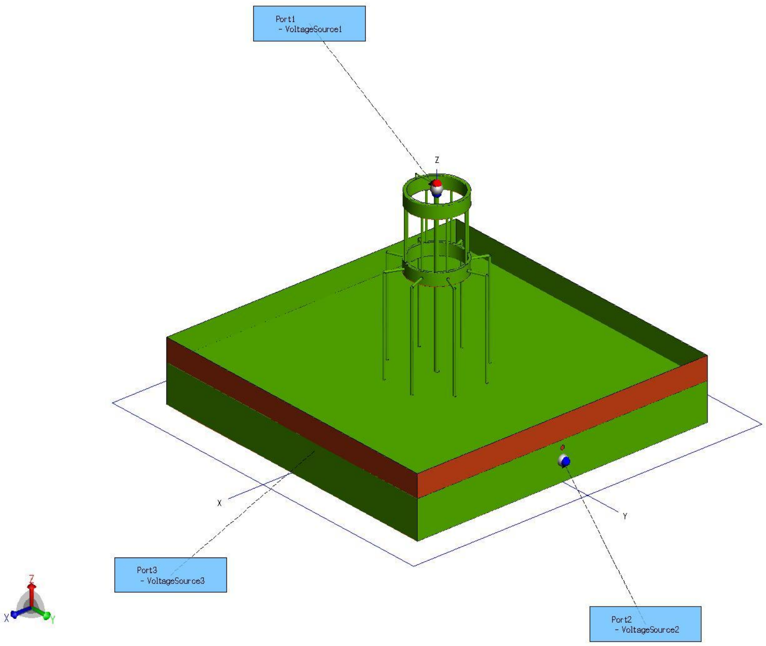

Figure 4.14: *XDM design FEKO scale model with a salt solution included as dielectric, using a MoM / FEM hybrid solution.*

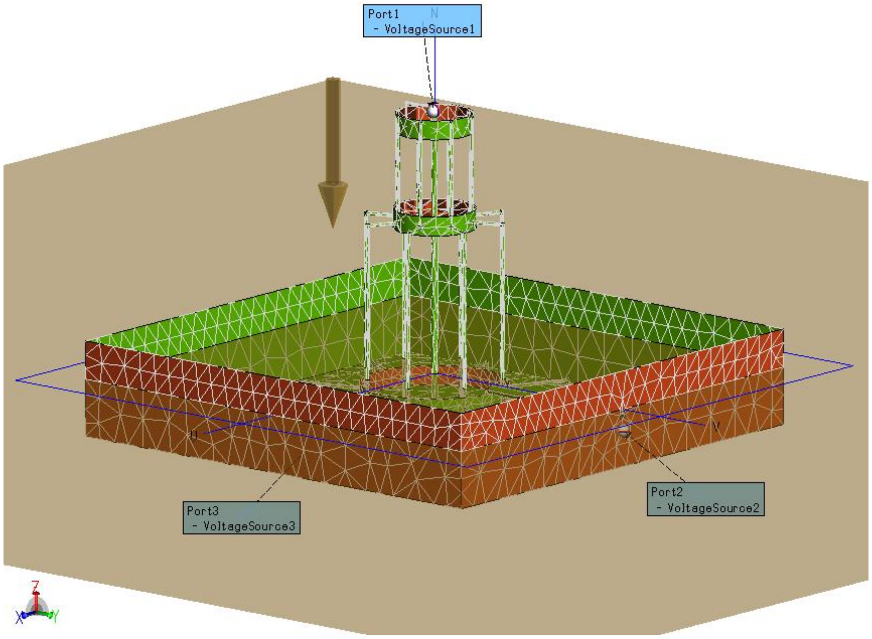

Figure 4.15: *XDM design FEKO scale model with unrefined mesh and Sommerfeld ground plane.*

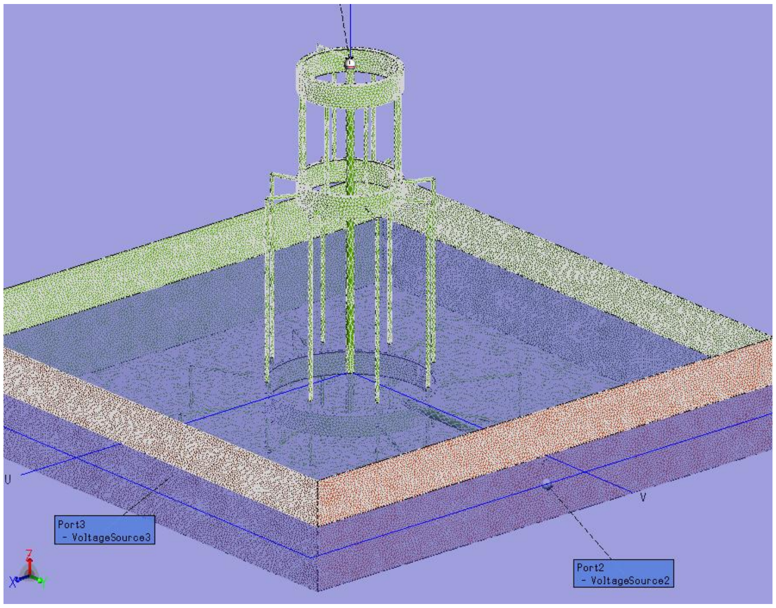

Figure 4.16: *XDM design FEKO scale model with refined mesh and Sommerfeld ground plane.*

edge length, the mesh involved 6,356 metallic triangles and 425,567 tetrahedral elements. This required 42 GB of memory, which was not available at that stage of the project.

The alternative method to include the salt-water, which requires less memory, is the FEKO infinite ground plane with a Sommerfeld integral solution. However, using the infinite plane, it follows that the model is "immersed" in salt-water (shown in Fig. 4.15), instead of salt-water being enclosed inside the model EM barriers. An initial meshed system consisted of 3 wire-segments and 20,000 triangles, requiring only 6.8 GB of memory. A successful simulation was run on a four-core machine with 15 GB memory, taking almost eighteen hours for one frequency point to solve. With 13 mm edge length for this simulation, however, the meshing was still very coarse.

Consequently the Centre for High Performance Computing (CHPC) became available for use by students and staff at Stellenbosch University. This facility consists of 160 nodes, each with 2 dual-core processors and 16 GB of memory. The meshing in FEKO was refined to an edge length of 2 mm, resulting in 3 segments and 155,238 triangles to solve (Fig. 4.16). This required a total of 402 GB of memory. A sum of 32 nodes were used on the CHPC, which initially took four days to compute one frequency point, but after updating the networking software, was improved to just under twenty-four hours per frequency point. In total, seven frequency points were calculated for the FEKO model.

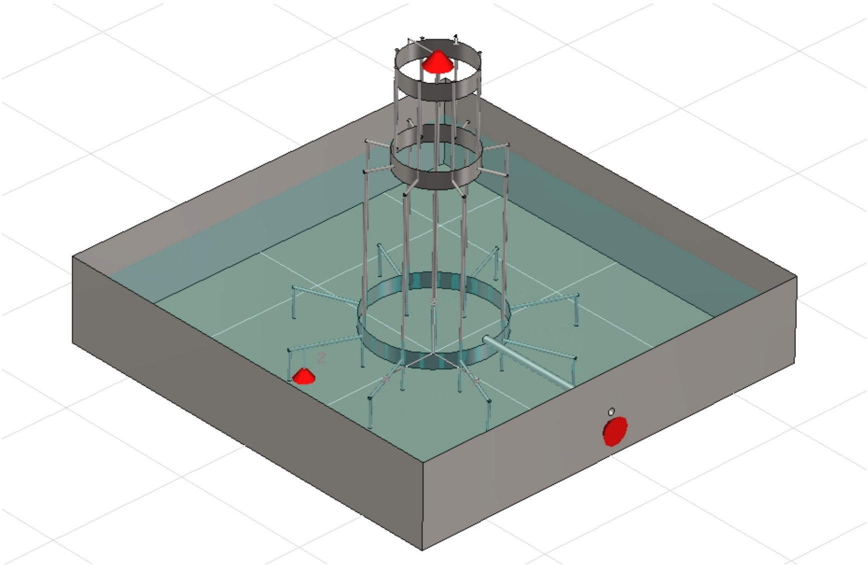

Figure 4.17: *XDM design CST scale model with salt-water dielectric.*

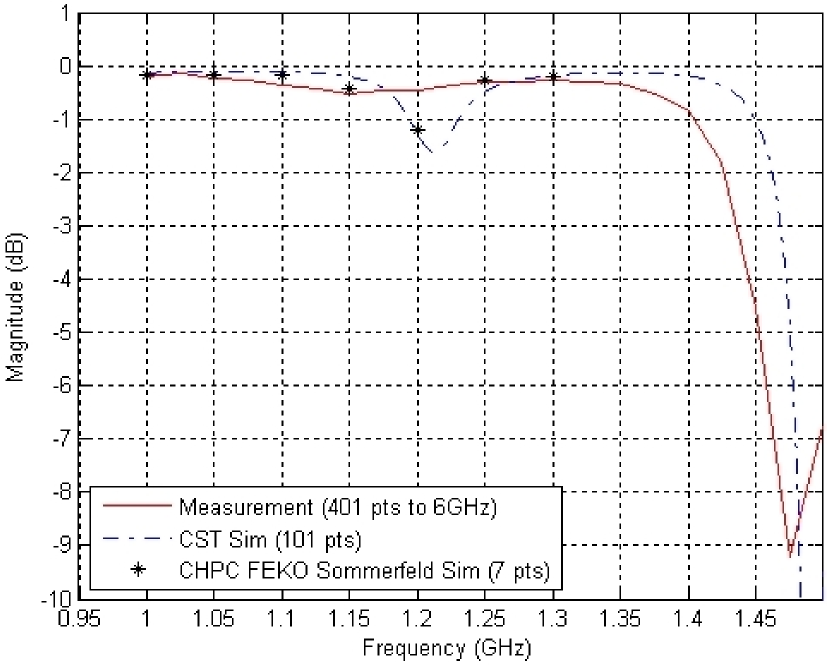

Figure 4.18: S_{11} *Magnitude comparison between FEKO, CST and measured results for the top port of the XDM design model with simulated soil.*

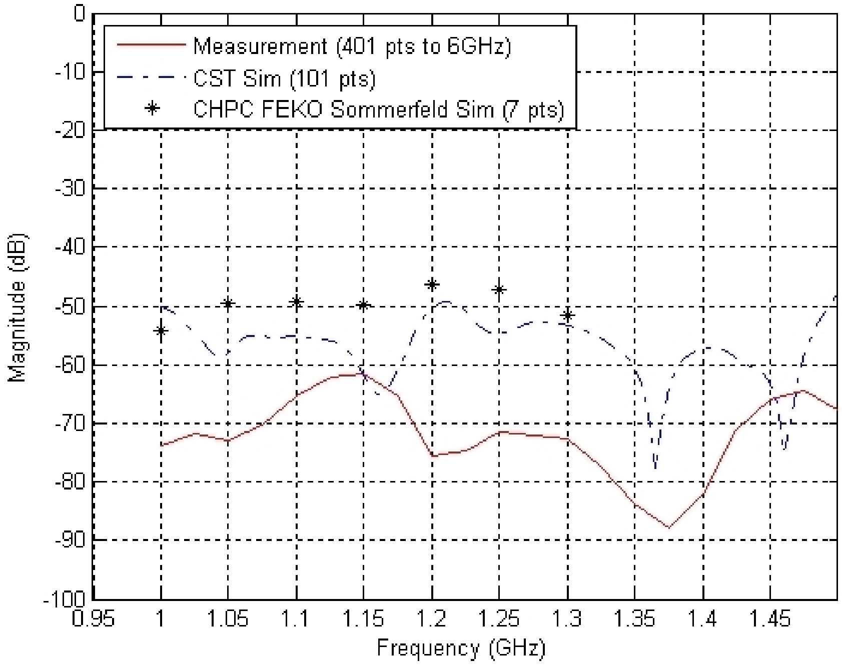

Figure 4.19: S_{21} *Magnitude comparison between FEKO, CST and measured results for the side port of the XDM design model with simulated soil.*

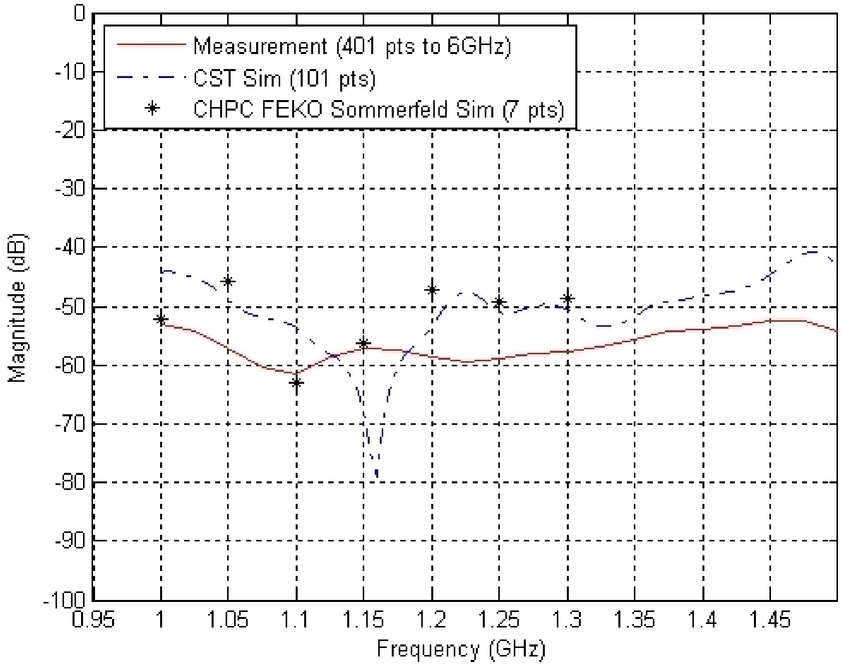

Figure 4.20: S_{21} *Magnitude comparison between FEKO, CST and measured results for the bottom port of the XDM design model with simulated soil.*

4.3.3 Simulated Soil in CST

The second verification again involved CST. The verified CST model without salt-water dielectric was utilised. When the dielectric was added to the model however (Fig. 4.17), meshing had to be refined extensively to accommodate the dielectric material with assumed relative permittivity of 80. The amount of mesh cells was limited to 1,000,000 by the available license, and the required fine mesh could not be achieved. Successful simulations were only done for a frequency range between 1 GHz and 1.5 GHz, with a mesh containing 750,000 mesh cells. This simulation took approximately seventeen hours on a dual-core machine. However, due to the license limitation, the meshing could not be further refined for accuracy.

4.3.4 Comparison of Results

The unrefined CST results, as well as the FEKO Sommerfeld results, compared to measurement, are shown in Fig. 4.18 to Fig. 4.20. In the S_{11} results of Fig. 4.18, both codes conform to the measurement to within 0.2 dB, except for a resonance that is detected in the computations at 1.2 GHz, which is not reflected in the measurement.

For the S_{21} results of the side port in Fig. 4.19, the variation between measurement and the simulations is between 10 dB and 23 dB, and resonant frequencies do not align. A difference of 1 dB to 11 dB between measured and computed values of Fig. 4.20, show better agreement for the S_{21} results. For both S_{21} results, the computational code values are closer to each other than they are to the measurement.

The deviation of specifically the resonances in the plots, indicates that wavelengths in the dielectric material are not the same for the physical and the numerical model. The accuracy for the assumed relative permittivity value of 80 is thus brought into question. This point was raised at an SKA conference by a FEKO software developer. As a result of this discussion, the literature was reviewed and [55] was obtained, accurately defining the permittivity of seawater in the frequency range of 1 Hz to 256 GHz. Between 1 GHz and 2 GHz for example, the real part of the relative permittivity is given as 71, due to inertial properties of molecule orientation polarization. The total polarization of seawater is the polarization due to the displacement of ions inside water (i.e. atomic polarization) added to the displacement of bound charges in water molecules (i.e. induced and orientation polarization).

The modelling in FEKO and CST take both the dielectric properties and conductivity into account with the simplified definition of the complex relative permittivity as shown in equations 4.1 and 4.3. Thus the use of salt water for modelling above 1 GHz can be justified using this definition in the computational codes. Ideally, more accurate estimates of soil properties could be obtained from drilled core samples from the Karoo. However, project timelines did not allow this, and we had to assume a constant conductivity from initial estimates obtained by the project team.

From [55], the complex permittivity of seawater with different salinity and temperature was accurately modelled. This was compared to previous measurements, as well as extrapolated, fitted results at frequencies from 1 Hz to 256 GHz. The equations show a more detailed expression for the complex relative permittivity, but they also show the simplified form as described in the computational codes. From [55]'s resulting values of permittivity of seawater, the variations between the computed and measured results can be understood.

When the resonant frequency wavelengths are adjusted according to the error ratio of 71:80, it is seen that the resonances around 1.2 GHz and 1.37 GHz move into alignment. This confirms that the relative permittivity value of seawater at 71 is closer to the actual measured permittivity.

If the sharpness of the resonances are considered, it shows that the imaginary part of the permittivity is incorrect as well. The value that the simulations use, is defined by the conductivity and the frequency in the following way:

$$\epsilon_{eff} = \epsilon_0 \epsilon_r - j\frac{\sigma}{\omega} \tag{4.1}$$

where ϵ_{eff} is the effective permittivity, ϵ_0 is the permittivity of free space, ϵ_r is the relative permittivity, σ is the conductivity and ω is the radial frequency. If the effective permittivity can be expressed as follows:

$$\epsilon_{eff} = \epsilon_0 \epsilon_r - j\epsilon_0 \frac{\sigma}{\epsilon_0 \omega} = \epsilon_0(\epsilon' - j\epsilon'') \tag{4.2}$$

then the complex relative permittivity can be seen as:

$$\epsilon_{rcomplex} = \epsilon_r - j\frac{\sigma}{\epsilon_0 \omega} = \epsilon' - j\epsilon'' \tag{4.3}$$

When the conductivity value of 0.2 from the simulations is used to calculate ϵ'' at 1 GHz in equation 4.3, a value of 3.6 is obtained. However, the value of sea water as given by [55] is 70. This indicates higher losses in the actual sea water, explaining the sharper resonances in CST compared to the measurement of the salt solution.

Taking into account that the unrefined CST mesh and the FEKO infinite plane were not entirely accurate representations of the model, and that the relative permittivity was not correctly defined, the results from this investigation are deemed satisfactory.

4.4 Full-scale Measurements at HartRAO

An RFI audit at the XDM site revealed a number of pick-up loops and current paths that would be important if very low RFI immunity were sought. These loops and paths

Figure 4.21: *Continuous wave current injection using a signal generator connected to the LDC of the XDM.*

were identified through a number of measurements of which only one is highlighted in this section. These measurements identified that a direct current strike would still damage the systems contained within the pedestal. However, the risk of such a strike is low (the XDM is surrounded by high hills) and it was agreed that no immediate mitigation measures were required. A number of background emissions was noted which could be reduced in pick-up level by modifications to the cabling layout [56].

To consider lightning RFI, the standard method would be to use an EMP simulator. However, the observatory is a radio quiet zone, and alternative methods had to be utilised. A signal generator (SG) inside a cherry-picker crane is used to generate a 10 MHz and 50 MHz continuous wave (CW) signal onto different LDC elements of the XDM, of which one is shown in Fig. 4.21. The SG is powered from the 220 V mains outlet inside the structure using a 15 m lead. Only the positive terminal of the signal generator is connected onto the LDC, while the ground of the signal generator is connected to the earthing bonding bar inside the structure via the lead and mains. This creates an excitation loop of RFI, which couples to earth loops inside and on the structure.

Using a battery-operated hand-held spectrum analyser and a common mode (CM) current probe, the levels of coupling were measured at various test points. Fig. 4.22 shows one of the pick-up loops, formed by the cabinet power cable sheath leading to a power filter on top of the shielded cabinet, and power and communication cable sheaths, all of which connects to the cabinet and to the earth bonding bar.

From the measured levels, it was presumed that with such a large pick-up area formed,

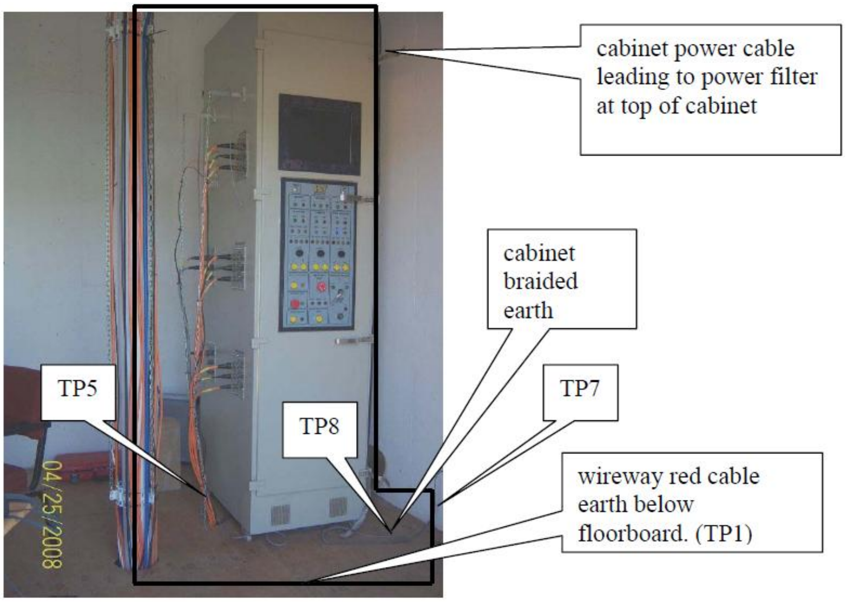

Figure 4.22: *Pick-up loops inside the XDM structure formed by cable sheaths and earthing layout [56]. Test points are indicated by the letters TP and a number.*

currents can easily be induced on the cable sheaths through magnetic coupling. However, when this research was communicated at the 2008 URSI conference [10], the question arose as to the validity of the excitation. Using the mains power earthing, forces the currents to flow through the earthing cables and connections of the structure. Thus the coupling could be resistive instead of magnetic. When planning the final model of the research, this issue was included for investigation.

The screening effectiveness of the cabinet was tested using the current probe and spectrum analyser inside and outside the cabinet. When placed on the inside, the spectrum analyser was set to record maximum levels. The cabinet shielding was measured between 30 and 35 dB within the 100 kHz to 10 MHz band [56]. This indicated that the sensitive equipment inside was sufficiently shielded against induced currents on the cable sheaths.

4.5 Conclusions

With valuable experience gained on the initial scale model, the XDM scale model was carefully planned, constructed and successfully verified using measurement and CST code.

To simulate the Karoo soil conditions, a salt solution with scaled conductivity is added to the physical model and represented in the computational models in FEKO and CST. However, some limitations hamper the full utilisation of both codes. The unrefined CST mesh and the infinite FEKO plane are not entirely accurate representations of the model. The relative permittivity value for the salt solution was also found inaccurate for the high frequencies considered. However, in view of these factors, the results from this investigation are deemed satisfactory and the goal of including soil in the model is successfully obtained.

Measurements on the XDM installed at HartRAO yielded valuable insight into pick-up loops and current paths from external RFI. From analysis of the measurements, the good cabinet shielding and the low risk of a lightning strike was deemed sufficient not to warrant additional lightning protection and bonding measures. However, the validity of our method for lightning excitation by current injection was questioned. The issue is further discussed in the next chapter.

– The key to success is not through achievement, but through enthusiasm –

– Malcolm Forbes –

Chapter 5

Accurate Scale Model of KAT-7

With confidence in our computational code and measurement verification strategies, we designed an accurate scale model of the KAT-7 structure with assistance from the SA SKA mechanical engineer. This chapter gives detail on the construction and two measurement verifications of the model.

5.1 Introduction

The final design for the KAT-7 stage of the project was named the advanced development model or ADM. Fig. 5.1 shows the engineering design of this structure.

Taking earlier recommendations and manufacturing criteria into consideration, the design team made several material and layout changes to the design. Steel replaces the steel reinforced concrete as the structure material for the ADM. The layout and mechanisms for the elevation of the dish were changed, using a set screw system instead of a geared system. For the dish, the light-weight composite material is still used, but the reflective layer is created using a conductive mesh embedded in the dish, instead of the flash-sprayed aluminium. The design layout for the counterweights was changed as well.

For this research project, a very accurate scale model of this design was required. The scale model had to be constructed in such a way as to easily do verification measurements, and be true to the actual design in order to study lightning and RFI in our computational model with confidence. For this purpose, we approached the mechanical designer of the ADM.

5.2 KAT-7 Design $1/20^{th}$ Scale Model

After discussion with the SA SKA mechanical engineer who designed the ADM, he agreed to help in producing an accurate detailed scale model following a simplified version of the KAT-7 design.

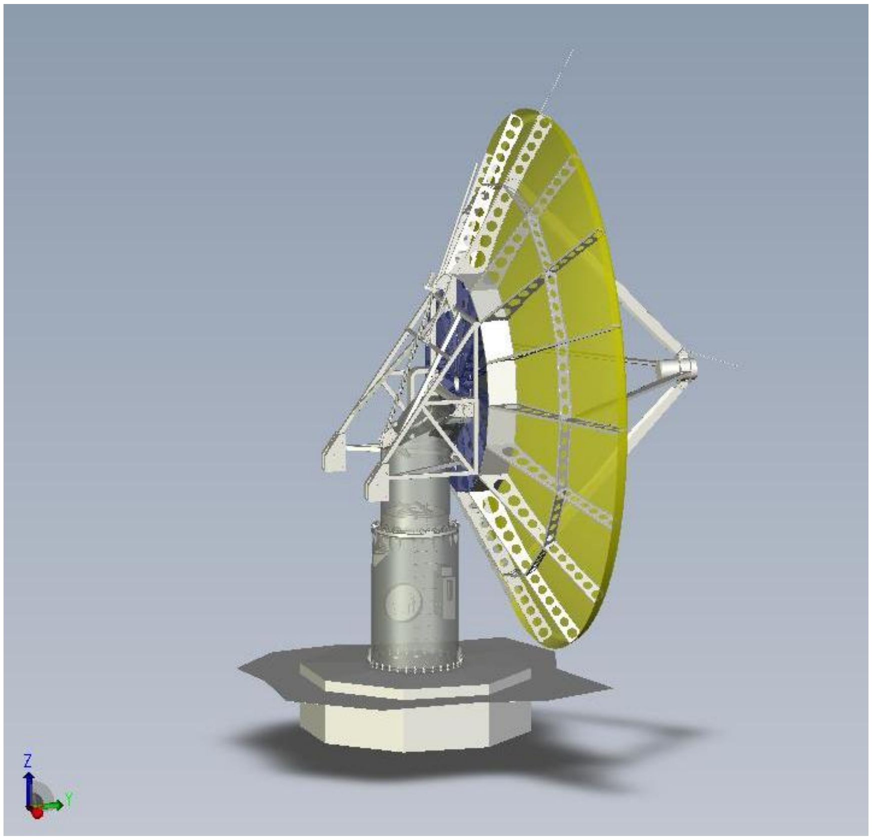

Figure 5.1: *Near-final engineering design of the KAT-7 structure.*

With all the relevant requirements met, the designer produced the $1/20^{th}$ scale model design shown in Fig. 5.2. All elements of the model were separately drawn to enable precision engineering of each.

The design drawings were sent to an engineering company who used laser-cutting to produce all the parts of the model. These were sent for tin-plating to prevent corrosion and ensure good galvanic connection when constructed. The assembly was done in-house by the Stellenbosch University Electrical and Electronic Engineering electronician.

5.2.1 Physical Scale Model

The model was mounted on a large, flat ground plane plate. The injection port was created with a semi-rigid cable coming through the ground plane via an SMA bulkhead connector and terminating with only its core wire onto the focal point of the dish. A pick-up loop was placed at the base of the pedestal by extending the core wire of an SMA bulkhead connector onto the pedestal wall. The physical model as measured for S-parameters in the anechoic chamber is shown in Fig. 5.3.

One of the simplifications done on the dish to ease manufacturing, was to change the dish design from parabolic to cone-shaped. The cone could then be produced out of a

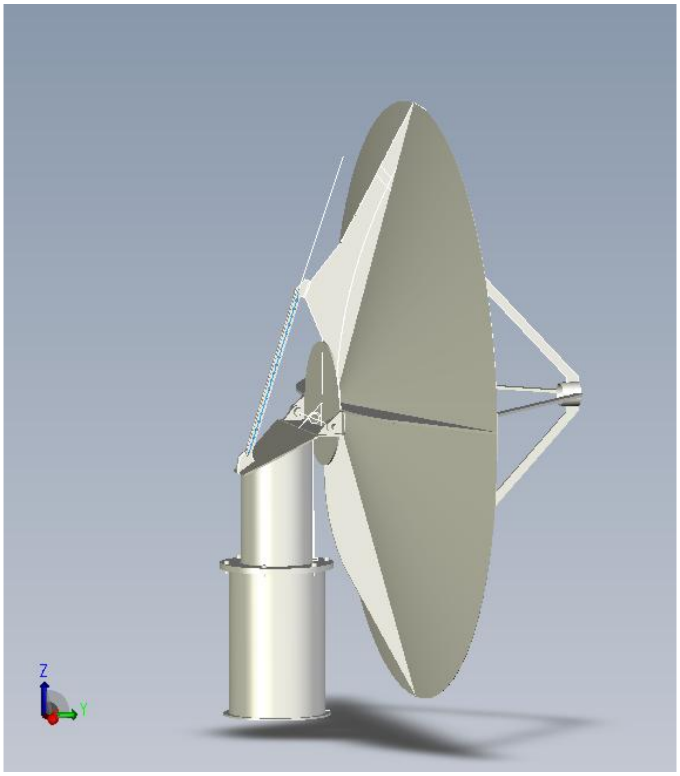

Figure 5.2: *Engineering drawing of the simplified scale model following the KAT-7 structure design.*

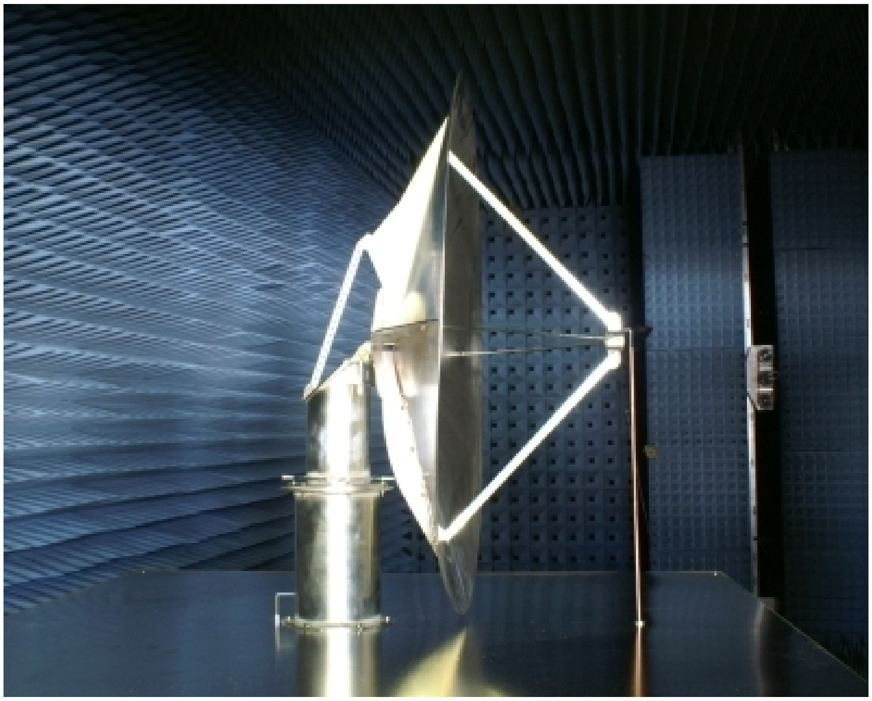

Figure 5.3: *Photograph of the KAT-7 design scale model, as set up in the anechoic chamber for S-parameter measurement verification.*

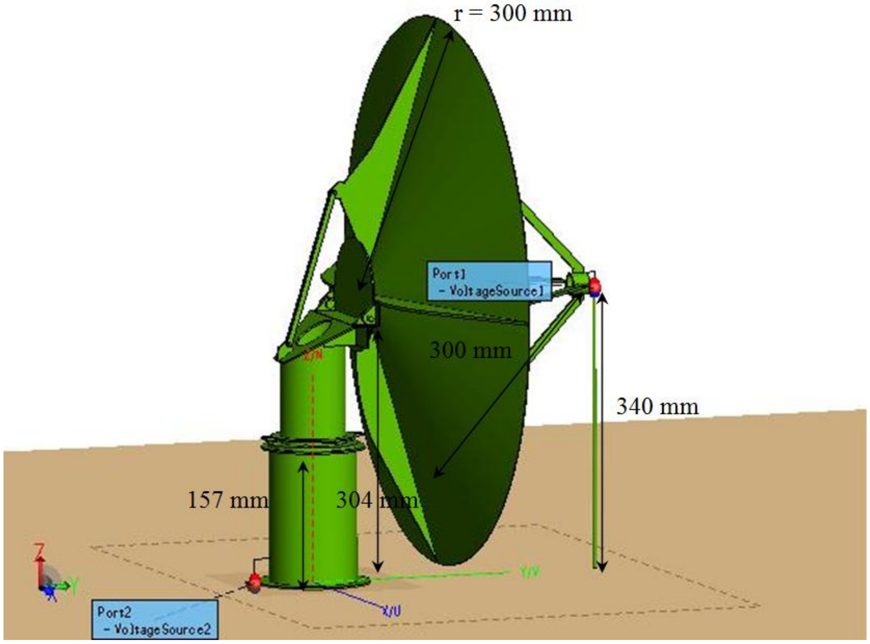

Figure 5.4: *KAT-7 design FEKO scale model with simulated lightning injection on the dish focal point as the excitation port. A pick-up port is formed by a loop connected to the bottom of the pedestal. Basic dimensions are shown in the picture.*

single piece of flat plate, pop-riveted at the edges. The counterweights were removed as well to simplify the design.

The two elements of the pedestal were designed such that it could replicate the movement of the azimuth bearing of the ADM. Similarly, the elevation bearing movement was enabled by two screws connecting the bearing to the pedestal, and two adjustable plates representing the set screw. The dish could thus be fixed at any angle between 0 degrees and 90 degrees from the vertical.

With the current injection semi-rigid removed, this enables plane wave measurements with the dish in any position and orientation.

5.2.2 Scale Model in FEKO

Exact dimensions were available in the design file for the KAT-7 scale model. Although the model could not be successfully imported in FEKO, the correct dimensions could be used to replicate the model.

Discrete voltage ports with 50 Ω impedance were used for the excitation and pick-up loops. The excitation port was placed on top of the semi-rigid sheath, connecting the sheath and the core wire which extends to the focal point of the dish. Similarly the pick-up loop port is placed as a wire port between the ground plane and the core wire forming the loop.

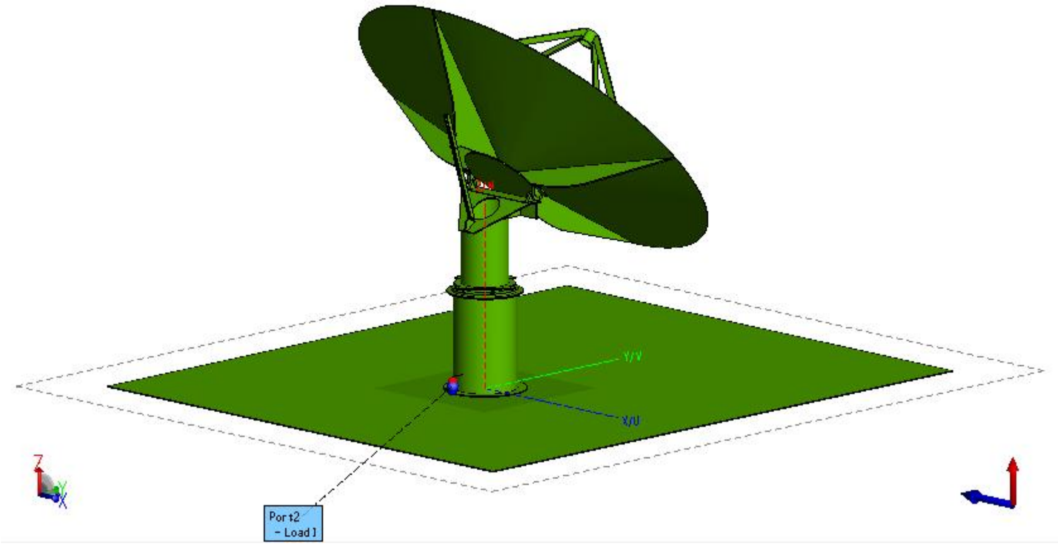

Figure 5.5: *EM plane wave simulating antenna excitation on FEKO model of KAT-7 with dish angled at 45 degrees. The ground plate is seen with this model and has dimensions of 924 mm by 861 mm.*

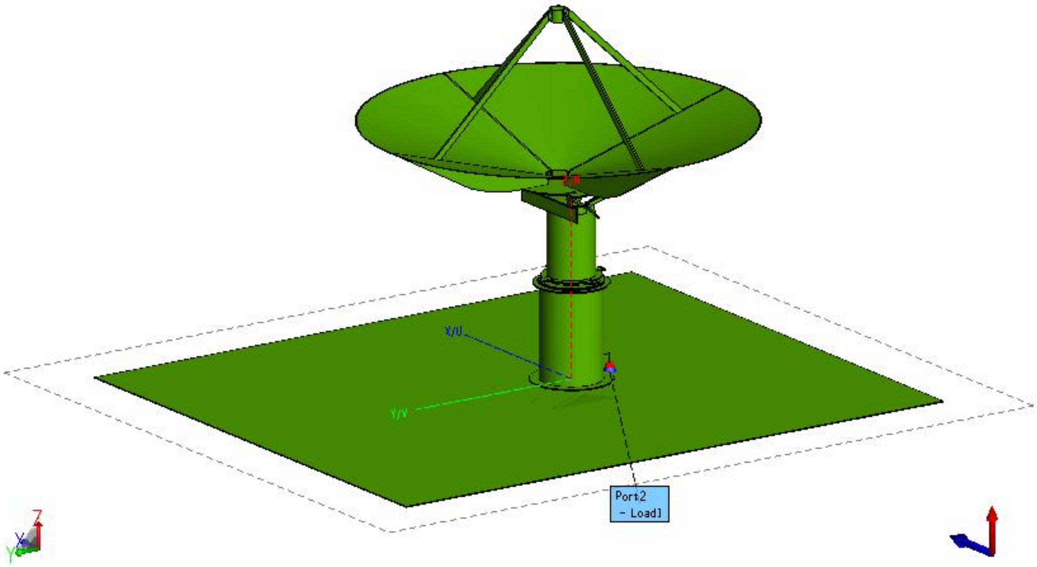

Figure 5.6: *EM plane wave simulating antenna excitation on FEKO model of KAT-7 with dish angled at 90 degrees.*

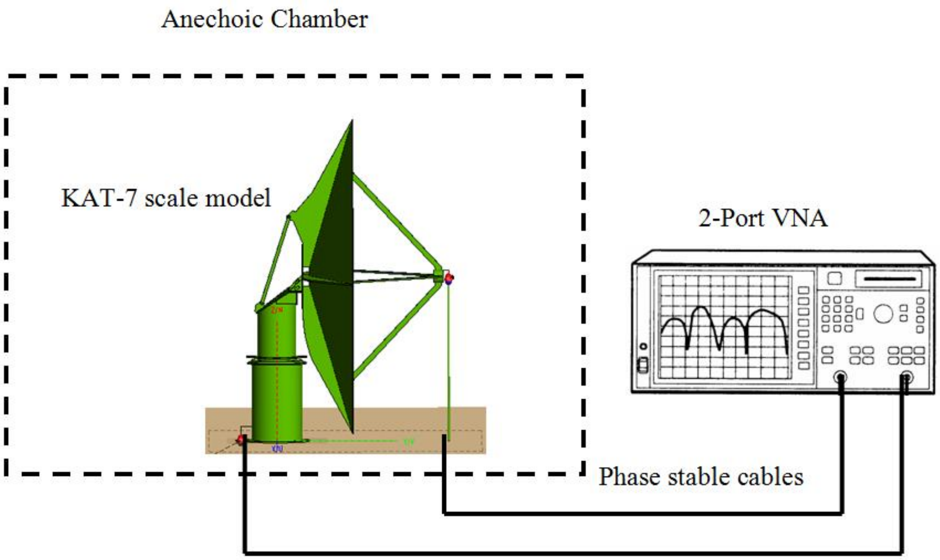

Figure 5.7: *Diagram of the setup for the KAT-7 scale model S-parameter measurement.*

These wire ports were defined with length of 3 mm and radius of 0.03 mm. The remaining core wires were defined as thin wires as well, with discretisation of the same value as the port. Surface meshing was chosen for triangles with an edge length of 14 mm. Due to the detail of the model, small features were discretised with extremely fine mesh triangles. This resulted in warnings and errors with the FEKO calculation. A function of the code, "Merge coincident vertices", was used after each meshing, to solve the discretisation problem. The resulting model was meshed with 33 segments and 20,637 triangles.

The numerical calculation could then be done between the two ports to correspond to the two-port S-parameter VNA measurement. With a memory requirement of only 8 GB, a normal four-core machine would be able to run the simulation, but using 32 nodes on the CHPC, the S-parameters for 51 discrete frequency points were calculated within a few hours. The frequency range used was chosen between 0.5 GHz and 5 GHz. When verified, the model can then be used for investigations into the 50 MHz high frequency content of lightning, as well as other RFI frequencies of interest up to 250 MHz.

Keeping the future simulations for lightning and RFI in mind, a plane wave excitation model was needed as well. If this model could be successfully verified, it could be used for indirect lightning strike investigations and external RFI sources as well. The frequency range for the plane wave experiment was chosen between 1 GHz and 6 GHz to correspond to the frequency range of the antenna used for the plane wave illumination and measurement of the model.

The scale model in FEKO was manipulated to adjust the dish to two different angles and orientations. For one scenario, the dish was angled at 45 degrees facing away from the pick-up loop (Fig. 5.5). For another scenario, the dish was changed to 90 degrees from the vertical, which is also defined as the stow position for the dish. For this dish angle, the set screw of the dish was orientated on the opposite side of the pick-up loop (Fig. 5.6).

An electromagnetic plane wave with 10 V/m value was defined in FEKO, which could be replicated in measurement by an antenna illumination of the dish in the anechoic chamber. The placement of the plane wave was chosen to propagate toward the side of the model, with vertical E-field orientation and horizontal H-field orientation. Opposing sides of excitation were used for the two models.

The semi-rigid and excitation port were removed and the pick-up loop port was replaced by a 50 Ω load. To be able to compare a measured S-parameter to the FEKO simulation, the current values through the 50 Ω load was requested as the solution to the simulation. In measurement, the S_{21} transmission parameter gives the comparison of the pick-up loop measured voltage wave, compared to the input voltage wave at the antenna. More detail on the measurement calculations in the following sections.

5.3 Verification by Measurement

The measurement verification technique was proven in the previous two chapters to be accurate. The same procedure is used for the KAT-7 scale model. However, to verify the use of plane waves in FEKO, additional measurements are made using a log-periodic dipole antenna (LPDA).

5.3.1 S-parameter Measurement

The S-parameters are measured to verify the computational model, and to use this method of current injection to do further modelling of simulated direct lightning strikes. The measurement was done in the anechoic chamber (Fig. 5.3) similarly to the previous models. A diagram of the measurement setup is shown in Fig. 5.7. The VNA was calibrated using a SOLT procedure, where the connection point of the phase stable cable to the model sets the calibration plane. With future radio astronomy for the anticipated SKA to be conducted at frequencies between 70 MHz and 10 GHz, and the KAT-7 operating range between 500 MHz and 2.5 GHz, a scaled frequency range of 0.5 GHz to 5 GHz was chosen. The anechoic chamber absorption limits the lower frequency, and the upper frequency is limited by the computational cost of modelling in FEKO. The measurements were carefully taken with 201 discrete points and the results recorded to file for all the S-parameters.

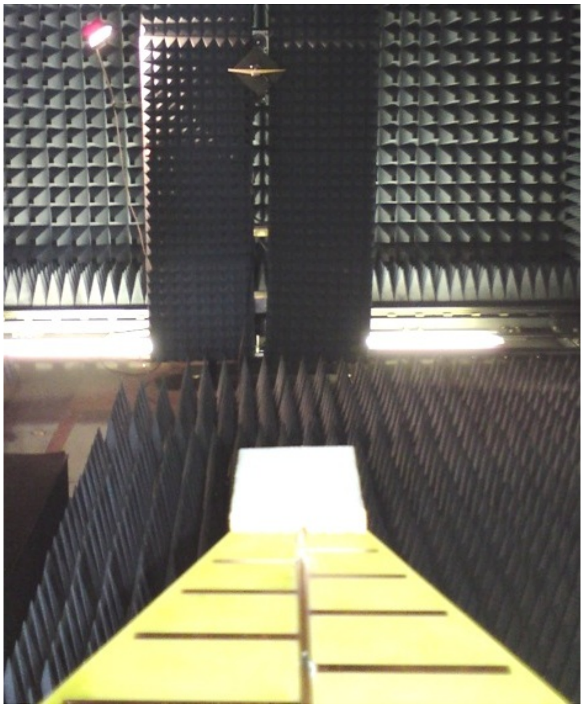

Figure 5.8: *Photograph showing the characterisation of LPDAs used for plane wave excitation in anechoic chamber.*

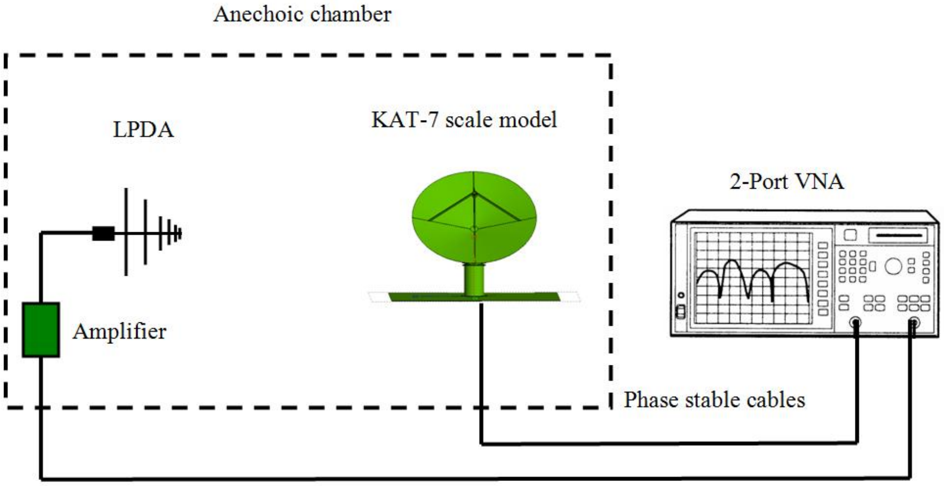

Figure 5.9: *Diagram of the setup for the KAT-7 scale model plane wave antenna measurement.*

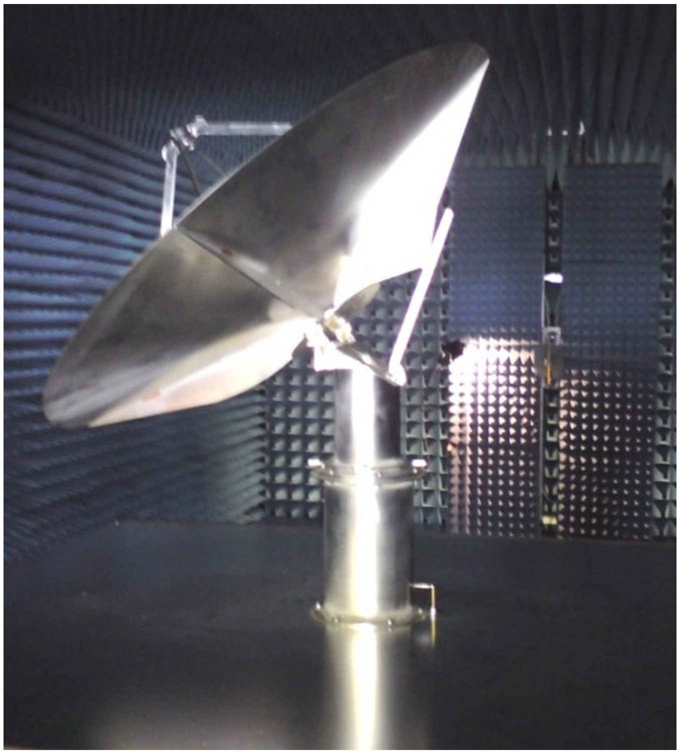

Figure 5.10: *LPDA plane wave measurement verification of KAT-7 design scale model in anechoic chamber. For this measurement the dish is angled at 45 degrees facing away from the pick-up loop.*

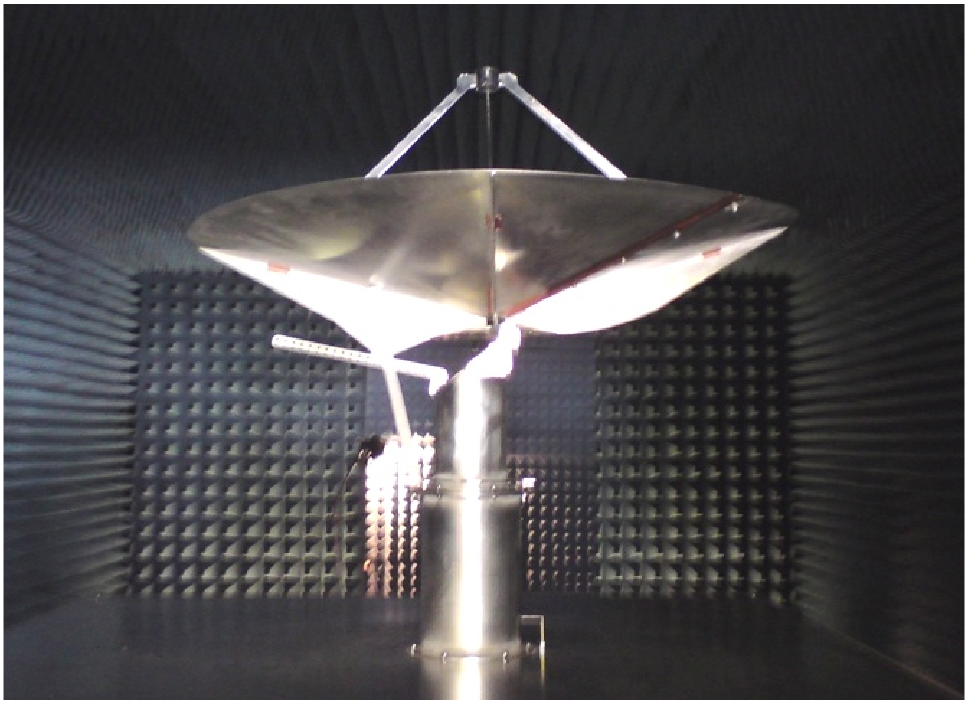

Figure 5.11: *LPDA plane wave measurement verification of KAT-7 design scale model in anechoic chamber. For this measurement the dish is angled at 90 degrees and the elevation set screw is on the opposite side of the pick-up loop.*

5.3.2 Plane Wave Measurement

We plan to use plane wave excitations to model indirect lightning strikes. To verify the modelling, a plane wave measurement using an LPDA was done. Two LPDAs were characterised beforehand using other known antennas for the three-antenna method [58]. The photograph in Fig. 5.8 shows the one LPDA facing the second LPDA on the opposite side of the anechoic chamber.

After the antennas were characterised, the gain for the LPDA was calculated. Fig. 5.15 near the end of this chapter shows the antenna gain plotted over the frequency range.

Then the setup was changed to have one LPDA on the far end of the chamber, connected to port 2 of the VNA through an uni-directional low-noise amplifier. However, the VNA was programmed to attenuate the input signal by the same factor as the amplifier. The amplifier is installed in the chamber specifically for antenna measurements.

The calibration of the VNA was done for 201 discrete frequency points between 1 GHz and 5 GHz, where the antenna gain is constant. A good calibration was obtained with the noise floor level around -90 dB as shown in Fig. 5.15.

The scale model, with dish angled at 45 degrees, was placed on a perspex mount inside the chamber and orientated in the same way as the FEKO simulation. Port 1 was then connected to the pick-up loop of the model. In doing a S_{21} measurement, it allows the installed amplifier to operate correctly. And with $S_{21} = S_{12}$, this means that the pick-up loop voltage is measured due to the plane wave excitation of the antenna. Fig. 5.9 shows a diagram of the layout for this measurement.

The procedure is repeated for the model dish adjusted to 90 degrees to the vertical and orientation changed by 180 degrees. Photographs of the 45 degree dish plane wave measurement and 90 degree plane wave measurement are shown in Fig 5.10 and Fig. 5.11 respectively.

5.4 Comparison of Results

The S-parameter verification results are given in Fig. 5.12 to Fig. 5.14.

5.4.1 S-parameter Measurement Results

The S_{11} magnitude plot for the FEKO results follows the measured results plot closely to within less than 1 dB, except at the resonances (see Fig. 5.12). Slight misalignment of resonances can be attributed to small errors (less than 1 mm) in the model definition in FEKO. The first resonance visible at just above 500 MHz corresponds to a half-wavelength resonance of the support struts' dimension on the dish. At 880 MHz and 1.76 GHz, the feed-port semi-rigid cable dimension forms single and multiple wavelength resonances.

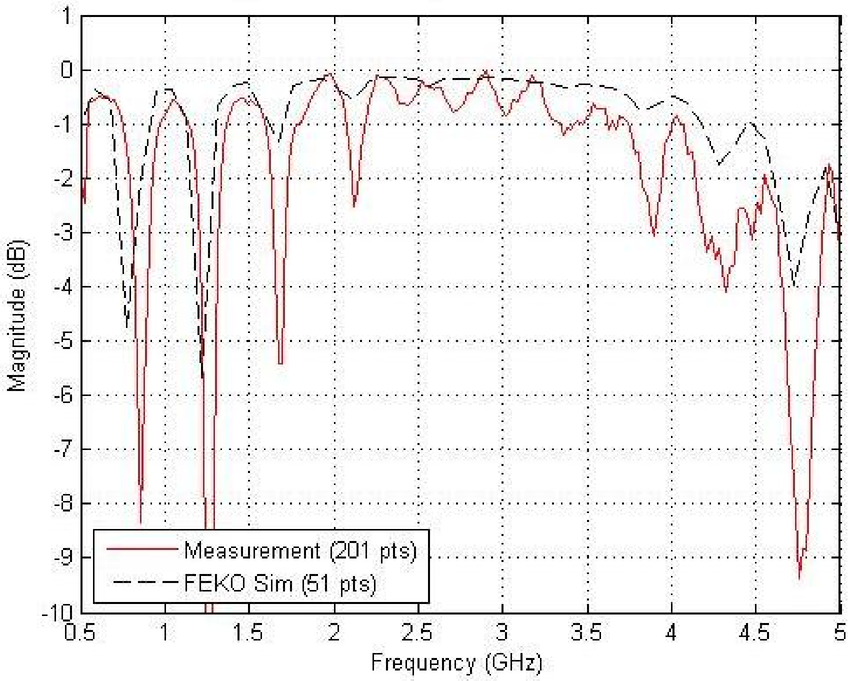

Figure 5.12: *S_{11} magnitude comparison of ADM scale model measurement and FEKO simulation.*

Another multiple wavelength resonance is seen at 1.30 GHz, where the ground plate side-dimension is 924 mm. A resonance at 2.04 GHz is caused by reflections inside the yoke part of the pedestal, which has an opening for access. This dimension between the yoke top and pedestal top is 147 mm.

In Fig. 5.13 the magnitude comparison shows that for most of the results, FEKO correlates to within 5 dB to the measurement. Only a few resonant frequencies show larger variation with the worst being 17 dB difference at 2.65 GHz.

For S_{22}, the agreement between FEKO and measurement is within 0.3 dB between 0.5 GHz and 1.7 GHz. In the frequency range of 1.7 GHz to 3 GHz, the values differ by no more than 1 dB, and the main resonance aligns. Above 3 GHz, the plots diverge by up to 3 dB, as can be seen in Fig. 5.14.

5.4.2 Plane Wave Measurement Results

Before the plane wave measurement results can be compared to the FEKO simulation, the simulation current values need to be converted to the coupling parameter S_{21}, and the gain of the antenna needs to be accounted for in the measurement.

The measured S_{21} magnitude in dB, was adjusted by subtracting the dB gain of the antenna:

$$S_{21actual} = S_{21measured} - G_{LPDA}\ dB \tag{5.1}$$

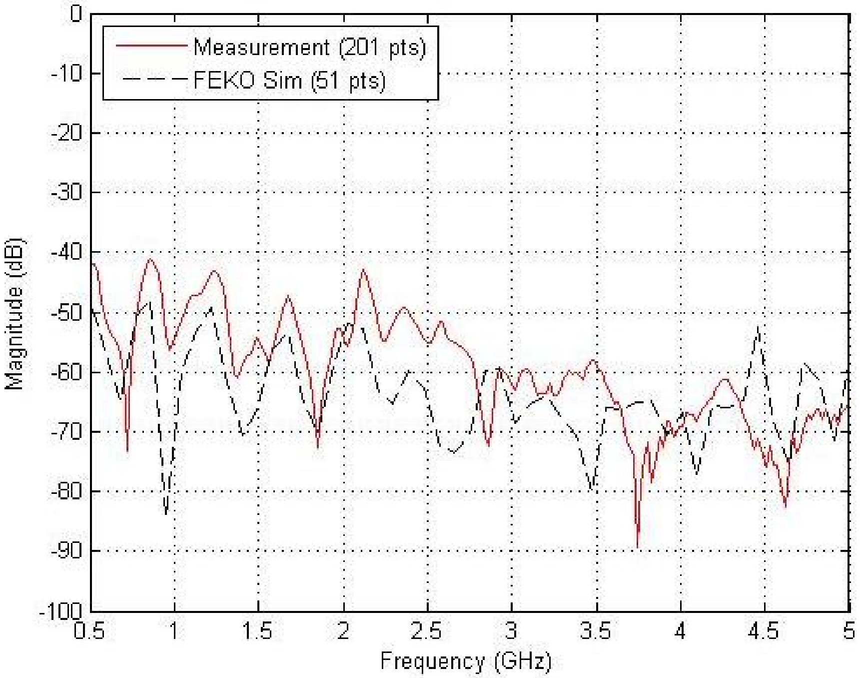

Figure 5.13: *S_{21} magnitude comparison of ADM scale model measurement and FEKO simulation.*

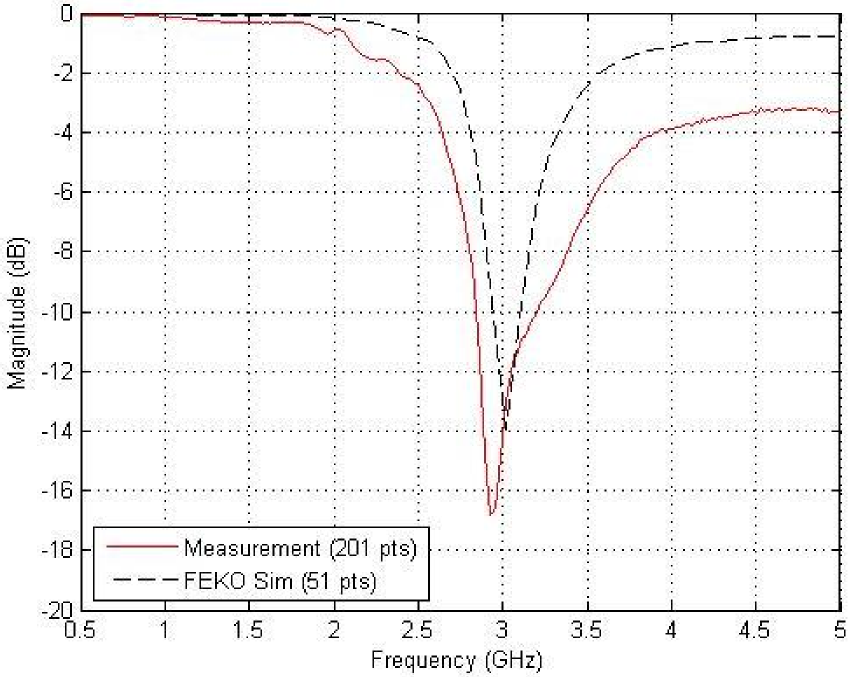

Figure 5.14: *S_{22} magnitude comparison of ADM scale model measurement and FEKO simulation.*

With the calibration done up to the model SMA port and the LPDA connection, this was the only adjustment that needed to be done. The antenna mismatch was found not to make a noticeable difference to the measured value.

From the FEKO simulation, the current value on the impedance port is given in dB for each frequency. This means that the current value has already been normalised to its reference. The dB-current values are converted back to linear and with the impedance vale of 50 Ω, this implies a voltage value equal to the current multiplied by the impedance:

$$V_{out} = 50 * 10^{I_{dB}/20}\ V \tag{5.2}$$

To calculate S_{21} for each frequency, the input voltage V_{in} is taken as equal to 1 due to the normalisation, and the S_{21} dB magnitude values are calculated by:

$$S_{21FEKO} = 20 * log_{10}(V_{out}/V_{in})\ dB \tag{5.3}$$

where V_{out} is the linear voltage calculated from the current.

The values of S_{21FEKO} in equation 5.3 are compared to the values of $S_{21actual}$ (from equation 5.1) in Fig. 5.15 for the dish angled at 45 degrees. For 51 frequency points calculated in FEKO, the results show conformity to within 5 dB across the frequency band.

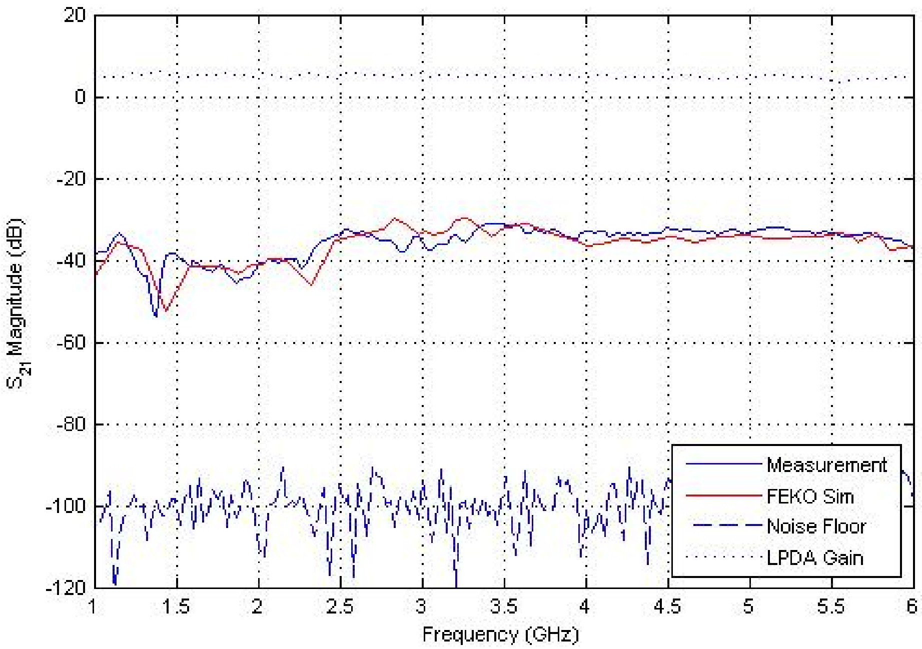

Figure 5.15: *S_{21} magnitude comparison of plane wave excitation ADM scale model measurement and FEKO simulation. Here the dish is angled at 45 degrees and facing away from the pick-up loop. The antenna gain and noise floor level for the measurement is shown as well.*

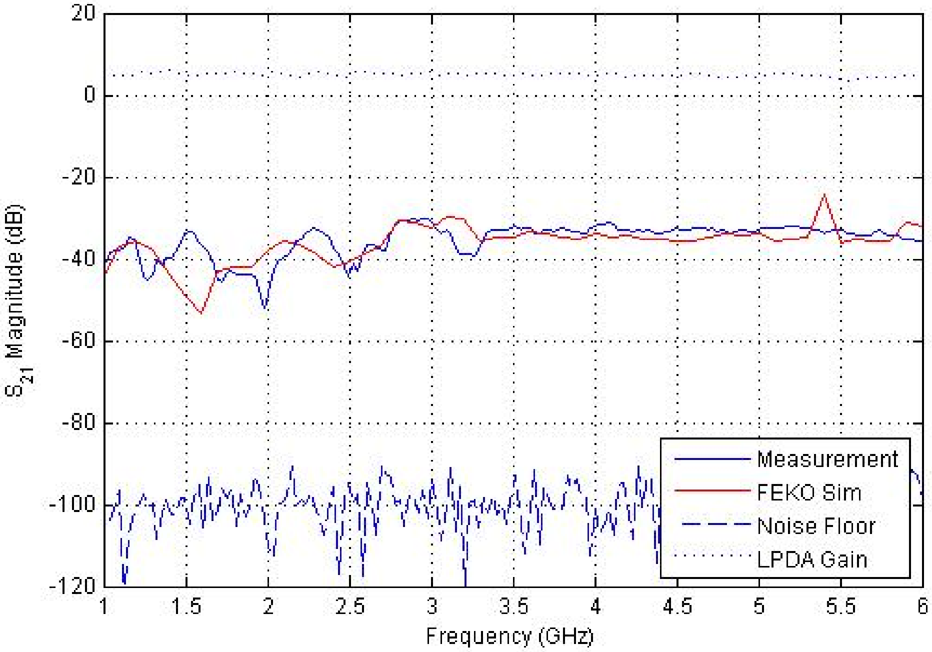

Figure 5.16: *S_{21} magnitude comparison of plane wave excitation ADM scale model measurement and FEKO simulation. Here the dish is angled at 90 degrees and the elevation set screw on the opposite side of the pick-up loop. The antenna gain and noise floor level for the measurement is shown as well.*

Only three points have higher disagreement, where resonances are slightly misaligned. This is due to minor errors in the geometry.

The comparison of results for the 90 degree dish angle is shown in Fig. 5.16. These plots show similar correlation and have variation of less than 5 dB, except at three resonant points where the difference is larger. As mentioned in section 5.3.2, the antenna gain and noise floor level are shown in these figures as well.

5.5 Conclusions

This chapter detailed the production of a physical scale model which was simplified from the actual KAT-7 design. Computational modelling in FEKO was verified with rigorous measurement of the model in an anechoic chamber. S-parameter measurements verified the computational model for further investigation into direct lightning strikes using FEKO.

Indirect lightning strikes can be studied in FEKO as well, after antenna plane wave measurements verified the numerical model.

With the research completed at this stage of the project, a secure foundation was created for specific lightning protection and RFI mitigation investigations using FEKO.

– Even if you are on the right track, you will get run over if you just sit there –

– Will Rogers –

Chapter 6

KAT-7 Lightning Protection

Direct and indirect lightning strikes on the verified FEKO KAT-7 design scale model are studied in this chapter. A direct strike is modelled with a current injection on the dish lightning rod, while EM plane waves from different directions represent indirect lightning strikes. The design layout of the lightning down conductor, specifically over the elevation and azimuth bearings, is optimised for RFI mitigation and cost-effectiveness. Resonant frequencies are investigated to identify problem areas in order to effectively mitigate RFI. The modelling of the foundation steel reinforcing as part of the earth electrode for the lightning protection system (LPS) is discussed as well. The investigation considers interconnection of steel elements as required by international standards. The concrete and soil are modelled as a homogeneous medium below a Sommerfeld integral ground plane in FEKO. From the simulation results, recommendations were given to the KAT-7 design team.

6.1 Introduction

To predict the behaviour of lightning currents on and electromagnetic fields inside one of the structures accurately, computational electromagnetics is chosen, which is the numerical solution to Maxwell's equations. Successful verification of numerical models through measurements and comparison to another numerical code has given us confidence to utilise accurate scale models in FEKO to investigate lightning and RFI.

From discussions with the KAT-7 design team, main areas of concern were identified. These included the design and layout of the lightning protection system (especially at the bearings, where movement had to be accounted for), as well as the cable entry from below the pedestal floor, and shielding of the inside. However, one of the main driving factors behind the design is cost, and this is especially true for the MeerKAT's 80 antennas. If the LDC design layout could be planned effectively to keep the cost of material low and help in RFI mitigation as well, the project would benefit greatly.

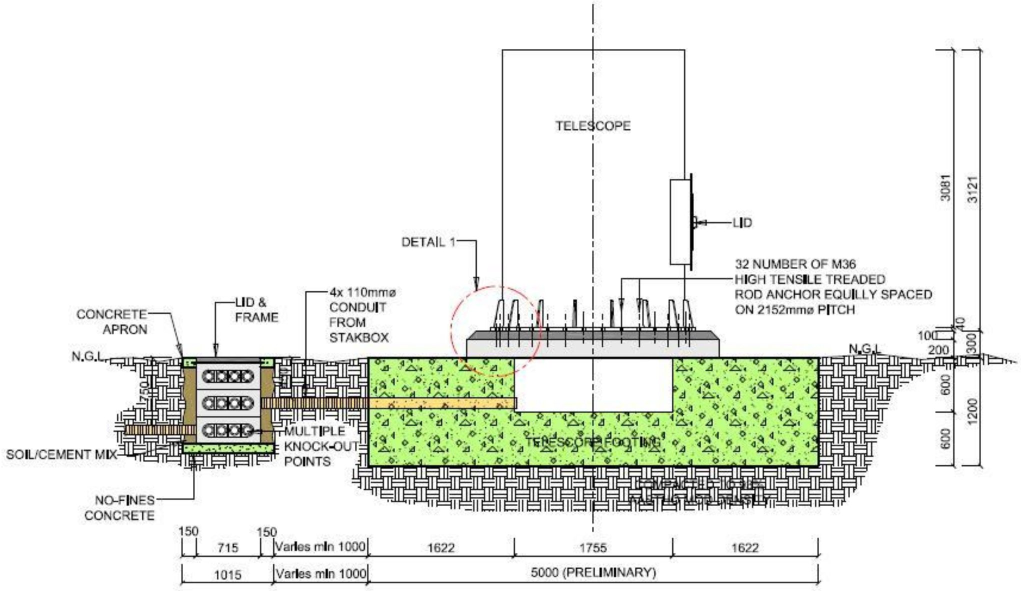

Figure 6.1: *SA SKA design drawing with detail on the KAT-7 base. The pedestal is elevated onto a concrete lip to allow levelling at the construction phase. The structure is then effectively lifted from ground level by 32 bolts.*

6.2 CEM Model Used for RFI Investigations

One of the major advantages of using a CEM scale model above a physical scale model, is that the conductivity can actually be scaled in the CEM model. This cannot be done for physical models, as conductive materials with 20 times better conduction either do not exist, or have to be supercooled to obtain the conductivity [40]. For the different metals used in the full-scale design, the scaled conductivity was included with skin effect in the FEKO scale model. It was found that the results with the inclusion of skin effect were almost exactly the same as with the use of PEC. Further modelling only used PEC for all metallic parts. However, where soil is simulated, the soil conductivity is scaled.

The precise layout for different options of the KAT-7 LDC was added to the FEKO model. The base of the actual pedestal is designed in such a way as to fit over 32 bolts which are securely embedded in the concrete. The design drawing for the pedestal base is shown in Fig. 6.1.

The concrete foundation has a 600 mm deep cylindrical space provided for cables entering the pedestal from below ground level. The lip of this opening is constructed to be 300 mm above the ground level, and the foundation bolts protrude from this lip. Two nuts are placed on each bolt, allowing the pedestal to be levelled during construction (see Fig. 6.2). With this slight elevation of the pedestal, stray currents can leak around the edges of the pedestal base and introduce electromagnetic interference to the inside of the pedestal.

Figure 6.2: *Photographs of the foundation showing the foundation bolts on the concrete lip on the left, and the space provided for cable entry on the right.*

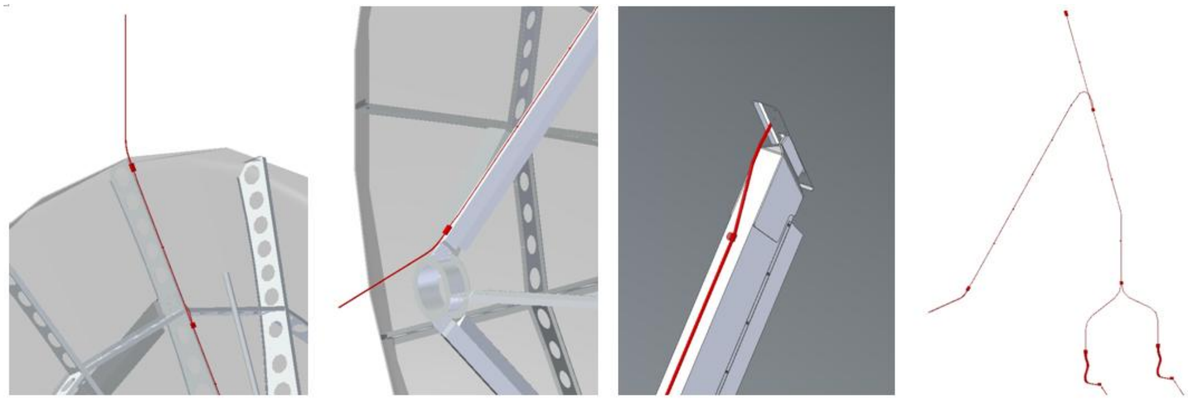

Figure 6.3: *From left to right (f.l.t.r.): The LDC dish lightning rod; The receiver lightning rod; The area where the receiver lightning rod conductor goes through the dish; The connection between the conductors from the receiver rod and the dish rod.*

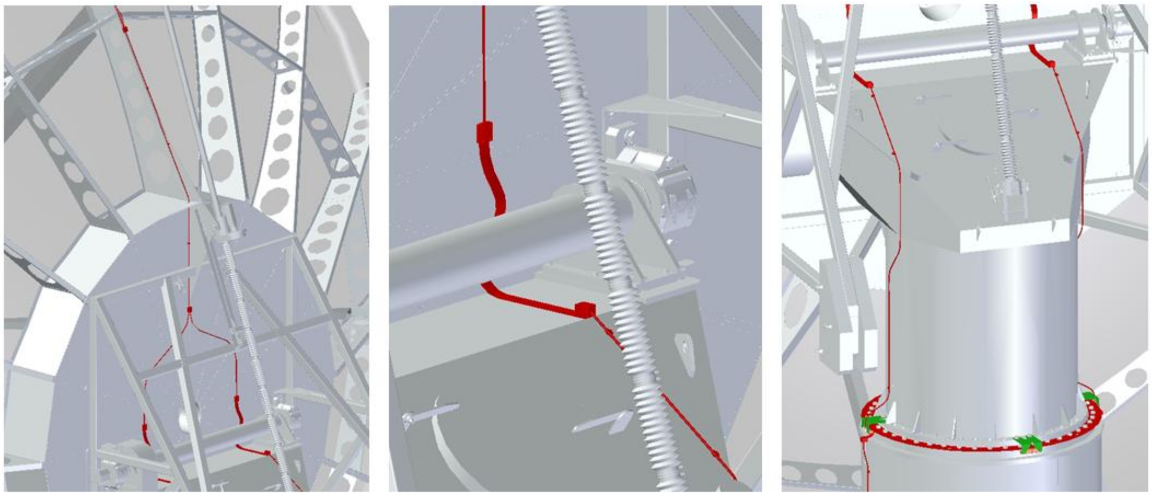

Figure 6.4: *F.l.t.r. The LDC on the backing structure where it splits in two; The strap shown here going beneath the elevation bearing axle; The ring-plate connection to 4 copper shoes over the azimuth bearing.*

Two lightning rods are placed on the dish, one at the focal point receiver, and one at the top of the dish for the dish facing forward (shown in the two pictures on the left-hand side of Fig. 6.3). The down conductor attached to the receiver rod, is connected to the top strut using conductor clamps. This conductor joins the top rod's conductor at the back of the structure after going through an opening in the dish (right-hand side pictures of Fig. 6.3). The opening allows the connection of the top strut to the dish backing structure.

The joint conductor splits in two conductors and is then connected, either over or beneath the elevation bearings, onto the pedestal. From here the two conductors go down the sides of the pedestal and connect to a ring plate above the azimuth bearing (Fig. 6.4). The ring plate is connected over the bearing onto four copper shoes which are spring-loaded to ensure good galvanic connection. These shoes are directly connected to the bottom steel part of the pedestal and depend on the steel structure and foundation bolt connections for current conduction to ground. The bolts are connected to a ring inside the concrete, having four bolted lug connections going to the ring earth conductor, which forms the earth electrode together with 8 copper rods.

The numerical model with the LDC included is shown in Fig. 6.5 above a perfectly conducting ground plane. Here a direct lightning strike is modelled.

For the investigations in this chapter, it was decided that the consideration of soil does not affect the discussion sufficiently to warrant the substantial overheads in computation necessary for its inclusion. However, specific questions regarding the steel reinforcing inside the concrete are discussed in section 6.6, where real earth is modelled as a Sommerfeld integral ground plane.

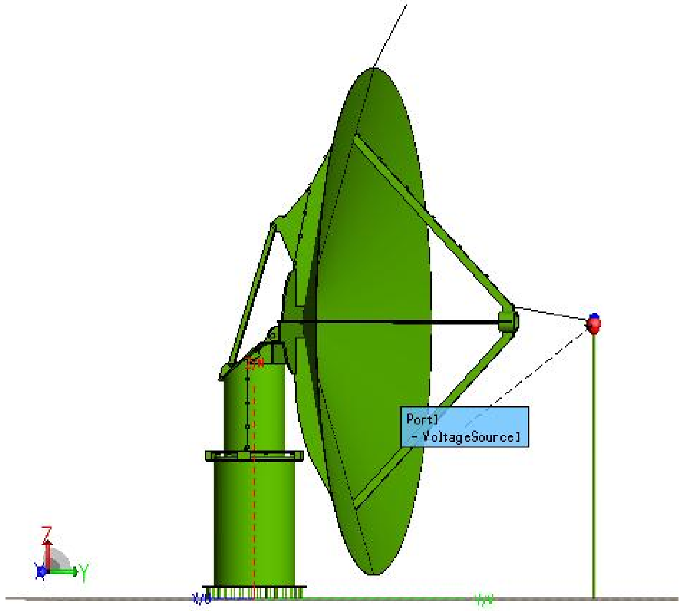

Figure 6.5: *KAT-7 FEKO model with lightning rods and complete LDC added. The model is raised onto the foundation bolts, which in the model's case is connected to the ground plane. A direct lightning strike is modelled by a current injection at the receiver lightning rod.*

6.3 Equivalent Lightning Excitations

The following sections give detail on the simulation of direct and indirect lightning strikes through different methods of excitation in the FEKO modelling. Initial results are discussed.

6.3.1 Simulated Direct Lightning Strike

We elected to investigate the highest probable lightning frequency at 50 MHz only. Beyond this point the RFI becomes negligible according to IEC standards [16]. With the scaling factor of 20, the simulation frequency was 1 GHz. This fits within the frequency range for which the model was verified.

A direct strike was modelled with a current injection via a 50 Ω wire-port at the dish receiver lightning rod as shown in (Fig. 6.5). Similar excitations have been used in [37, 38, 39] to simulate lightning current return strokes.

To investigate problematic areas during a lightning strike, surface currents and electric fields were requested as the calculations to be done by FEKO. Meshing resulted in 280 segments and 22,538 triangles. This required 10 GB of memory, and the simulation was run on a four-core machine, with 15 GB of memory available, in just under five hours.

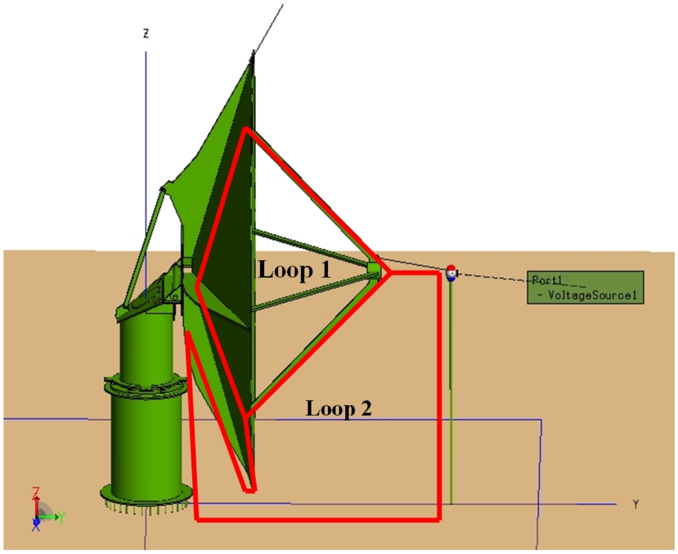

Figure 6.6: *Current injection through lightning rod onto struts of dish for equivalent direct-lightning strike. Loops are formed between the dish struts, structure and ground.*

6.3.2 Interpretation of Direct Strike Results

Several interesting, and perhaps unexpected, features are found with the direct injection method. From a high-level perspective, the currents on each strut are approximately equal. However, on closer scrutiny, there are several loops that are formed when the ground connected injection cable similar to the physical model semi-rigid is employed. Some of these are highlighted in Fig. 6.6.

The current density and electric field plot of Fig. 6.7 should also be considered in this discussion. Some capacitive coupling is discernible between the dish and the pedestal at mid-pedestal height with the dish in this position. The lower strut also forms a common path between the identified loops 1 and 2. As a consequence, the lower strut current density differs from the other struts. Additionally, the ground plane forms the return path for the current injection.

The question arises as to whether or not this is a fair representation of a direct strike, as in real conditions, no such directed return path is created. Measurements have been made on the actual XDM using this technique. The immediate value of this approach is that current paths can be determined using CM current probes and this readily identifies cable barriers that are not sufficiently protected.

What the results show is that the injection method does affect the resulting currents due to the loops being formed. However, by placing the injection conductor further away from the pedestal base, the influence of the injecting current magnetic field is lessened. Recommendations in this regard are alluded to in [11], where different configurations of lightning excitation with a continuous CW current source are compared to each other.

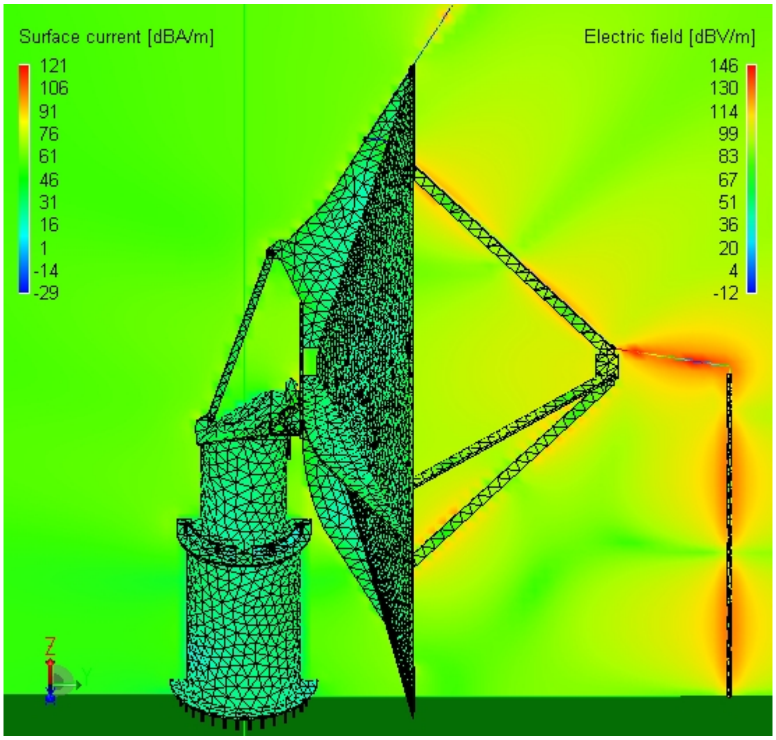

Figure 6.7: *Computed current density and electric field results for the equivalent direct-lightning strike. Currents are more uniform on each strut and the capacitive coupling between dish and pedestal at mid-pedestal height is just apparent.*

With the test setup recommended, the earthing is used as the return path, as with our testing. Furthermore, the higher coupling level is shown with an angled excitation conductor closer to the structure being tested. Guidelines on minimum distance away from the structure is given as a distance more than three times the diameter of the structure for tall structures.

In Fig. 6.8, a comparison between the electric field results for an equivalent direct strike is shown for two cases. The first case is where the pedestal bottom is open (which was relevant for an initial wooden floor design) and cable shields enter the pedestal between the bolts that the pedestal rests on. The following scenario shows where the bottom of the pedestal is totally shielded by a metallic plate, and cable shields are concentrically bonded to the plate upon entering. The plate allows shielding of between 40 dB and 50 dB toward the inside of the pedestal, compared to an open pedestal. Feedback in this regard was important to the KAT-7 design team.

6.3.3 Simulated Indirect Lightning Strike

By way of contrast, an indirect lightning strike was modelled with a 10 V/m EM plane wave from 12 different directions, which can be seen in Fig. 6.9. The plane-wave propaga-

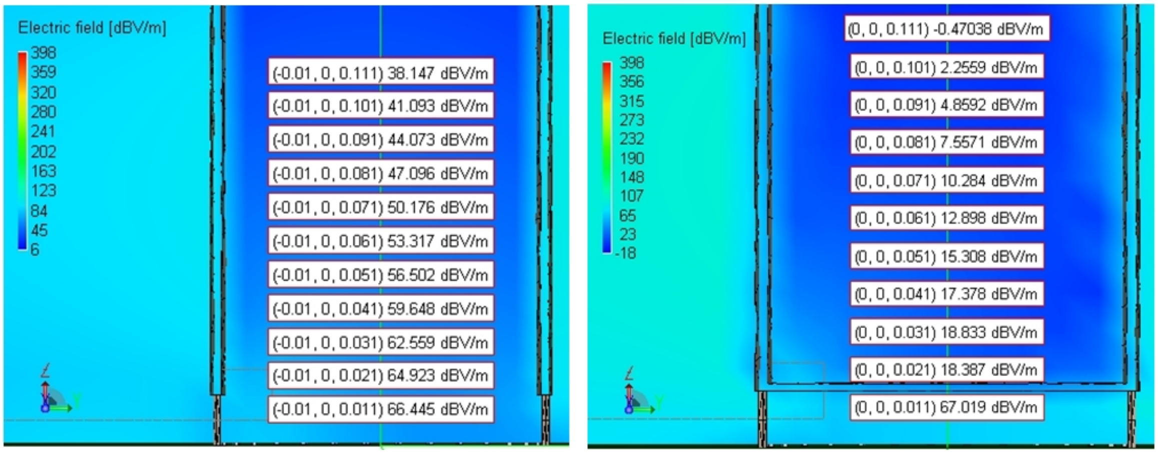

Figure 6.8: *Comparison of electric field results for an equivalent direct strike. A cross-section of the bottom part of the pedestal is shown with an open floor on the left and a shielded floor on the right. The electric field values are shown for points on the z-axis in the middle of the pedestal.*

tion is perpendicular toward the dish with vertical electric field orientation and horizontal magnetic field orientation. The current density and E-field results in FEKO are calculated for each of these plane waves at 1 GHz.

6.3.4 Interpretation of Indirect Strike Results

Fig. 6.10 shows the current density arising from such an indirect excitation toward the front of the dish. An immediate observation is that the top and bottom struts have substantially higher induced currents, because they form a loop cutting the magnetic field. In this case there is no preferential ground return orientation.

From these studies one could consider which struts give the most protection to the galvanically conducting cables running to the feed-horn. In the case where the dish position is most frequently angled at 45 degrees to the horizontal, and indirect strikes are most common, the side struts would afford the best shielding to the cables.

Throughout the design phase of KAT-7, this thinking was used to maximise the use of the metallic pedestal interior as an EMC-zone. Careful inspection of Fig. 6.10 also shows interior surface current density which is worsened by poorly-bonded cabling and incomplete barriers at the base for an equivalent indirect lightning strike.

6.4 Lightning Down Conductor Investigations

For the LDC system, different configurations of the conductors and their connections over the bearings were considered. The main components of the LDC include the lightning

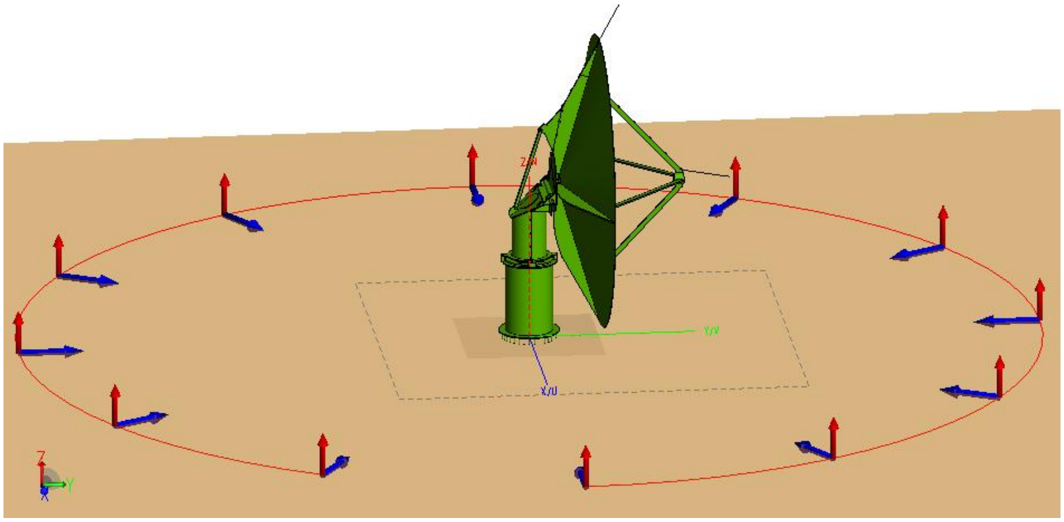

Figure 6.9: *Plane-wave excitation from different directions, modelling indirect lightning strikes.*

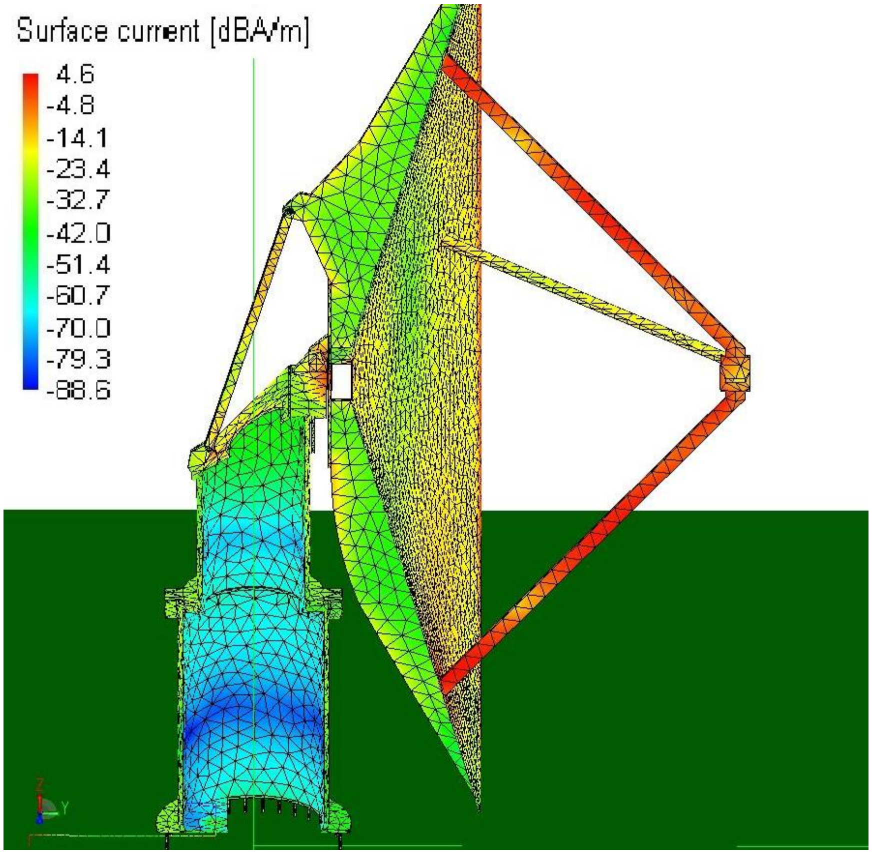

Figure 6.10: *Sectioned view of plane-wave excitation from the front of the dish. Higher current density is apparent on the lower and upper struts.*

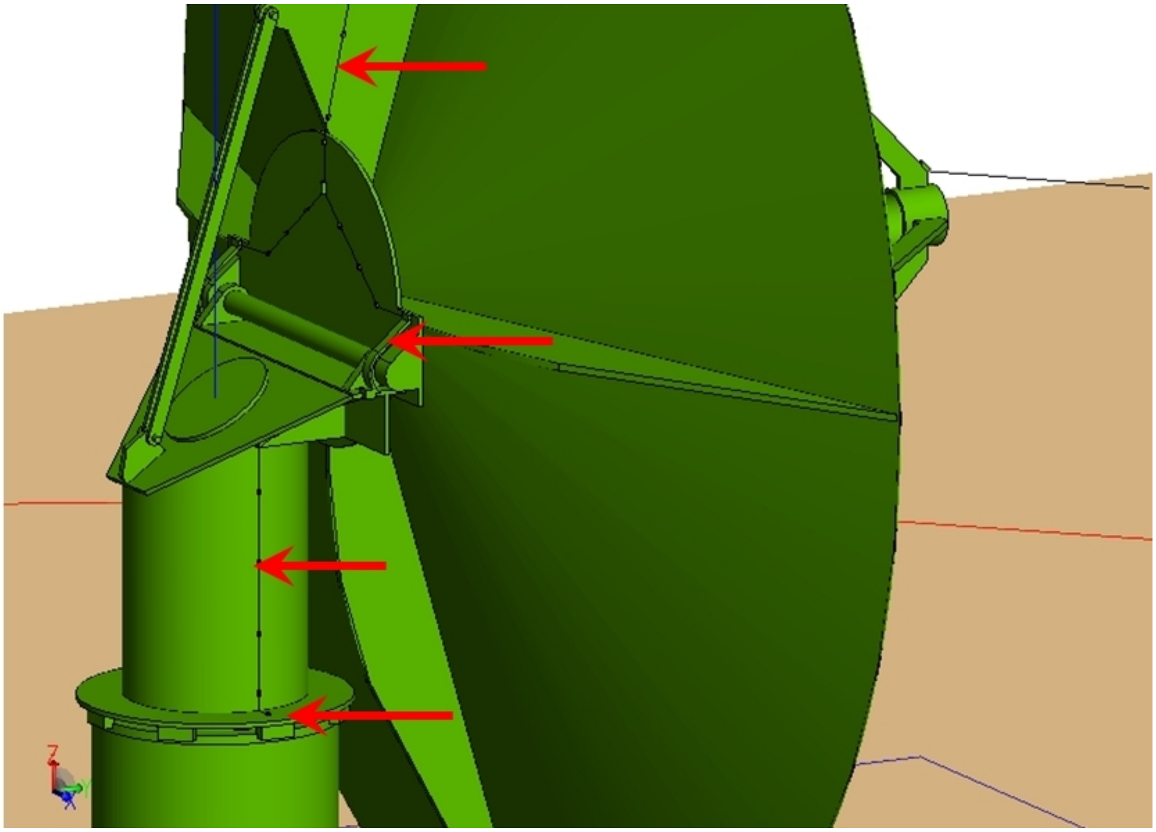

Figure 6.11: *KAT-7 scale model in FEKO, with lightning down conductors (1^{st} and 3^{rd} arrow from the top), straps over elevation bearings (2^{nd} arrow), and shoes over azimuth bearing (4^{th} arrow).*

rods, the conductors and their clamps, flexible strapping over the elevation bearings and spring loaded conductive shoes over the azimuth bearing. Some of these elements are identified with arrows in Fig. 6.11.

Running parallel with the pedestal manufacturing process, the KAT-7 office requested RFI feedback on the LDC design over the bearings, to include connection points for the conductor clamps and LDC fittings in the design. In some cases where extended computational modelling made prompt feedback difficult, the manufacturing had to continue as planned. In these cases, retrofitting had to be done to implement the recommendations.

6.4.1 LDC Over Elevation Bearings

The elevation bearings were identified as possible problem areas regarding lightning protection and RFI. Specific attention was given to detail of the LDC over these bearings. The elevation bearing is shown as per the design on the far left in Fig. 6.12. The picture in the middle shows how the design is scaled down for numerical simulations. An infinite perfect electric ground plane was used for all simulations.

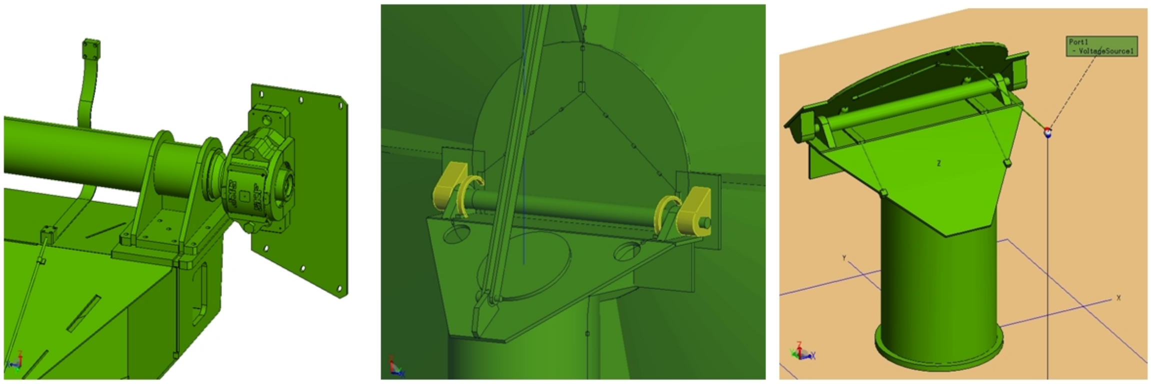

Figure 6.12: *F.l.t.r. Full scale elevation bearing design; Scale model straps over elevation bearings in FEKO; Simplified FEKO structure with straps over elevation bearings.*

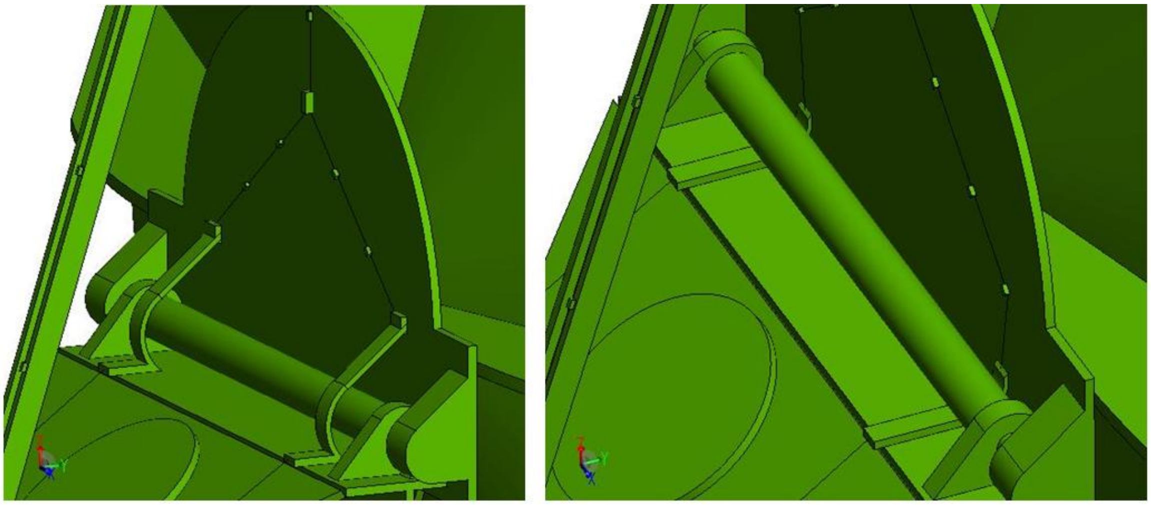

Figure 6.13: *The LDC straps are shown here connected over the elevation bearing axle on the left, and connected beneath the axle on the right.*

The discretised model in FEKO was too large to run on a normal four-core machine. Thus the simulation was submitted to the CHPC. However, with increased usage and long queues, valuable time was lost with unavailability of the CHPC. We decided to further simplify the model to exclude the dish part, in order to run simulations on single machines instead of the clusters. Using the simplified model allowed EMC principles to be investigated and different design scenarios compared to each other. The simplified structure without the dish is shown to the right of Fig. 6.12.

The main concern was whether the LDC straps should go over the bearing axle or underneath it. Here the optimal lightning protection is desired at the lowest cost. An initial design had the straps connected over the bearing axle. To reduce the length of strapping to keep costs low, the design was changed to go beneath the axle. The question

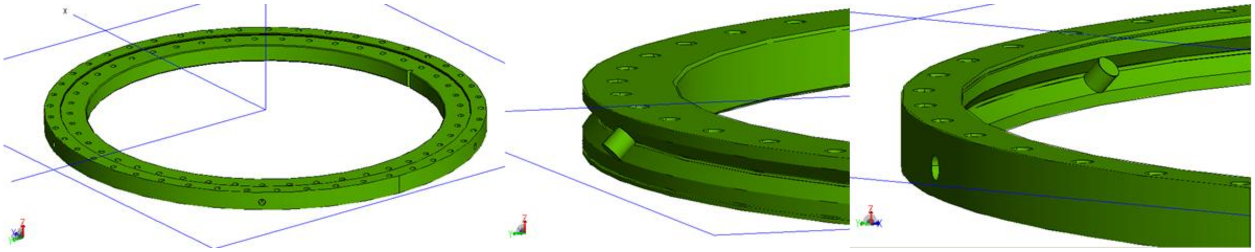

Figure 6.14: *Full scale azimuth bearing design, showing the inner ring of the bearing in the middle picture and the outer ring in the picture on the right. One of the 71 roller elements is shown, designed in such a way to be able to take the weight of the yoke and dish.*

was raised as to which design would render the optimal protection.

The simplified model excluding the dish was used to calculate the surface currents and electric fields at 1 GHz in FEKO. Two scenarios were investigated, namely with the longer straps going over the axle, and the shorter straps connected beneath (Fig. 6.13).

6.4.2 LDC Over Azimuth Bearing

The azimuth bearing consists of an outer ring, an inner ring and 71 bearing roller elements. The outer ring bolts onto the bottom part of the pedestal, and the inner ring is bolted to the top part of the pedestal, called the yoke. The bearing design is such that the roller elements are cylindrical and oriented in a 45 degree angle to be able to carry the weight of the yoke and dish. Fig 6.14 shows the design of the rings of the bearing, as well as one of the 71 roller elements.

The two lightning down conductors coming from the elevation bearing terminates on a 360 degree connected steel ring which is bolted on the bottom lip of the yoke, and extends over the radius of the bearing. Four spring-loaded copper shoes bolted onto the outer ring of the bearing act as a brushing system to connect to the steel ring above. The full-scale design for one of these shoes is shown on the far left picture of Fig 6.15. The following picture to the right shows the scale model design in FEKO for the 4 shoes. However, with the unavailability of the CHPC, the dish was left out of this model and the simplification of the pedestal and yoke is seen in the third picture of Fig. 6.15.

Here we focused on the amount of shoe-connections needed to effectively protect the azimuth bearing against lightning, keeping cost in mind. Simulations were done for different scenarios of the LDC design over the bearings, including layouts with 2, 4 and 8 shoes, and with or without the conductors from the elevation bearing.

Perfect connections between the bearings and metallic parts of the structure were assumed, which allows use of the metallic structure as part of the LDC system [9]. In the implementation, however, the mechanical engineering team, although mindful of EMC

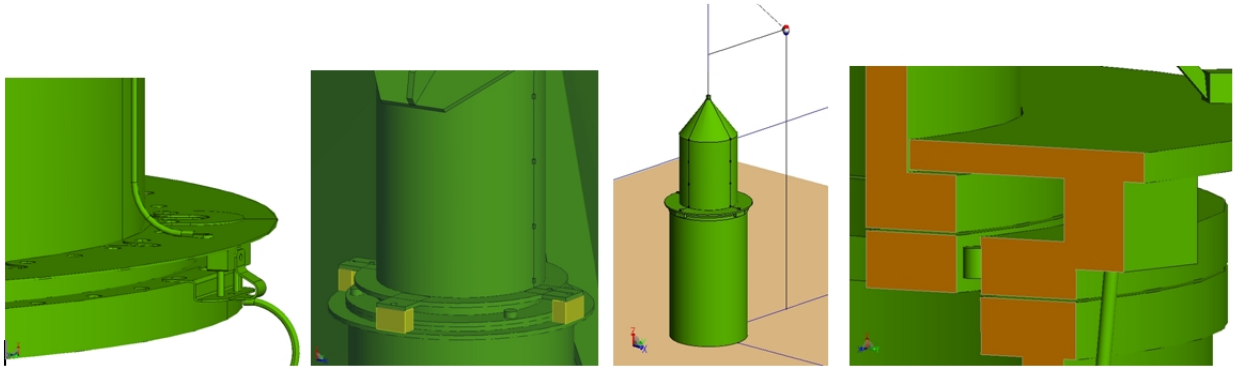

Figure 6.15: *F.l.t.r. Full scale azimuth bearing design; Scale model design in FEKO of shoes over azimuth bearing; Simplified FEKO model with shoes over azimuth bearing; Detail of air gap simulating coated surface between bearing interfaces.*

matters, made corrosion protection a priority. Consequently, the metal interfaces were painted or gun-coated, which introduced capacitive coupling specifically at the bearing interfaces. The last picture in Fig. 6.15 shows a section view of the bearing and shoe interface, where these coated surfaces are modelled with an air gap.

Two different orientations of the dish, at 45 degrees and at 90 degrees, were considered. Direct current injection of 1000 V and 100 A, and a plane-wave excitation of 100 V/m, were used to evaluate as many as possible scenarios for which the coupling levels could be compared. The results calculated in FEKO were the surface current density and electric field.

6.4.3 Results for LDC Over Elevation Bearings

Each scenario was excited by the same level of current or electric field, and the surface current density and electric field result levels were compared to each other for the different scenarios. Specific levels were not considered for this investigation.

Surface current density results are shown in Fig. 6.16 and Fig. 6.17 for the straps connected over and beneath the bearing axle respectively. The indicated levels of surface current density agree to within 0.4 dB for these two scenarios, except at the point where the axle enters the elevation bearing. Here the surface current levels are 3.7 dB higher for the straps connected over the bearing than for the straps connected below the bearing.

No difference could be observed between scenarios for the electric field results. With no contribution to the recommendations given, these results were omitted.

With the plane-wave excitation, the surface current density levels were highest when the plane wave is directly from the side of the model. When comparing the case for the straps over versus the straps below the axle, the results in Fig. 6.18 and Fig. 6.19 show that the levels on the bearing and axle mounting differ by no more than 0.7 dB. However,

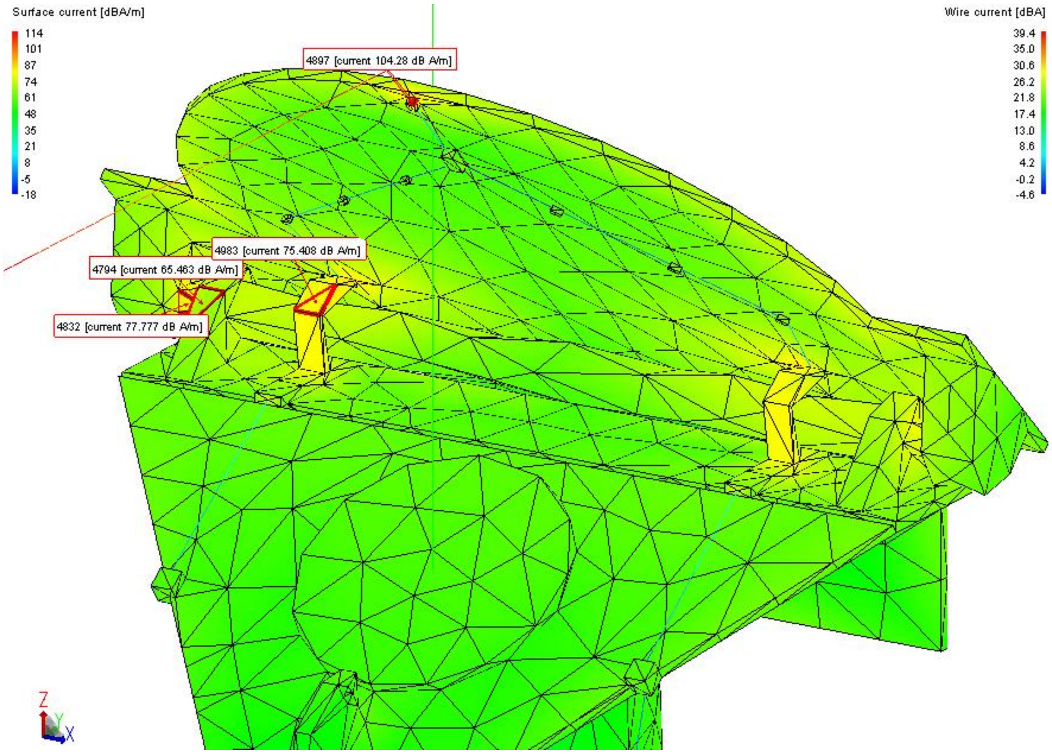

Figure 6.16: *Surface current density results for a direct current injection. The dish is angled at 45 degrees and the straps connected over the elevation bearing axle.*

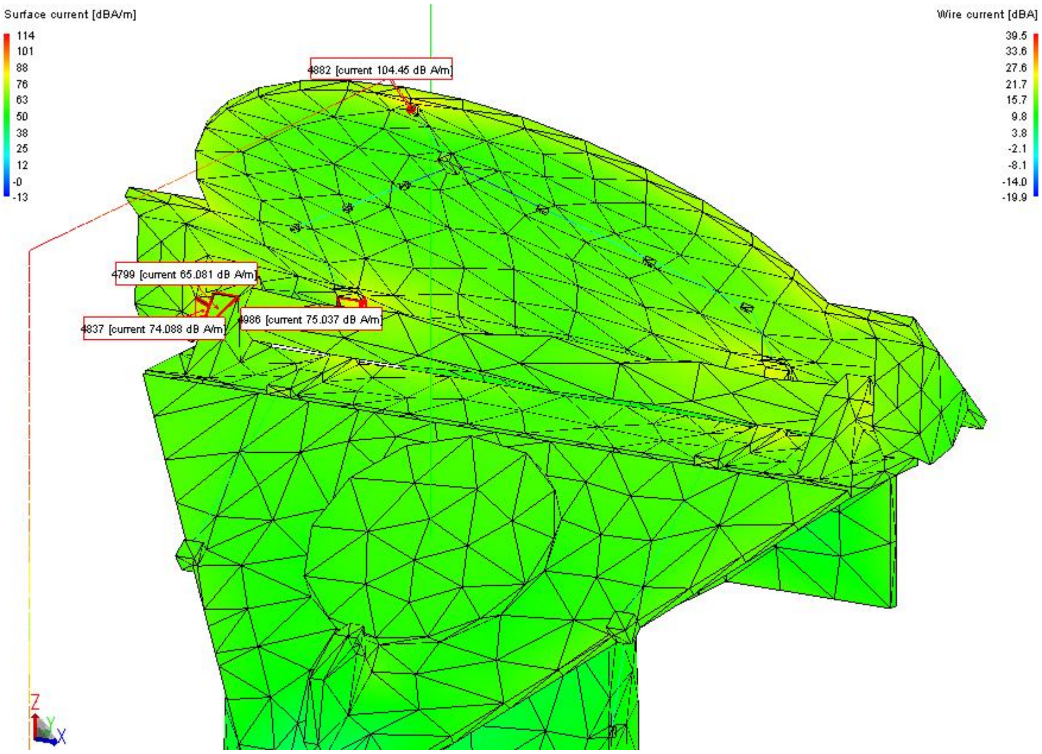

Figure 6.17: *Surface current density results for a direct current injection. The dish is angled at 45 degrees and the straps connected beneath the elevation bearing axle.*

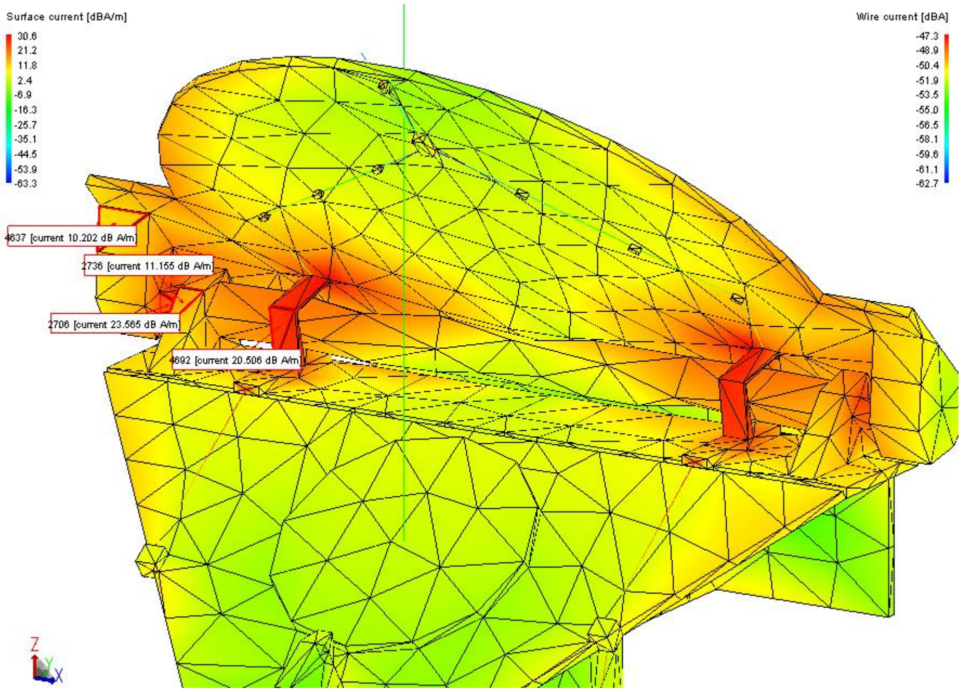

Figure 6.18: *Surface current density results for a plane-wave excitation from the side. The dish is angled at 45 degrees and the straps connected over the elevation bearing axle.*

the current density for the strap going beneath the axle is 3 dB higher than the value on the axle connection to the bearing. For the strap going over, the axle connection value is 3 dB higher compared to the strap's value.

These results indicates that the strap going below the axle has a better protection characteristic compared to the strap going over when the dish is angled at 45 degrees.

Considering the dish at an angle of 90 degrees to the vertical, the surface current density results are given in Fig. 6.20 and Fig. 6.21. From the figures it can be seen that all of the levels in the strap going over the axle are between 2 dB and 3 dB lower than the case with the straps going below. From inspection, it was found that the current injection level for the latter case is 2.3 dB higher, indicating that the comparative levels agree to within 1 dB.

The plane-wave excitation results follow in Fig. 6.22 and Fig. 6.23. For this case, all the levels are between 1 dB and 2 dB higher for the straps going over the bearing axle compared to the straps connected below.

The simulations were repeated with the surfaces coated as mentioned in section 6.4. The coating of paint was modelled with a 2 mm air gap, which relates to a 100 micron space. The current density results of Fig. 6.24 show that the results are still in agreement with the values obtained without the coated surfaces.

The final recommendation given to the KAT-7 design team was that the level of protection is better for the case where the LDC straps are connected below the elevation

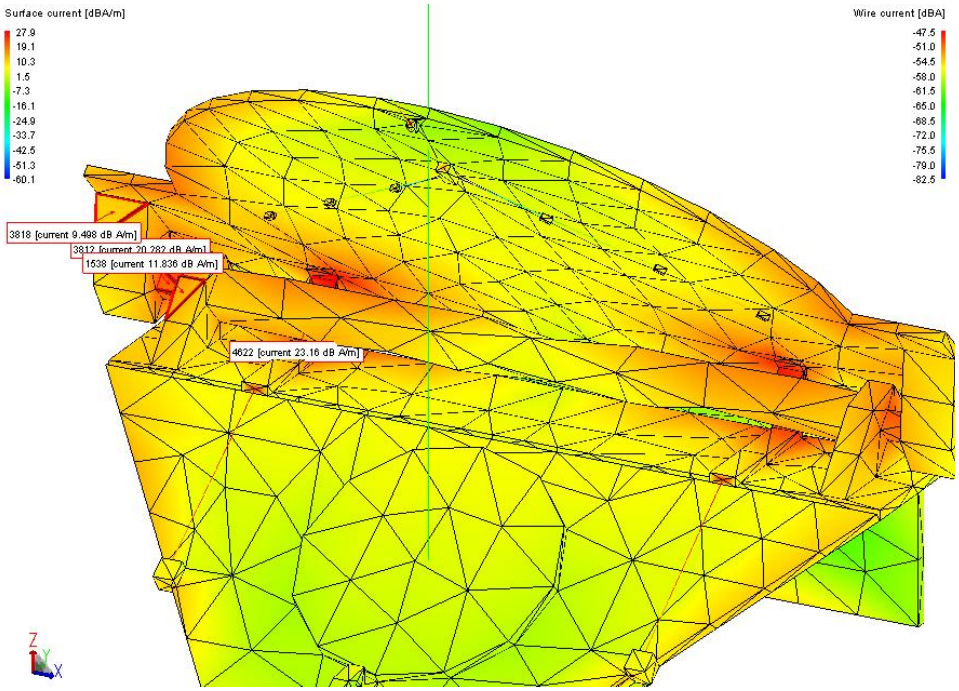

Figure 6.19: *Surface current density results for a plane-wave excitation from the side. The dish is angled at 45 degrees and the straps connected beneath the elevation bearing axle.*

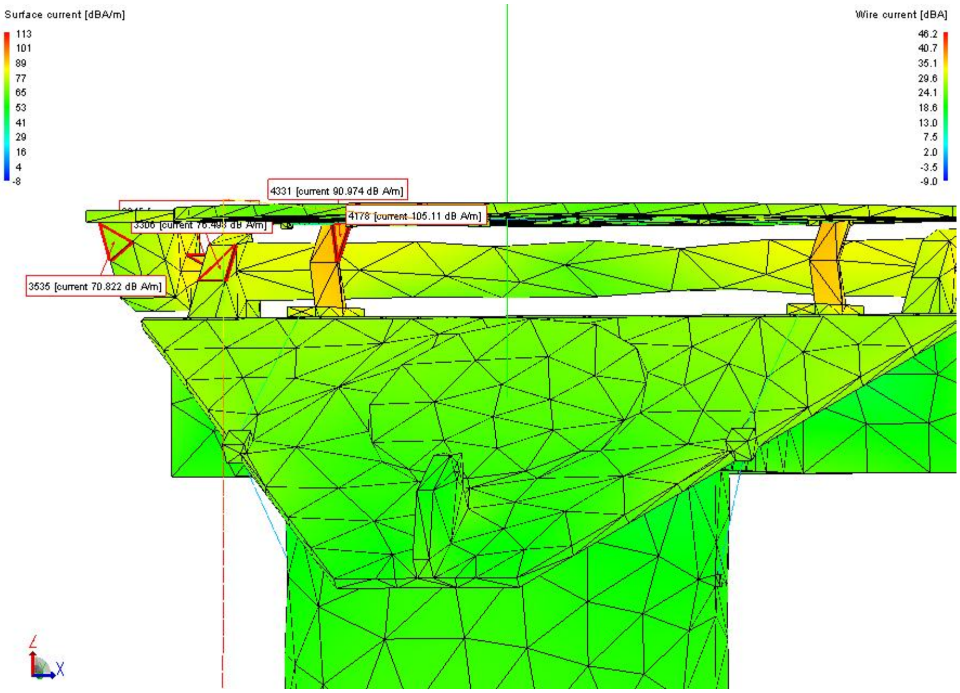

Figure 6.20: *Surface current density results for a direct current injection. The dish is angled at 90 degrees and the straps connected over the elevation bearing axle.*

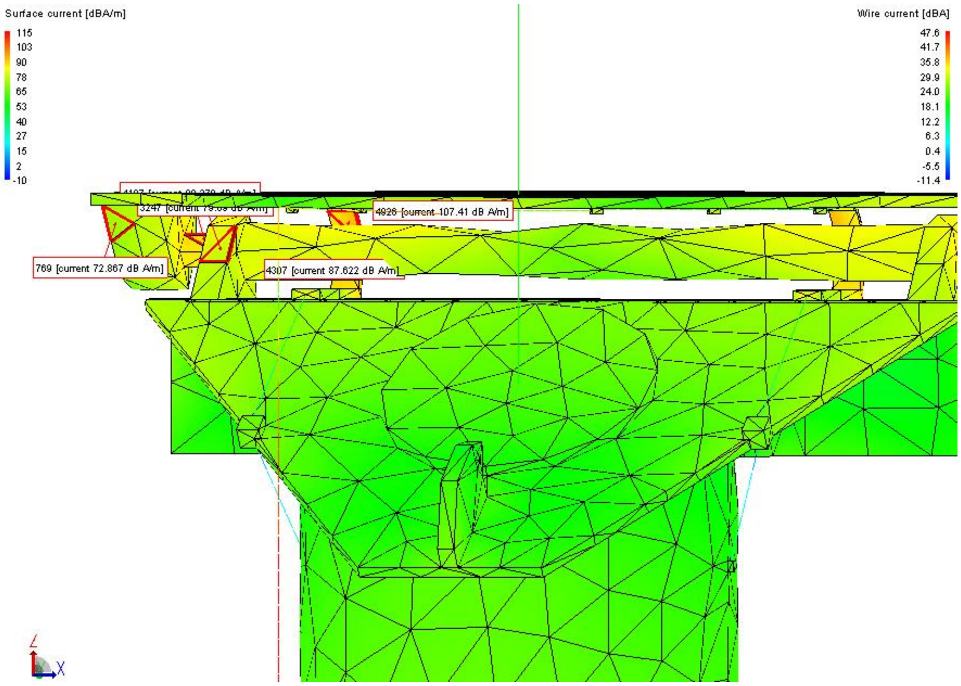

Figure 6.21: *Surface current density results for a direct current injection. The dish is angled at 90 degrees and the straps connected beneath the elevation bearing axle.*

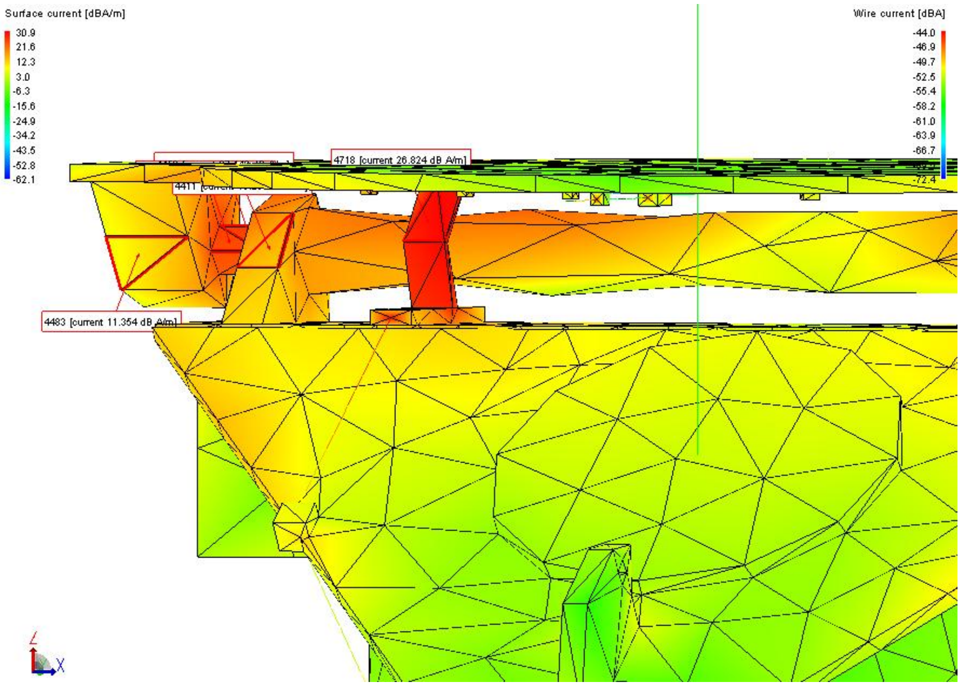

Figure 6.22: *Surface current density results for a plane-wave excitation from the side. The dish is angled at 90 degrees and the straps connected over the elevation bearing axle.*

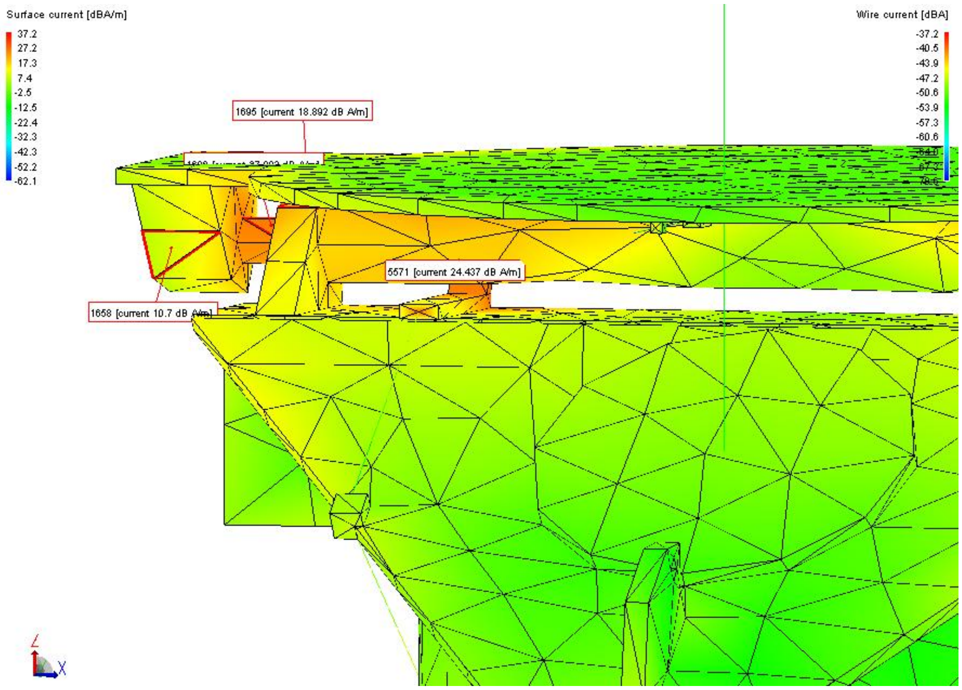

Figure 6.23: *Surface current density results for a plane-wave excitation from the side. The dish is angled at 90 degrees and the straps connected beneath the elevation bearing axle.*

bearing axle. This implies a lower cost for the shorter straps needed for this application. The recommendation was implemented on the KAT-7 structures.

6.4.4 Results for LDC Over Azimuth Bearing

Four models evaluating different scenarios of connection over the azimuth bearings, are shown in Fig. 6.25. Each model has a different amount of copper shoe connections over the bearing and a different amount of conductors coming from the elevation bearings to the steel ring which connects to the shoes.

With the assumption that all steel elements of the structure was galvanically connected, the surface current density for these four scenarios were modelled in FEKO. The results showed that the levels of current density did not change much between the different cases. One of the results, for the four shoes connected and no conductors, is shown in Fig. 6.26. Here the only change between scenarios is that the bearing elements directly behind the shoes have lower current density levels than when there are no shoes connected. The electric field levels inside were the same for the different scenarios.

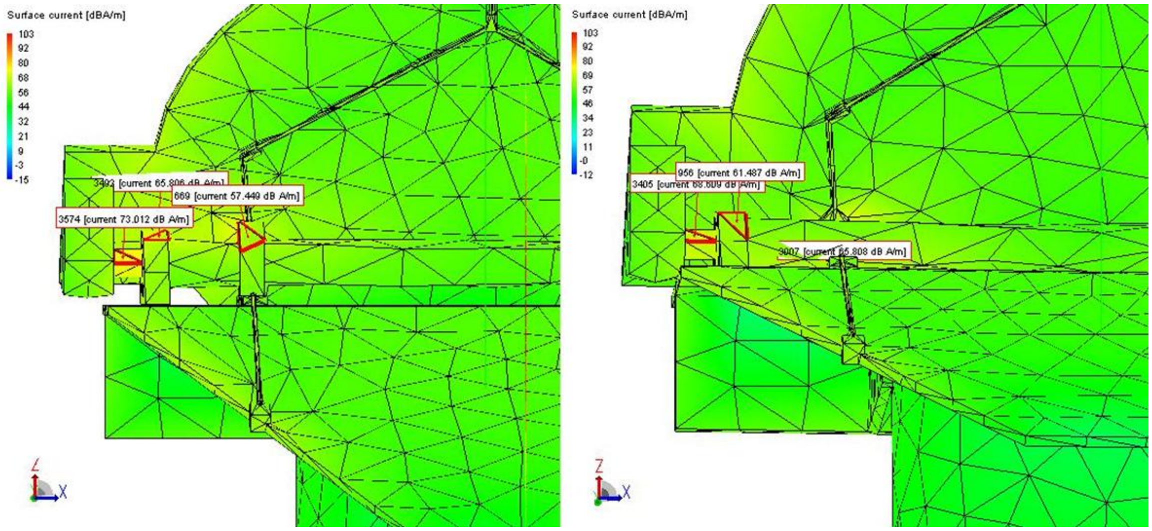

Figure 6.24: *Simulations repeated with coated surfaces for the dish at 45 degrees. The first picture shows current density results for the straps over the bearings and the following picture for the straps below.*

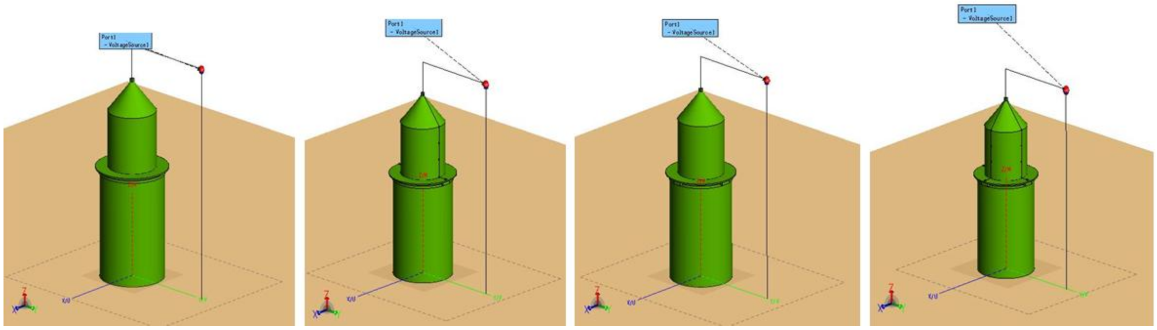

Figure 6.25: *Different scenarios for connection of the LDC copper shoes over the azimuth bearing. F.l.t.r. No conductors or shoes connected; Two conductors and two shoes connected; Four shoes connected, but no conductors, thus the steel of the yoke and pedestal is used for the LDC; Four conductors and four shoes connected.*

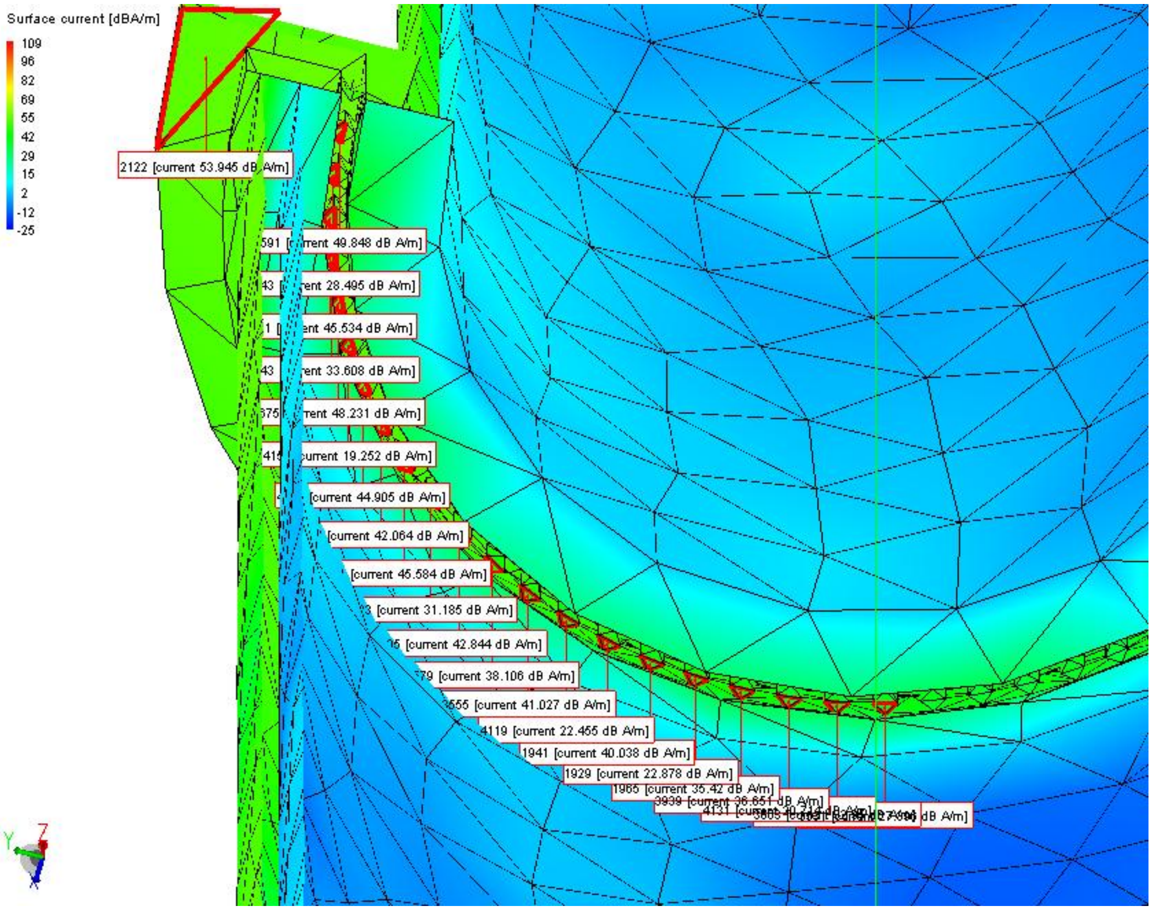

Figure 6.26: *Surface current density on the bearing elements for four shoes connected over the bearing, as seen from below and from inside the structure.*

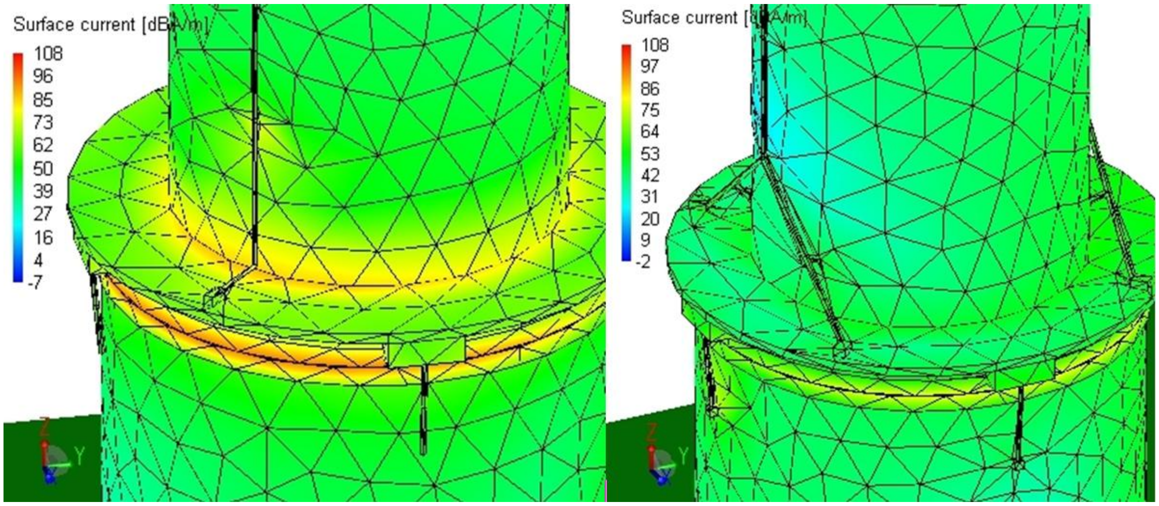

Figure 6.27: *Original design over the azimuth bearing on the left, showing high current density at the coated interfaces due to capacitive coupling. The altered design on the right shows noticeably lower current density at key interfaces compared to the previous figure.*

6.4.5 Coated Interfaces and Corrective Bonding

As mentioned in section 6.4, all the element surfaces were coated for corrosion protection. The bearing itself was gun-coated and the pedestal and yoke structures were painted. From this it became apparent that even the bolts connecting these elements would only contact the painted surfaces, and not make galvanic connection. To ensure that all possible practical conditions were included in the modelling, it was elected to repeat the modelling with the coated surfaces.

At the interfaces between the yoke, bearing and pedestal, the areas are fairly large and the distance between the elements very small. With the painted or gun-coated surface, this creates a capacitor. At high frequency, capacitive coupling takes place at these interfaces, introducing surface currents to the inside of the structure. The worst case surface current density for the original design is shown in the first picture of Fig. 6.27. The high levels of coupling can be seen here if the elements are not galvanically connected.

Alterations to the design was discussed with the design team, as this layout was discovered to show the worst coupling levels. The yoke and pedestal had, however, already been manufactured, and the fittings for the LDC connections were already installed. The only alternative was to investigate a design which could be retrofitted still using the installed fittings.

Lower coupling levels were seen with more conductors used concentrically around the yoke and the pedestal. The design was changed to let the two down conductors split into four terminations onto the steel ring. Bonding of the copper shoes onto the bearing had to ensure galvanic connection, and conductors from the shoes to the pedestal steel was

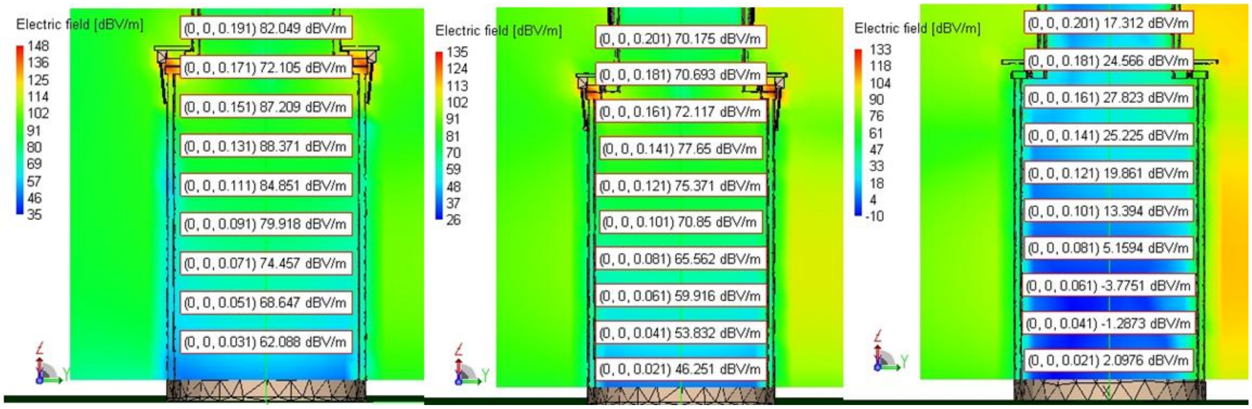

Figure 6.28: *Simulated electric field inside the bottom of the pedestal structure, for three different scenarios, f.l.t.r. Coated interfaces with high electric field levels inside the pedestal; Optimised bonding with decreased electric field levels inside the pedestal; Ideal galvanically connected structure with very low electric field levels inside. The electric field values are shown for points on the z-axis in the middle of the pedestal.*

needed. When these alterations to the design was modelled, we observed that the worst case surface current coupling levels dropped by 12 dB. The decreased current density at the interfaces can clearly be seen in Fig. 6.27. This can be attributed to the more uniform surface current distribution using four connections compared to two connections to the steel plate.

Different levels of E-field coupling to the inside of the structure are shown in Fig. 6.28. The picture on the left shows the electric field levels for the original LDC design. The results for the optimised design E-field is seen in the middle picture, while the picture to the right has the assumed perfect galvanic connection with no LDC connected over the bearing. From the original LDC design, the E-field levels are reduced by 12 dB with the optimised design. However, the ideal galvanically connected structure would have given 30 dB shielding without the need of an LDC. The recommendations were relayed to the KAT-7 design office and the changes will be implemented on one of the KAT-7 structures.

The FEKO modelling aided in designing corrective bonding placement for improved lightning protection, and minimal induction to the interior of the structure.

6.5 RFI Resonances

Where discontinuities in the structure exist, lightning currents may experience reflections in the time domain, due to sudden changes in impedance of the current path [21]. These reflections can be linked to resonances in the frequency domain. A program within FEKO, called AdaptFEKO, uses adaptive frequency sampling to identify sharper resonances within a certain frequency range. More frequency points are then chosen closer to

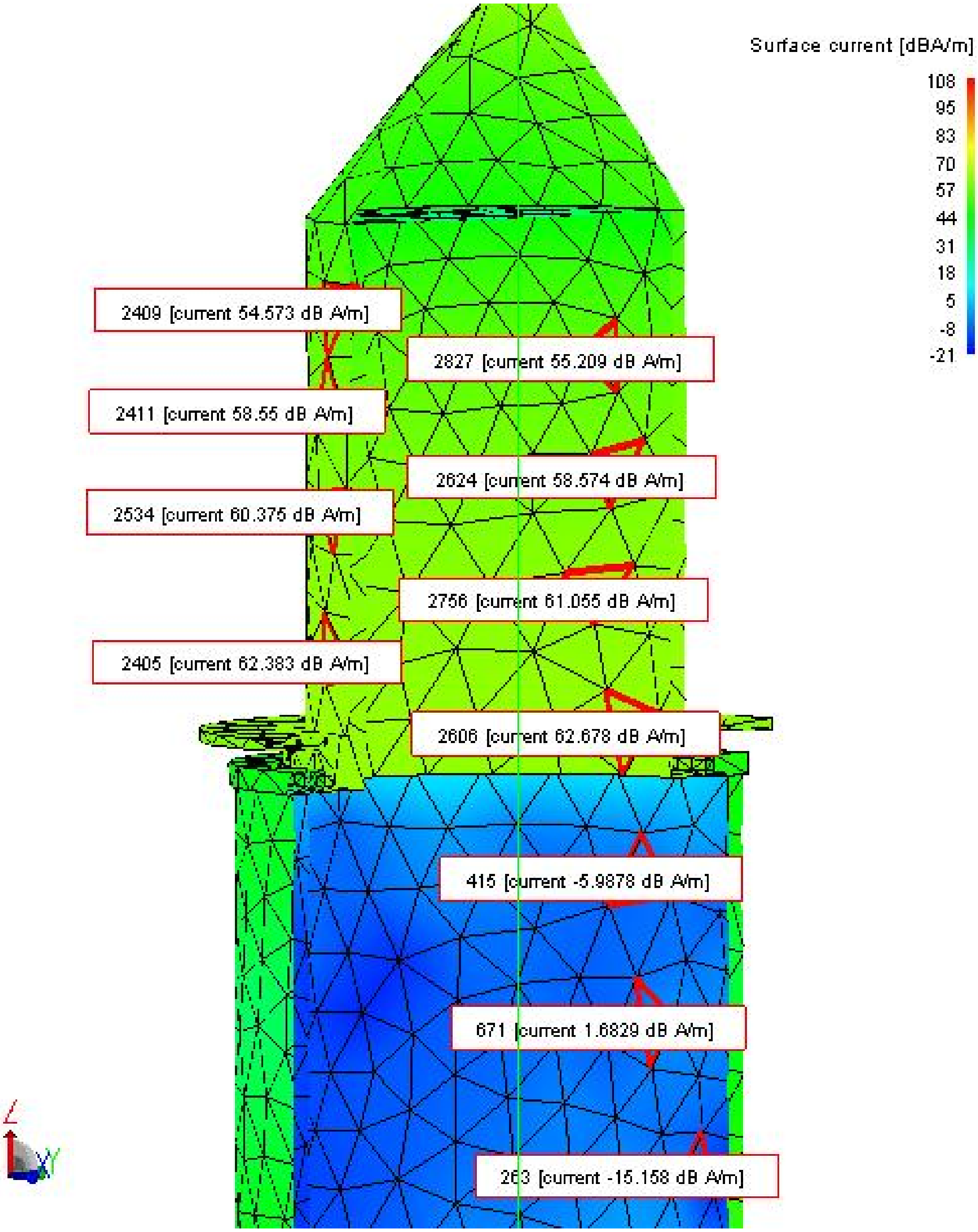

Figure 6.29: *Surface current density results, at 587 MHz, in and outside the pedestal and yoke, for the azimuth bearing galvanically connected.*

the resonances and less points where the curve is relatively smooth. This helps to ensure that very sharp resonances are not missed when choosing the amount of frequency points for a wide frequency range. The code chooses the frequency points at which resonances occur to calculate the current density and the EM field.

A frequency range with 21 frequency points between 20 MHz and 1 GHz was used to investigate areas which require RFI mitigation due to possible reflections. This corresponds to a real frequency range of 1 MHz to 50 MHz, which includes the higher frequency lightning content. Although the highest concentration of energy for the lightning current lies around 25 kHz, the main lightning protection is being dealt with by the contractors.

The result for one of these investigations is shown in Fig. 6.29 for the pedestal, yoke and azimuth bearing galvanically connected. The only pathway for leakage currents and fields to enter the interior, is in between the bearing roller elements. At 587.368 MHz, a resonance is apparent on the inside of the yoke, where surface current density inside is equivalent to that on the outside of the yoke. Surface currents inside the pedestal, however, are at levels of 60 dB to 65 dB less than the outside.

When considering the scaled dimensions of the model yoke interior, it was discovered that the height of 102 mm from the bearing to the ceiling corresponds directly to the wavelength of the 5^{th} harmonic of 587.368 MHz. The harmonic frequency scales in real terms to 146.8 MHz. This is close to a frequency range of 150 MHz to 153 MHz, which is used as one of the operational bands for pulsar detection. If the design dimensions were slightly different, lightning induced reflections inside the structure could interfere with observed radio signals from pulsars.

From these results it is seen that resonances inside the structure can assist the identification of areas requiring RFI mitigation at sensitive frequencies. By investigating resonant frequencies on accurate scale models in FEKO, including all interfaces and equipment, recommendations on future design parameters for the placement of shields and cabinets inside the structure can be given to MeerKAT to effectively mitigate lightning interference.

As a final comment on this analysis, some resonant frequencies are dependent on particular cable lengths and layout. In practice, variations between pedestal cable and cabinet configurations can lead to quite different characteristics. Specific investigations are thus not always profitable. Rather, a design team should be alert to the possibility of structural resonances, and take care to keep these out of sensitive bands.

6.6 Earthing Investigations

From the IEC standards on lightning protection [9], the requirement is given that the LPS should utilise the metal elements of the structure in the design. The requirement for steel reinforcing in concrete, is that the interconnection of the metal elements should be continuous, thus the elements should either be welded or securely connected.

In the first picture of Fig. 6.30 the foundation excavations is shown in the photograph, with the steel reinforcing to be used in the background. The second picture gives a closer view of the steel reinforcing for one of the structure foundations, and the last picture illustrates full welding of all the elements of the reinforcing.

To follow the standard requirement, earthing was done via eight copper rods in the bottom of the foundation excavation. Four rods are placed one at each corner, and the other four are placed in between them on the sides. All of the rods are interconnected with a copper ring conductor using exo-thermic welding. An early design sketch is seen as the first picture in Fig. 6.31. The earthing is connected onto a ring that forms part of the pedestal foundation bolts (second picture). The connection is shown in the third picture as a bolted lug connection onto the ring. The last picture of the figure illustrates one of the exo-welded joints of the earth electrode conductors.

The design team opted to implement different earthing strategies on some of the KAT-7 structures. Three of the structure's foundation steel reinforcing was welded together to ensure proper continuity of the steel. The labour-intensive welding process took three full work days to complete per structure. The building of the full KAT-7 structure takes about 2 weeks, so this seemed a disproportionate amount of time devoted to the foundation. The KAT-7 building team expressed concern about the time and cost implications.

Another interconnection method that was implemented on one structure, was to connect the steel elements with binding wires (5 % was welded for stability only), and a third method had only 20 % of interconnections welded. Soil resistivity surveys and earth resistance tests were done on all seven foundation's earthing. The earth resistance tests were initially carried out with just the copper earth wires and rods installed in the foundation excavation. Afterwards, the tests were repeated when the foundation reinforcing

Figure 6.30: *Photographs f.l.t.r. The foundation excavation for one of the KAT-7 antennas with the steel reinforcing to be used in the background; The steel reinforcing for one of the structure foundations; Welding of foundation steel reinforcing elements to improve resistance to earth.*

Figure 6.31: *F.l.t.r Early design sketch of the earth electrode layout; The pedestal mounting foundation bolts connected to the reinforcing; Earth electrode connected to the foundation ring with a bolted lug; Exo-thermic welding connection for the earth electrode conductors.*

was connected and the concrete poured.

The requirement from the standards [9] states that the resistance to earth of the earth electrode system be below 10 Ω for effective lightning protection. For two of the structures with reinforcing steel elements welded, the earth resistance was measured as 26.4 Ω and 28.2 Ω before, and 9.21 Ω and 7.71 Ω after the concrete was poured. The improvement in earth resistance by adding the steel reinforced concrete with welded interconnections of steel elements, was therefore 17.2 Ω and 20.5 Ω respectively.

The foundation using binding wires had values of 33.4 Ω and 9.38 Ω, indicating an improvement of 24 Ω. Where the reinforcing was only 20 % welded, the resistance to earth was decreased by 12.4 Ω to 6.88 Ω. It was found that the addition of the steel elements to the earth electrode system lowered the earth resistance by between 12 and 24 Ω. The interconnection with binding wires showed the best improvement in earth resistance.

If it could be proved that the welded interconnection of the steel elements is not essential for the earth electrode system, it would save both time and cost to the project, eliminating the labour-intensive process of welding all the steel elements of the reinforcing.

6.6.1 Numerical Modelling of Earthing and Bonding

The simplified scale model used in section 6.4.2 is employed to investigate earthing and bonding. At the base of the pedestal, only four of the foundation bolts are galvanically connected to the pedestal steel for the LDC. Although all thirty-two bolts go into the foundation and are connected to the two foundation rings, only the four relevant bolts are modelled. The steel reinforcing is included as a grid of fifteen by fifteen wires, connected below ground level to the first foundation ring. A similar grid is formed at the bottom of the concrete foundation, and both grids are connected with fourteen vertical wires on each side. A ring conductor at a level halfway in between the two grids, is represented by

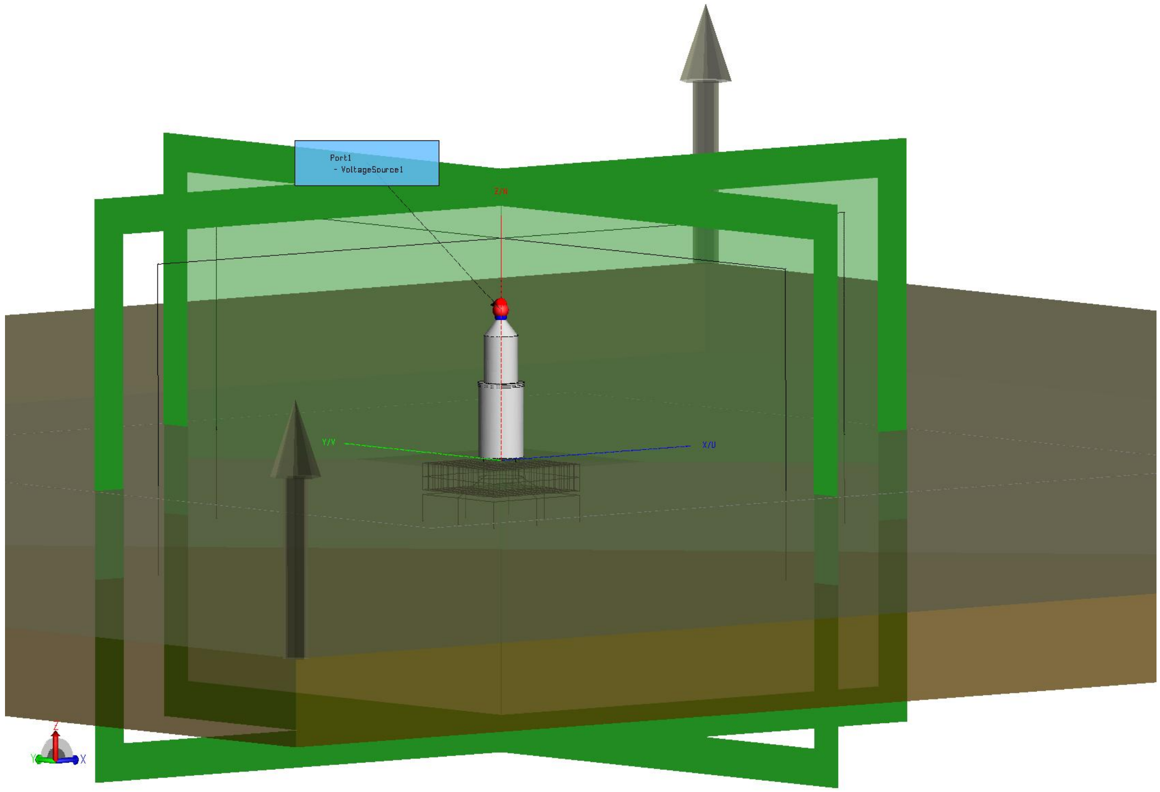

Figure 6.32: *FEKO simulation of the simplified pedestal and steel reinforcing connected to the earthing. An infinite Sommerfeld ground plane simulates the soil interface. The interface at the bottom of the soil is set up as a PEC ground plane. Symmetry is used to reduce computation time, seen as two green rectangles. A current injection is modelled with four concentric conductors, connected from the PEC earth below the soil. They combine above the model to connect to a discrete voltage port with fixed current value, which is used to simulate a direct lightning strike.*

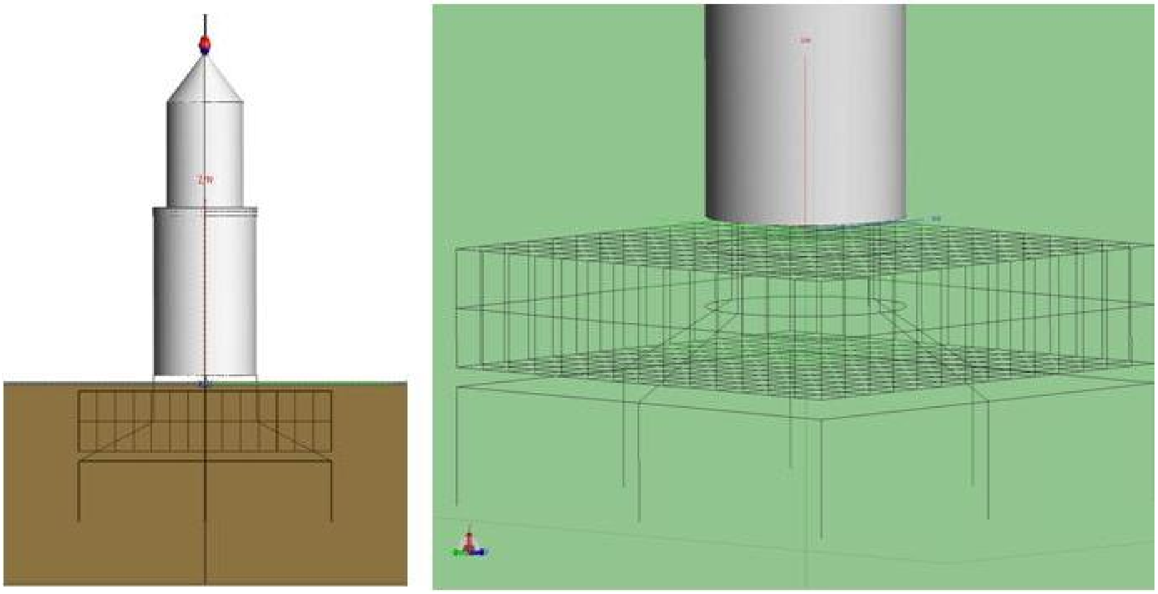

Figure 6.33: *The picture on the left gives a side view of the model with the reinforcing and earth. The only current return path is formed by the earthing conductors via the soil to the PEC ground plane; The picture on the right shows how the earthing conductors are connected to the pedestal foundation ring in the middle of the steel reinforcing. Different interconnections of the elements and earthing are investigated.*

a wire that connects the vertical wires on all sides.

Eight vertical wires below the foundation are interconnected by a ring wire that forms the earthing copper rods and ring conductor. Four wires connect the earthing ring on each side to the bottom foundation ring inside the foundation grid.

Earth is simulated by a Sommerfeld integral ground plane which has dielectric material representing the soil and a PEC ground plane beneath it. The material is defined with the same assumed conductivity for both soil and concrete, scaled and converted from 100 Ωm to 0.2 S/m. From [32, 48], an accepted value for the relative permittivity of soil is given as $\epsilon = 10$. To simplify the model, the area below the pedestal which allows cable entry is left out of the model, forming a homogeneous area below the air-soil interface.

The bottom of the simulated soil forms a PEC ground plane. The discrete voltage port, which forms the current injection for a simulated direct lightning strike, is connected to this PEC ground plane via four wires. These wires run parallel to the ground plane to the extent of the model, and then bend down to connect to this ground plane (see the picture in Fig. 6.32). This forms the return path for the current injection from the voltage port. Current values on the wires can then be compared for the different scenarios.

For the interconnected scenario, all of the wires are connected at each intersection. The right-hand side picture of Fig. 6.33 shows all the interconnected reinforcing steel elements, as well as the earthing rods and ring below it. The diagonal wires connecting

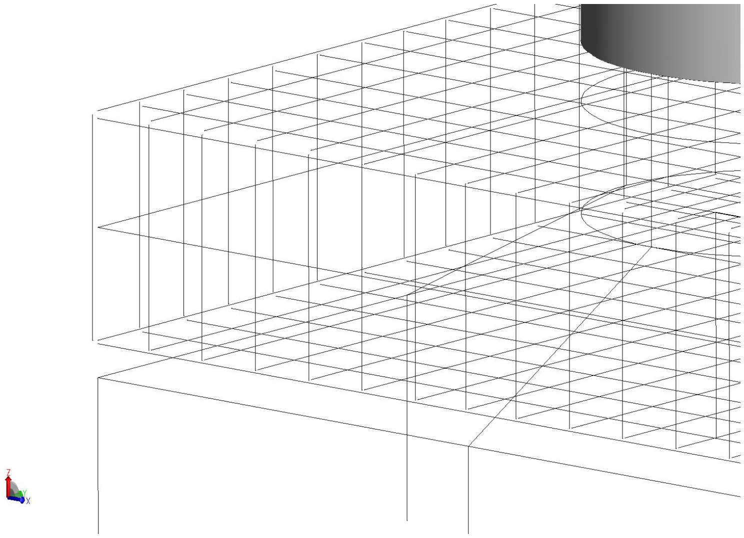

Figure 6.34: *Steel reinforcing elements not interconnected to investigate the effect on earthing.*

the foundation ring to the earthing ring are connected to the bottom steel grid as well.

In Fig. 6.34, none of the reinforcing elements are interconnected, neither are they connected to the earthing ring or rods. This is achieved by translating the elements by 2 mm in different directions in the model, thereby being in close proximity in the concrete, but not galvanically connected. The only connections made are the elements that cross the top foundation ring, which are connected to that ring and each other, and the diagonal earth wires connecting the foundation ring to the earth ring.

The two models are meshed in FEKO to each form 1160 triangles and 2720 segments. Geometrical symmetry is used in two planes to increase the computational speed. For the 1 GHz frequency considered, the simulations took less than three hours each to run on a four-core machine.

6.6.2 Modelling Results

The foundation reinforcing element current results, for interconnection versus no interconnection of steel reinforcing, can be seen in Fig. 6.35 and Fig. 6.36. The same results for the copper earthing elements of the earth electrode system are shown in Fig. 6.37 and Fig. 6.38.

When the currents on the steel reinforcing for the two scenarios are compared, the elements at the top of the reinforcing show less than 2 dB variation in value. However, the results on the lower elements of the concrete reinforcing show that the interconnected scenario (where the earthing and lower grid is connected as well) has higher currents flowing. Where the elements are not interconnected, the lowest current result is 9 dB

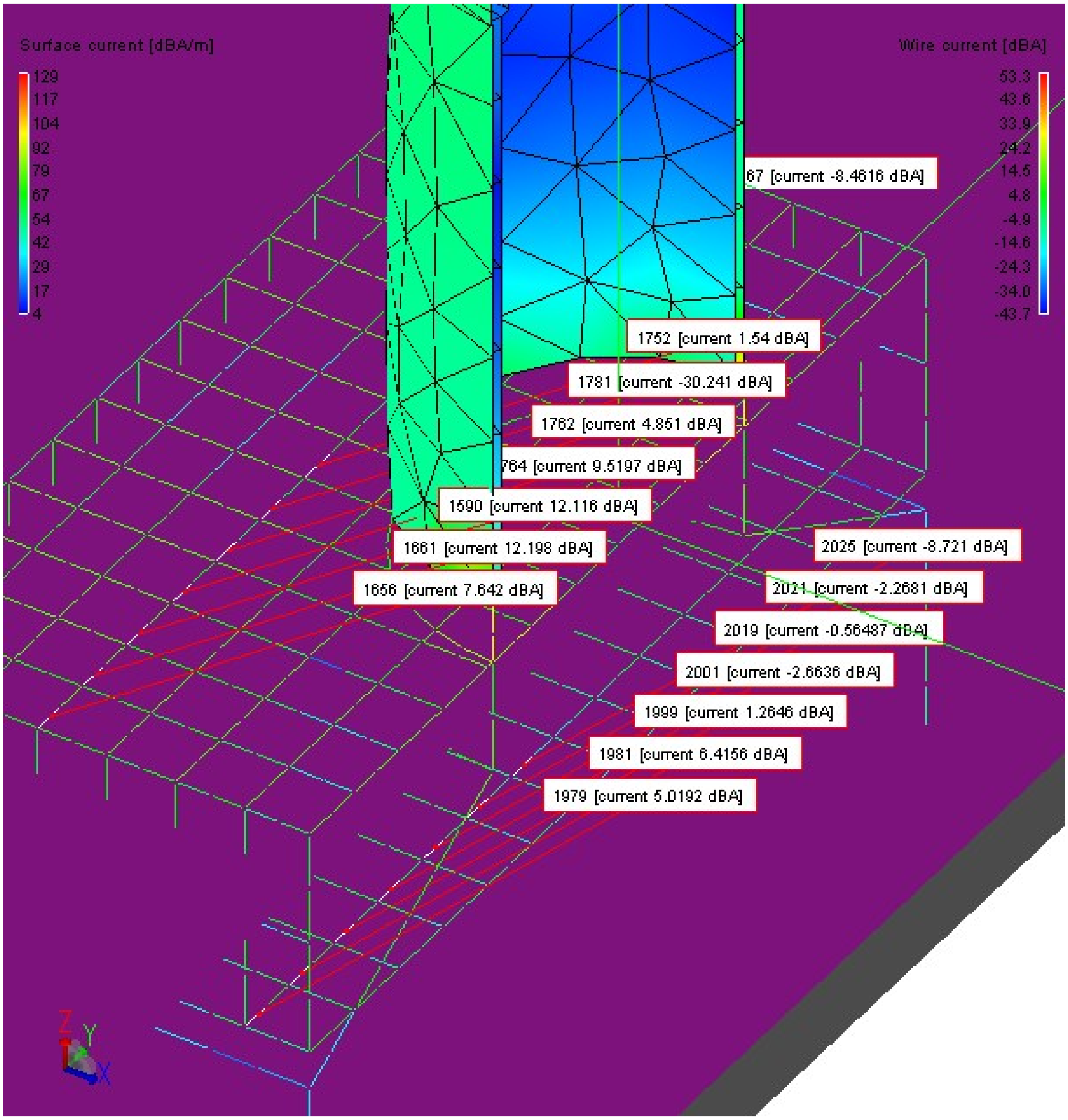

Figure 6.35: *Wire current and surface current density results from FEKO 1 GHz simulation for steel reinforcing rods interconnected.*

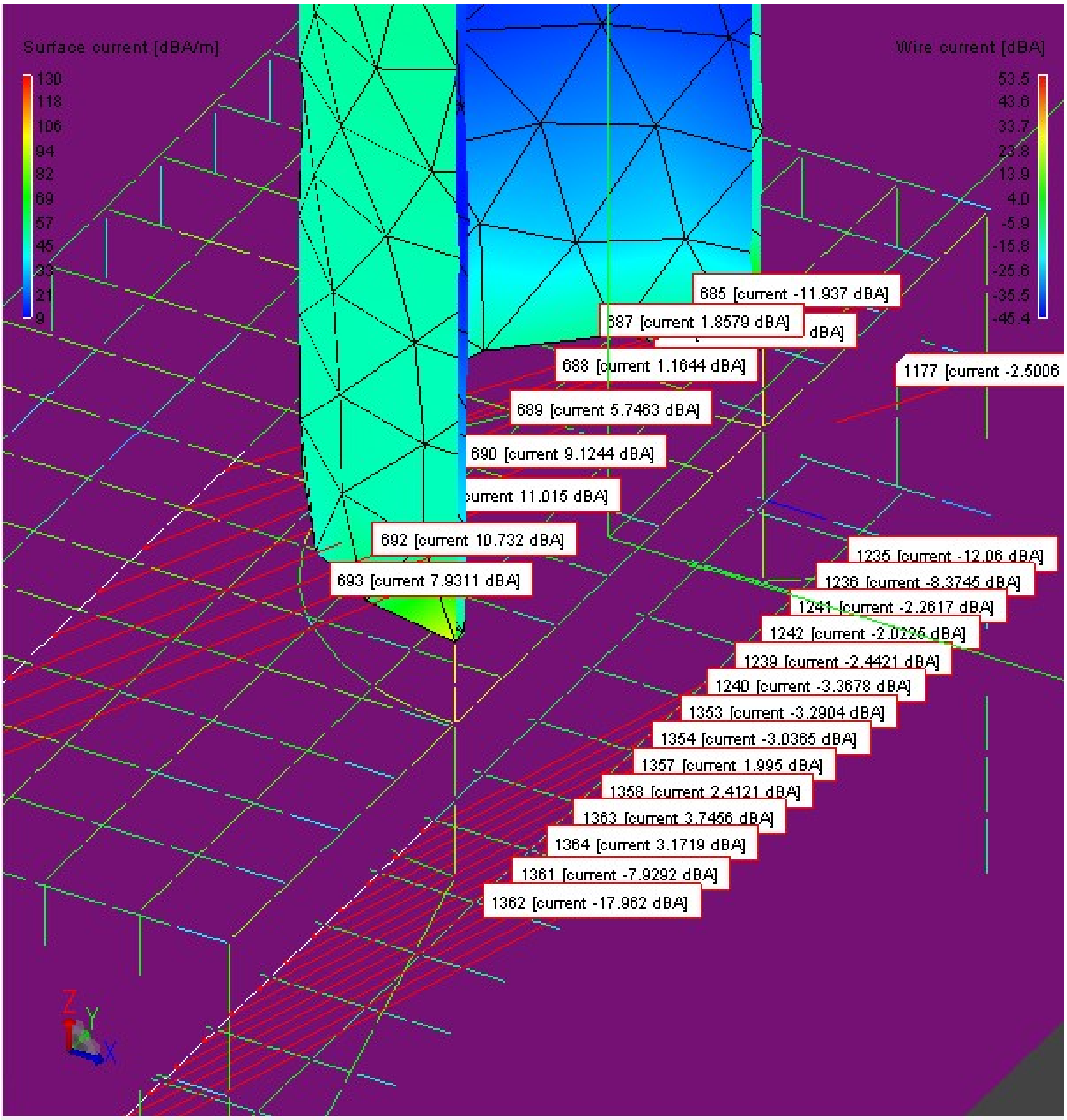

Figure 6.36: *Wire current and surface current density results from FEKO 1 GHz simulation for steel reinforcing rods not interconnected.*

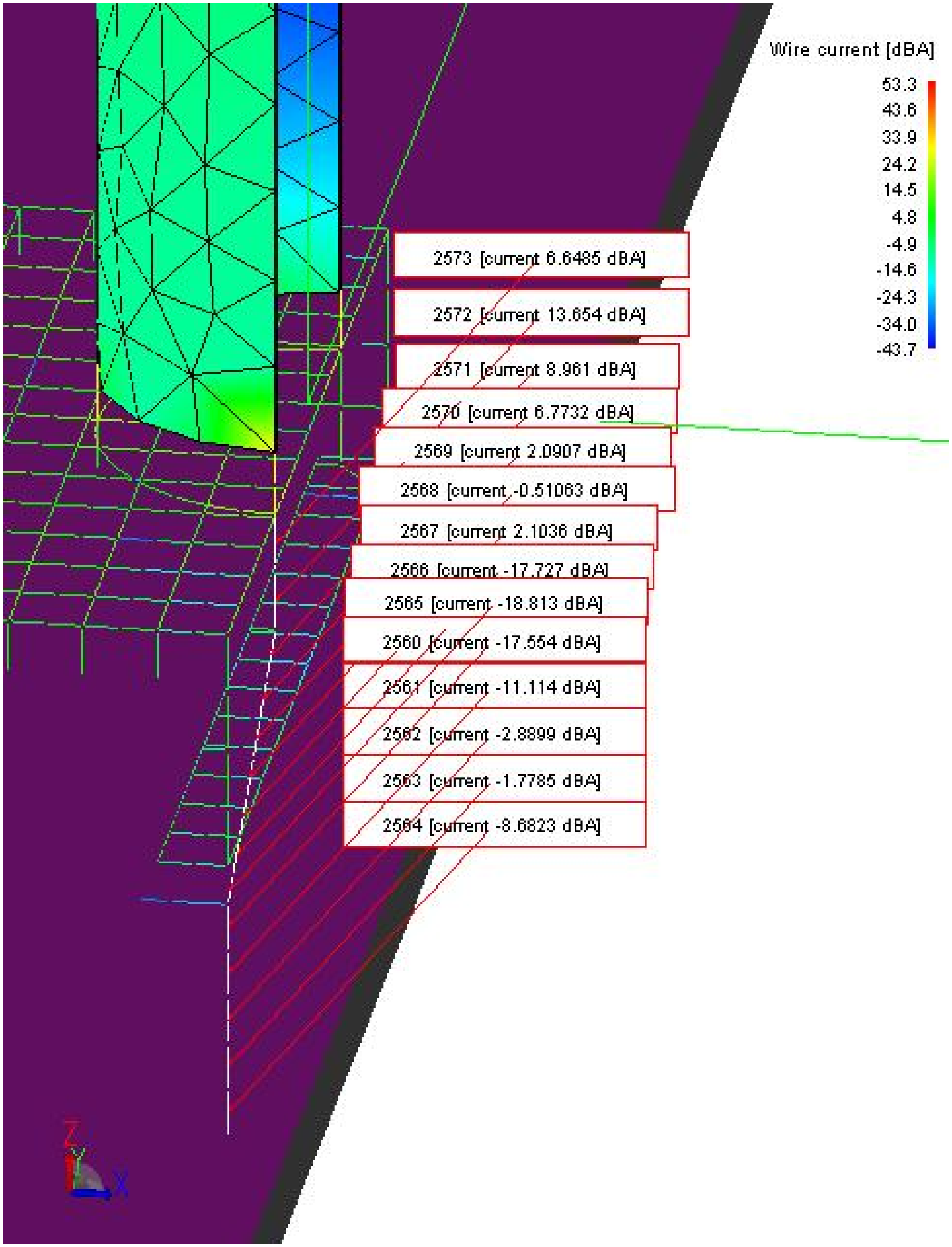

Figure 6.37: *Wire current results from FEKO 1 GHz simulation for steel reinforcing rods interconnected.*

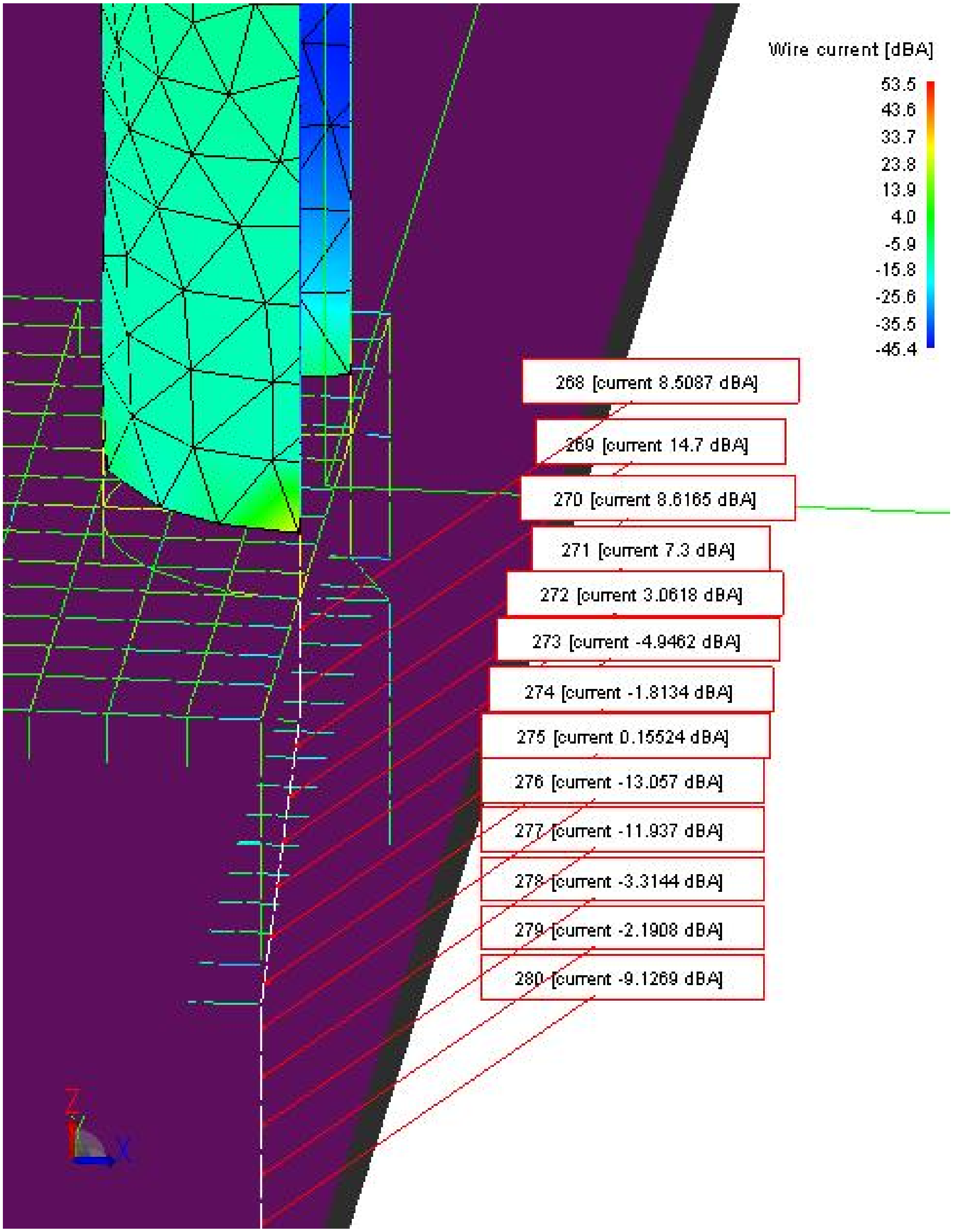

Figure 6.38: *Wire current results from FEKO 1 GHz simulation for steel reinforcing rods not interconnected.*

lower than the lowest value for interconnected elements.

Considering the copper earthing elements for the different scenarios, the results in Fig. 6.37 and Fig. 6.38 differ no more than 3 dB, except for three wire segments. The largest variation on these segments of the copper wire, is seen where it is connected to the lower grid steel reinforcing in the interconnected case. Here the current levels are 17 dB lower than the levels for the copper wire that is not connected.

These results indicate that the interconnection of the steel reinforcing does not affect the earthing greatly. However, the connections between the earthing electrode and the foundation steel rings and reinforcing elements do show changes in current levels. After discussion with the infrastructure team of KAT-7, we found that the foundation ring onto which the earth rods are connected, is painted as well.

At higher frequencies, such as the scaled 50 MHz used for simulation, capacitive coupling would aid the conduction of current to earth through this connection. However, if proper galvanic connection is not made, the main lightning current components at 25 kHz and 1 MHz may prefer the reinforcing elements as the lowest impedance path to earth. This could cause cracking of the concrete and damage to the foundation when lightning strikes. For this reason, some countries forbid the use of concrete steel reinforcing as part of the earth electrode [9].

To conform to South African standards, which are in line with IEC standards [9, 16, 18, 19], using binding wires to connect the steel reinforcing elements would be sufficient, seeing that it has the best improvement in earth resistance as well. High frequency simulations show that the interconnection of the steel elements do not contribute largely to the flow of current, except where connections are made to the copper earth electrodes. However, with practical considerations of corrosion protection inside the concrete [9, 57], these connections need closer scrutiny for the MeerKAT design.

6.7 Conclusions

The verified CEM models are used for investigations into RFI characterisation for maximum lightning protection. Different excitation methods for equivalent direct and indirect lightning strikes are evaluated and a direct injection method is found to be valid under certain conditions. However, an improvement on the current injection method is to not take it from one side only, but have the excitation wire connected to ground on four different sides to lessen the magnetic field influence.

The modelling is used to study various different design options for the LDC layout and bonding over the bearings. To consider the RFI implications of the design as well, surface current density and electric fields are calculated in FEKO at the highest probable lightning frequency of 1 GHz, which scales in real terms to 50 MHz. The results are used to compare the lightning current and RFI behaviour for the different cases and determine the optimal design layout regarding cost-effectiveness, lightning protection and RFI mitigation.

The function AdaptFEKO is used to show that resonances can identify areas requiring RFI mitigation inside the structure. This can help the future MeerKAT design to ensure that the dimensions of shielded enclosures inside the structure do not cause lightning induced reflections at frequencies sensitive to radio astronomy observations.

Using a Sommerfeld integral ground plane with soil and concrete below, the FEKO simulations have shown that welding the steel reinforcement elements of the concrete foundation does not affect the currents flowing in earth sufficiently to substantiate the time and cost, compared to using binding wire to interconnect all the steel elements. However, the earthing rods and bonding ring play an important role, and the connection of this earthing system to the pedestal foundation bolts is a more relevant matter requiring attention. Feedback pertaining to the earthing issues at hand were given to the SA SKA team to consider when planning the design for MeerKAT.

Continuous feedback has been given to the KAT design team on an active international project. FEKO has played an important role in these investigations.

– The most important thing is to not stop questioning –

– Albert Einstein –

Chapter 7

Conclusions and Recommendations

This dissertation has presented original design contributions regarding lightning protection and RFI mitigation for South Africa's intended demonstrator for the world's largest radio astronomy project, the SKA. These contributions have been tested using the computational electromagnetic code, FEKO. This approach has been validated through extensive checking of physical and computational scale models.

Two methods of lightning excitation were used in the investigations. An equivalent current injection method simulated direct lightning strikes. The connection of the current injection was brought into question at an URSI conference, but ITU recommendations give conditions for which it is valid. However, an improvement on the method is to not take the injection from one side only, but establish the ground connection from four concentric sides to minimise the effects of the electromagnetic fields produced by the injection current.

The design for the lightning down conductor system for KAT-7 was enhanced by strapping beneath the elevation bearings' axle, and copper shoe connections with optimal bonding over the pedestal azimuth bearings. Coated surfaces and static-bearing roller elements are taken into account for the modelling, having significant influence on the results. Worst case levels of induced RFI into the pedestal are compared, to evaluate the primary areas requiring RFI mitigation in the design. Using AdaptFEKO, structure resonances identify RFI sensitive areas for specific frequencies. The entire lightning down conductor (LDC) design keeps cost-effectiveness as a design constraint.

Project cost and time are saved by evaluating the method of interconnection of the foundation reinforcing as part of the lightning earthing system. This eliminated the need for welding all metallic elements of the reinforcing, which can take up to 3 days per structure. The findings were achieved with MoM code combined with a Sommerfeld integral ground plane and simulated soil below.

The principles and recommendations of this dissertation will be applied in the design of MeerKAT as well. Further recommendations toward this goal would include the following:

Figure 7.1: *Photograph of the first KAT-7 dish being installed in the Karoo during July 2009 [1].*

- Investigate the option of surface coatings only after galvanic connection of conductive elements have been established. The life cycle costing of the corrosion protection against lightning protection should be established to determine a final decision.
- Accurate numerical simulation of the inside of the pedestal should be done with the inclusion of all equipment cabinets. Evaluating resonant frequencies for this enclosure will identify possible induction problems due to lightning. The layout and design of shielding plates or grids for this enclosure can be studied in FEKO to minimise RFI toward the inside of the structure.
- Instead of utilising the foundation steel reinforcing in the lightning earthing system to lower resistance to earth, rather extend the earthing through additional horizontal or vertical earthing rods and ring conductors. The effectivity can be tested through calculations according to South African National Standards on Earthing and by simulating the layout in FEKO.

With the construction of KAT-7 nearing completion, recommendations that have not yet been actioned due to scheduling constraints, will be implemented on at least one of the structures. A photograph of the first KAT-7 dish being installed during June of 2009 is shown in Fig. 7.1.

– Think like a man of action, act like a man of thought –

– Henry L. Bergson –

Bibliography

[1] South African SKA (Square Kilometre Array), http://www.ska.ac.za/

[2] Square Kilometre Array, the international radio telescope for the 21st century, http://www.skatelescope.org/

[3] R.T. Lord, *RFI and radio astronomy - why the fuss?*, National Research Foundation, MeerKAT (KAT-7 Phase) Technical Report, K0000-2001V1-009 TR, Revision 1, 08 July 2009

[4] P.C.T. van der Laan, A.P.J. van Deursen, "Reliable protection of electronics against lightning", *23rd ICLP, Florence, Italy*, Paper 3.14, Vol. I, pp. 370 − 373, Sept 1996

[5] FEKO, Electromagnetic Software and Systems (EMSS), http://www.feko.info/

[6] A. Piantini, J.M. Janiszewski, A. Borghetti, C.A. Nucci, M. Paolone, "A scale model for the study of the LEMP response of complex power distribution networks", *IEEE Trans.Power Del.*, Vol. 22, No. 1, pp. 710 − 720, Jan 2007

[7] G. Sinclair, "Theory of models of electromagnetic systems", *Proceedings of the I.R.E.*, pp. 1364− 1370 Nov 1948

[8] Computer Simulation Technology (CST), Microwave Studio, http://www.cst.com/

[9] International Electrotechnical Commission, "Protection against lightning, Part 3: Physical damage to structures and life hazard", *IEC 62305-3:2006*, Jan 2006

[10] H.C. Reader, R.H. Geschke, P.S. van der Merwe, Dr. R.G. Urban, P.G. Wiid, D.J. Rossouw, "Issues in EMC metrology and modelling for SKA demonstrator", *2008 URSI General assembly, Commissions A and E: EMC Measurements*, Chicago, USA, August 2008

[11] International Telecommunication Union, Standardization Sector, "Series K: Protection against interference, Protection against LEMP in telecommunication centres", *ITU-T Recommendation K.40*, May 1996

[12] T. Williams, "EMC for Product Designers, Meeting the European Directive", *Newnes*, Third Edition, 2001

[13] T. Williams, K. Armstrong, "EMC for Systems and Installations", *Newnes*, First Edition, 2000

[14] P.A. Chatterton, M.A. Houlden, "EMC, Electromagnetic theory to practical design", *Wiley*, First Edition, 1992

[15] J.J. Goedbloed, "Electromagnetic compatibility", *Prentice Hall*, First English Language Edition, 1992

[16] International Electrotechnical Commission, "Protection against lightning, Part 1: General principles", *IEC 62305-1:2006*, Jan 2006

[17] International Telecommunication Union, Standardization Sector, "Series K: Protection against interference, Risk assessment of damages to telecommunication sites due to lightning discharges", *ITU-T Recommendation K.39*, May 1996

[18] International Electrotechnical Commission, "Protection against lightning, Part 2: Risk management", *IEC 62305-2:2006*, Jan 2006

[19] International Electrotechnical Commission, "Protection against lightning, Part 4: Electrical and electronic systems within structures", *IEC 62305-4:2006*, Jan 2006

[20] Private communications during site visits with the following people: Arnold van Ardenne, Albert-Jan Boonstra, Jan-Pieter de Reijer (Astron), Tim Iken, Andrew Faulkner (Jodrell Bank Observatory), and Tony Brown (Manchester University)

[21] Y. Baba, M. Ishii "Numerical Electromagnetic field analysis of lightning current in tall structures", *IEEE Transactions on Power Delivery*, Vol. 16, No. 2, pp. 324 – 328, Apr 2001

[22] V. Hedge, U. Kumar, "Studies on characteristics of lightning generated currents in an interconnected lightning protection system", *Journal of Electrostatics*, Vol. 67, pp. 590 – 596, 2009

[23] M. Bandinelli, F. Bessi, S. Chiti, M. Infantino, R. Pomponi, "Numerical Modeling for LEMP effect evaluation inside a telecommunication exchange", *IEEE Trans. Electromagn. Compat.*, Vol. 38, No. 3, pp. 265 – 273, Aug 1996

[24] M. Paolone, F. Rachidi, A Borghetti, C.A. Nucci, M. Rubinstein, V.A. Rakov, M.A. Uman, "Lightning electromagnetic field coupling to overhead lines: theory, numerical simulations and experimental validation", *IEEE Trans. Electromagn. Compat.*, Vol. 51, No. 3, pp. 532 – 547, Aug 2009

[25] M. Ianoz, "Review of new developments in the modeling of lightning electromagnetic effects", *IEEE Trans. Electromagn. Compat.*, Vol. 49, No. 2, pp. 224 − 236, May 2007

[26] A. Borghetti, J.A. Gutierrez, C.A. Nucci, M. Paolone, E. Petrache, F. Rachidi, "Lightning-induced voltages on complex distribution systems: models, advanced software tools and experimental verification", *Journal of Electrostatics*, Vol. 60, pp. 163 − 174, 2004

[27] A. Piantini, J.M. Janiszewski, "Lightning-induced voltages on overhead lines - application of the extended Rusck model", *IEEE Trans. Electromagn. Compat.*, Vol. 51, No. 3, pp. 548 − 558, Aug 2009

[28] A. Orlandi, C. Mazzetti, Z. Flisowski, M. Yarmarkin, "Systematic approach for the analysis of the electromagnetic environment inside a building during lightning strike", *IEEE Trans. Electromagn. Compat.*, Vol. 40, No. 4, pp. 521 − 535, Nov 1998

[29] V. Rakov, F. Rachidi, "Overview of recent progress in lightning research and lightning protection", *IEEE Trans. Electromagn. Compat.*, Vol. 51, No. 3, pp. 428 − 442, Aug 2009

[30] D.B. Davidson, "Computational electromagnetics for RF and microwave engineering", *Cambridge University Press*, First Edition, 2005

[31] Y. Baba, V.A. Rakov, "Electromagnetic models of the lightning return stroke", *Journal of Geophysical Research*, Vol. 112, D04102, pp. 1 − 17, 2007

[32] Y. Baba, V.A. Rakov, "Electric and magnetic fields predicted by different electromagnetic models of the lightning return stroke versus measured fields", *IEEE Trans. Electromagn. Compat.*, Vol. 51, No. 3, pp. 479 − 487, Aug 2009

[33] G. Maslowski, V.A. Rakov, "New insights into lightning return-stroke models with specified longitudinal current distribution", *IEEE Trans. Electromagn. Compat.*, Vol. 51, No. 3, pp. 471 − 478, Aug 2009

[34] S.H.S. Moosavi, R. Mioni, S.H.H. Sadeghi, "Representation of a lightning return-stroke channel as a nonlinearly loaded thin-wire antenna", *IEEE Trans. Electromagn. Compat.*, Vol. 51, No. 3, pp. 488 − 498, Aug 2009

[35] F. Rachidi, "Modeling lightning return strokes to tall structures: a review", *Journal of Lightning Research*, Vol. 1, pp. 16 − 31, 2007

[36] L. Grcev, F. Rachidi, V. Rakov, "Comparison of electromagnetic models of lightning return strokes using current and voltage sources", *Proc. 12th Int. Conf. Atmospheric Electricity*, Versailles, 2003

[37] Y. Baba, V. Rakov, "On the interpretation of ground reflections observed in small-scale experiments simulating lightning strikes to towers", *IEEE Trans. Electromagn. Compat.*, Vol. 47, No. 3, pp. 533 − 542, Aug 2005

[38] K. Yamamoto, T. Noda, S. Yokoyama, A. Ametani, "An experimental study of lightning overvoltages in wind turbine generation systems using a reduced-size model", *Electrical Engineering in Japan*, Vol. 158, No. 4, pp. 65 − 72, 2007

[39] Y. Baba, V.A. Rakov, "Applications of electromagnetic models of the lightning return stroke", *IEEE Transactions on Power Delivery*, Vol. 23, No. 2, pp. 800 − 811, Apr 2008

[40] S. Evans, "Application of dimensional analysis in electromagnetic measurements", *4110 Classical Electromagnetism Notes*, University Engineering Department, Cambridge

[41] V. Cooray, "Propagation effects due to finitely conducting ground on lightning-generated magnetic fields evaluated using Sommerfeld's integrals", *IEEE Trans. Electromagn. Compat.*, Vol. 51, No. 3, pp. 526 − 531, Aug 2009

[42] F. Rachidi, M. Rubinstein, J. Montanya, J. Bermudez, R.R. Sola, G. Sola, N. Korovkin, "A review of current issues in lightning protection of new-generation wind-turbine blades", *IEEE Transactions on Industrial Electronics*, Vol. 55, No. 6, pp. 2489 − 2496, June 2008

[43] A. Schaffar, J. Decibieux, L. Mureax, "Arianne 5 launcher lightning qualification logic", *ESA Workshop on Aerospace EMC*, Florence, Italy, Mar/Apr 2009

[44] E. Bachelier, F. Issac, S. Bertuol, J.P. Parmantier, J.C. Elliot, "Numerical EM simulation for the definition of the lightning protection systems of the future VEGA and SOYUZ launching pads", *ESA Workshop on Aerospace EMC*, Florence, Italy, Mar/Apr 2009

[45] R.A. Dalke, C.L. Holloway, P. McKenna, M. Johansson, A.S. Ali, "Effects of reinforced concrete structures on RF communications", *IEEE Trans. Electromagn. Compat.*, Vol. 42, No. 4, pp. 486 − 496, Nov 2000

[46] G. Ala, M.L. di Silvestre, "A simulation model for electromagnetic transients in lightning protection systems", *IEEE Trans. Electromagn. Compat.*, Vol. 44, No. 4, pp. 539 − 554, Nov 2002

[47] A. Mimouni, F. Rachidi, Z. Azzouz, "Electromagnetic environment in the immediate vicinity of a lightning return stroke", *Journal of Lightning Research*, Vol. 2, pp. 64 – 75, 2007

[48] L. Grcev, P.J. van Deursen, J.B.M. van Waes, "Lightning current distribution to ground at a power line tower carrying a radio base station", *IEEE Trans. Electromagn. Compat.*, Vol. 47, No. 1, pp. 160 – 170, Feb 2005

[49] L. Grcev, "Modeling of underground electrodes under lightning conditions", *IEEE Trans. Electromagn. Compat.*, Vol. 51, No. 3, pp. 559 – 571, Aug 2009

[50] L. Grcev, "Impulse efficiency of ground electrodes", *IEEE Transactions on Power Delivery*, Vol. 21, No. 1, pp. 441 – 451, Jan 2009

[51] H. Motoyama, "Experimental and analytical studies on lightning surge characteristics of ground mesh", *Electrical Engineering in Japan*, Vol. 160, No. 4, pp. 687 – 693, 2007

[52] H. Motoyama, "Electromagnetic transient response of buried bare wire and ground grid", *IEEE Transactions on Power Delivery*, Vol. 122, No. 3, pp. 1673 – 1679, Jul 2007

[53] International Telecommunication Union, Standardization Sector, "Series K: Protection against interference, Bonding configurations and earthing inside a telecommunication building", *ITU-T Recommendation K.27*, May 1996

[54] R.G. Urban, "Review and design of a lightning protection system for XDM and KAT-7 dishes", *Postdoctoral Report*, Department Electrical and Electronic Engineering, Stellenbosch University, December 2007

[55] R. Sumaraju, J. Trumpf, "Frequency, temperature and salinity variation of the permittivity of seawater", *IEEE Transactions on antennas and propagation*, Vol. 54, No. 11, pp. 3441 – 3448, Nov 2006

[56] H.C. Reader, W de Villiers, P.G. Wiid, P.S. van der Merwe, R.T. Lord, "RFI investigation of XDM", *National Research Foundation, Measurement Investigation Report, NRF-KAT7-1.1-TR-001*, Revision 1, 20 May 2008

[57] B. Keiser, "Principles of electromagnetic compatibility", *Artech House*, Third Edition, 1987

[58] C.A. Balanis, "Antenna theory, analysis and design", *Wiley*, Third Edition, 2005

[59] P.C.T. van der Laan, "Electromagnetic fields in electrical engineering, understanding basic concepts", *Shaker Publishing*, 2005

[60] V. Amoruso, F. Lattarulo, "Lightning-originated tangential electric field across air-soil interfaces", *IEEE Proc. Sci. Meas. Technol.*, Vol. 141, No. 1, pp. 65 − 70, Jan 1994

[61] Y. Baba, V. Rakov, "On the mechanism of attenuation of current waves propagating along a vertical perfectly conducting wire above ground: application to lightning", *IEEE Trans. Electromagn. Compat.*, Vol. 47, No. 3, pp. 521 − 532, Aug 2005

[62] Y. Baba, V.A. Rakov, "Influences of the presence of a tall grounded strike object and an upward connecting leader on lightning currents and electromagnetic fields", *IEEE Trans. Electromagn. Compat.*, Vol. 49, No. 4, pp. 886 − 892, Nov 2007

[63] A.M.A. Baker, M.S. Alam, M. Tanrioven, H.B. Ahmad, "Electromagnetic compatibility analysis in buildings affected by lightning strike", *IEEE Trans. Electromagn. Compat.*, Vol. 47, No. 3, pp. 197 − 204, Aug 2005

[64] J.L. Bermudez, F. Rachidi, W. Janischewskyj, V. Shostak, M. Rubinstein, D. Pavanello, A.M. Hussein, J.S. Chang, M. Paolone, "Determination of lightning currents from far electromagnetic fields: effect of a strike object", *Journal of Electrostatics*, Vol. 65, pp. 289 − 295, 2007

[65] S. Cristina, A. Orlandi, "Lightning channel's influence on currents and electromagnetic fields in a building struck by lightning", *IEEE*, pp. 338 − 342, 1990

[66] H.J. Geldenhuys, "The effects of lightning in shallow coal mines − an engineering study", *University of Witwatersrand*, A thesis submitted to the Faculty of Engineering, University of Witwatersrand, in fulfilment of the requirements for the degree of Doctor of Philosophy in Electrical Engineering, Johannesburg, Feb 1995

[67] N.W. Ebertsohn, R.H. Geschke, H.C. Reader, "Cable trays in EMC: measurement and modeling to 30 MHz", *IEEE Trans. Electromagn. Compat.*, Vol. 49, No. 2, pp. 346 − 353, May 2007

[68] C.A. Nucci, F. Rachidi, "Lightning-induced overvoltages", *IEEE Transmission and Distribution Conference*, Panel Session: Distribution Lightning Protection, New Orleans, April 1999

[69] R.K. Pokharel, M. Ishii, "Applications of time-domain numerical electromagnetic code to lightning surge analysis", *IEEE Trans. Electromagn. Compat.*, Vol. 49, No. 3, pp. 623 − 631, Aug 2007

[70] K. R. Rand, “Lightning protection and grounding solutions for communication sites”, *Polyphaser Corporation*, First Edition, Jan 2000

[71] M. Rubinstein, “An approximate formula for the calculation of the horizontal electric field from lightning at close, intermediate and long range”, *IEEE Trans. Electromagn. Compat.*, Vol. 38, No. 3, pp. 531 – 535, Aug 1996

[72] T. Tominaga, N. Kuwabara, J. Kato, A. Ramli, A. Halim, H. Ahmad, “Characteristics of lightning surges induced in telecommunication center in tropical area”, *IEEE Trans. Electromagn. Compat.*, Vol. 45, No. 1, pp. 82 – 91, Feb 2003

[73] J. Zou, J. Lee, Y. Ji, S. Chang, B. Zhang, J. He, “Transient simulation model for a lightning protection system using the approach of a coupled transmission line network”, *IEEE Trans. Electromagn. Compat.*, Vol. 49, No. 3, pp. 614 – 622, Aug 2007

– And in the end it is not the years in your life that count, but the life in your years –

– Abraham Lincoln –